11

Inverted Circulations in the Pacific Basin

Detailed description of the world oceans can be obtained from the datasets presented in Chap. 10. In this chapter, characteristics of the inverted circulations in the Pacific Ocean are presented.

11.1 General Features

Figure 11.1 shows the inverted annual mean volume transport stream function (Ψ) and vertically integrated velocity (U, V) for the Pacific Basin that is calculated by using the method depicted in Chap. 8. The annual mean northward transport across the equator in the west is 21.7 Sv, between the -21.7 Sv isoline at the western boundary (northeast coast of New Guinea) to the 0 Sv isoline near 170°W (Fig. 11.1a). This current meanders and generates several eddies such as the Mindanao Eddy (cyclonic), near the southern Philippines (Masumoto and Yamagata 1991) and the Halmahera eddy (anticyclonic) near Indonesia. The northward current joins the North Equatorial Current with 30 Sv transport (from 0 to 30 Sv isolines) east of the Philippines (10–15°N). Of these 51.7 Sv of water, 21.7 Sv are lost to the Indonesian Seas directly, or through the South China Sea indirectly. The remaining 30 Sv of water continues northward to Japan and then eastward with the anticyclonic gyre. This subtropical gyre recirculates 20 Sv between 25 and 35°N (from 30 to 50 Sv isolines) and makes 50 Sv of the Kuroshio Current, east of Japan. The seasonal variability is small in the inverted volume transport stream function and vertically integrated velocity (Fig. 11.2).

There are several low-latitude cyclonic gyres, with axes along 8°N and 8°S (Chu and Fan 2006). Among them, an evident cyclonic gyre occurs in the north equatorial region between 180 and 120°E, and three smaller cyclonic eddies (also called broken gyres) appear in the south equatorial region, east of 170°E. The north equatorial gyre appeared clearly on the study by Munk (1950) of the wind-driven circulation of the North Pacific, and was identified by Reid (1997) using hydrographic data. The south equatorial gyre identified using the

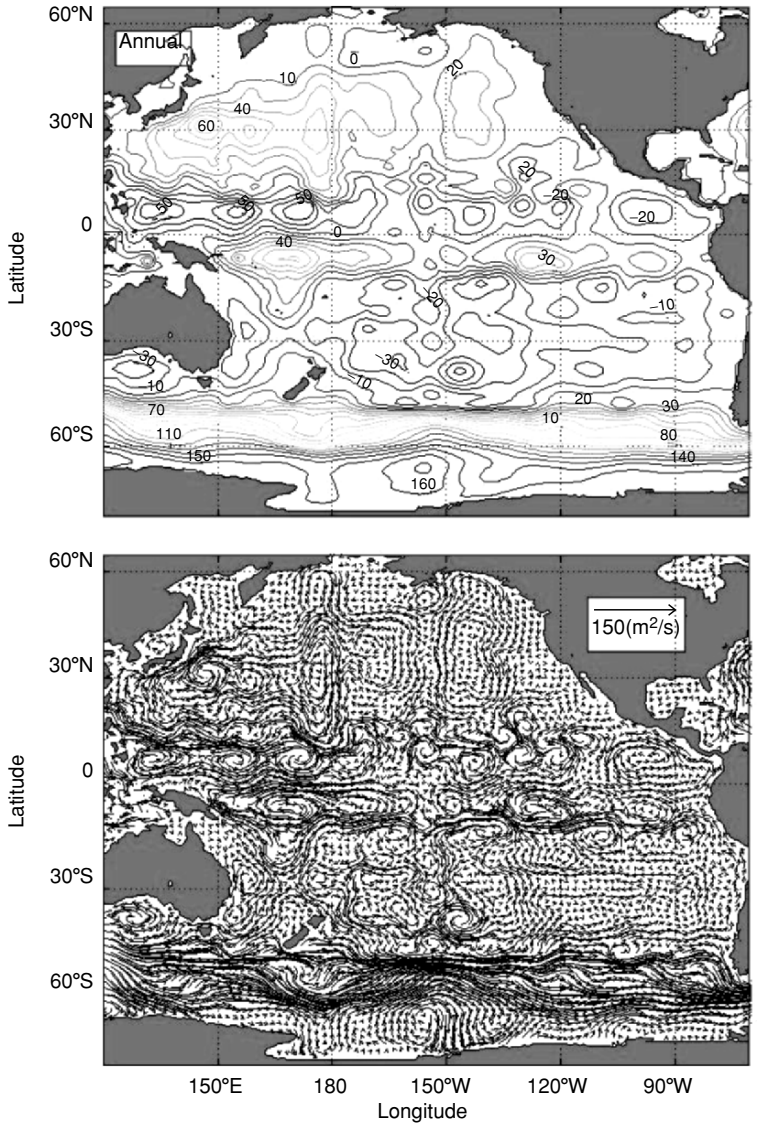

Fig. 11.1. Annual mean (**a**) volume transport stream function (Ψ) and (**b**) vertically integrated velocity (U, V) for the Pacific basin (from Chu and Fan 2006, Journal of Marine Systems)

P-vector method (broken gyre) is different from Reid's (1989) description of a complete gyre structure. The south subtropical anticyclonic gyre occurs east of 180°E between 12°S and 45°S and recirculates 30 Sv of water.

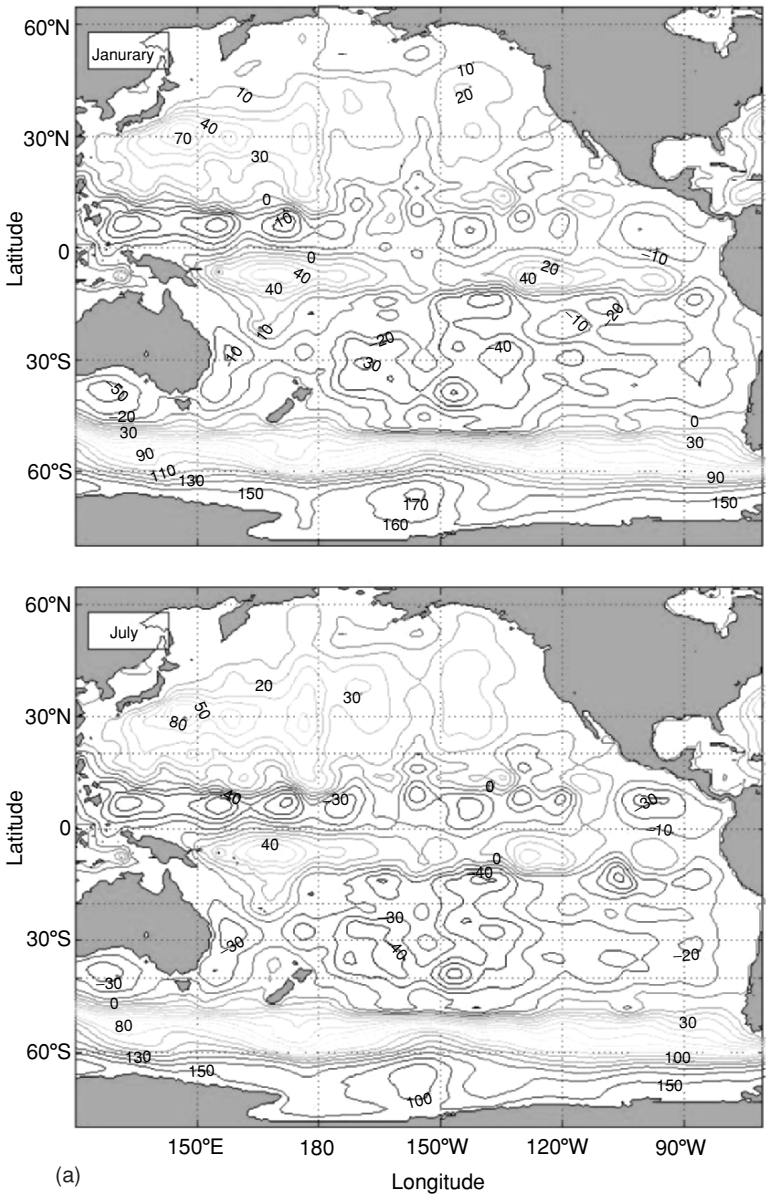

Fig. 11.2. (**a**) Seasonal variation of volume transport stream function (Ψ) for the Pacific Ocean (from Chu and Fan 2006, Journal of Marine Systems).

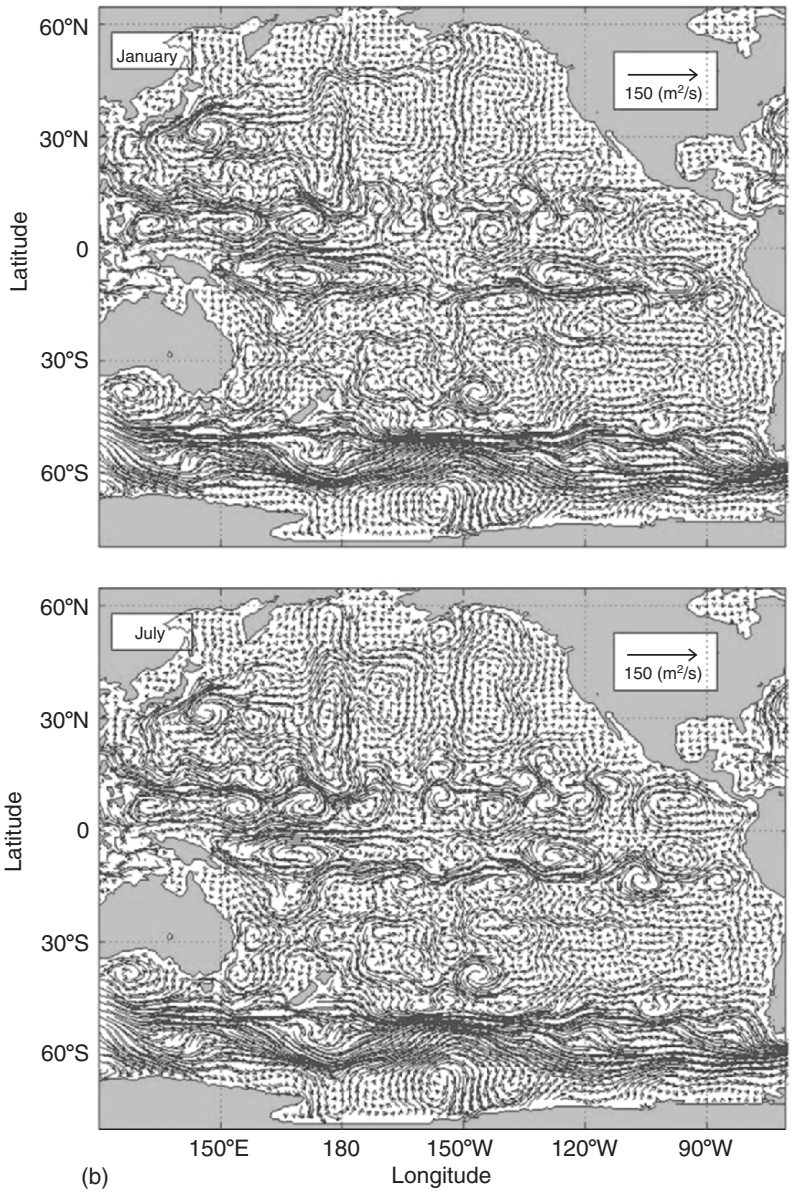

Fig. 11.2. (**b**) Seasonal variation of vertically integrated velocity (U, V) for the Pacific basin (from Chu and Fan 2006, Journal of Marine Systems)

11.2 Water Mass Crossroads

The western equatorial Pacific, particularly the southernmost Philippine Sea, is called "water mass crossroads" by Fine et al. (1994) due to the confluence of several water masses from higher latitudes of both hemispheres (Wyrtki, 1961a, b; Fine et al. 1994). The volume transport stream function and vertically integrated velocity are calculated using the method described in Chap. 7, as shown in Fig. 11.3.

11.2.1 General Description

The annual mean northward transport across the equator in the west is around 20 Sv, between the −20 Sv isoline at the western boundary (northeast coast of New Guinea) to the 0 Sv isoline near 170°W (Fig. 11.3a). This current meanders and generates several eddies such as the Mindanao Eddy (cyclonic) near southern Philippines and the Halmahera Eddy (anticyclonic) near Indonesia. The northward current joins the North Equatorial Current with 30 Sv transport (from 0 to 30 Sv isolines) east of the Philippines (10–15°N). Of these 50 Sv of water, 20 Sv are lost to the Indonesian Seas directly, or via the South China Sea indirectly. The remaining 30 Sv of water continues northward to Japan and then eastward with the anticyclonic gyre. This subtropical gyre recirculates 20 Sv between 25 and 35°N (from 30 to 50 Sv isoline) and makes 50 Sv of the Kuroshio Current east of Japan.

There are several low-latitude cyclonic gyres, with axes along 8°N and 8°S. Among them, an evident cyclonic gyre occurs in the north equatorial region between 180° and 120°E, and three smaller cyclonic eddies (also called broken gyres) appear in the south equatorial region, east of 170°E. The north equatorial gyre appeared clearly on the study by Munk (1950) of the wind-driven circulation of the North Pacific, and was identified by Reid (1997) using hydrographic data. The south equatorial gyre identified using the P-vector method (broken gyre) is different from Reid's (1989) description of a complete gyre structure. The south subtropical anticyclonic gyre occurs east of 180°E between 12°S and 45°S and recirculates 30 Sv of water.

After encountering the western boundary along the Philippine coast, the North Equatorial Current bifurcates into the northward flowing Kuroshio and the southward flowing Mindanao Current (Masuzawa 1969; Nitani 1970; Wijffels et al. 1995). The Mindanao Current and the New Guinea Coastal Undercurrent flow equatorward, feeding both the North Equatorial Counter Current, the New Guinea Coastal Current, and the flow from the Pacific to the Indian Ocean, that is, the Indonesian Throughflow.

The Mindanao Current is unique because it is the only northern hemisphere low-latitude western boundary current that has a mean flow toward the equator (Lukas et al. 1996), and is important because it feeds the Indonesian Throughflow (Ffield and Gordon 1992), and, in turn, sends impacts on the stratification of the Indian Ocean (Lukas et al. 1996; Godfrey 1996).

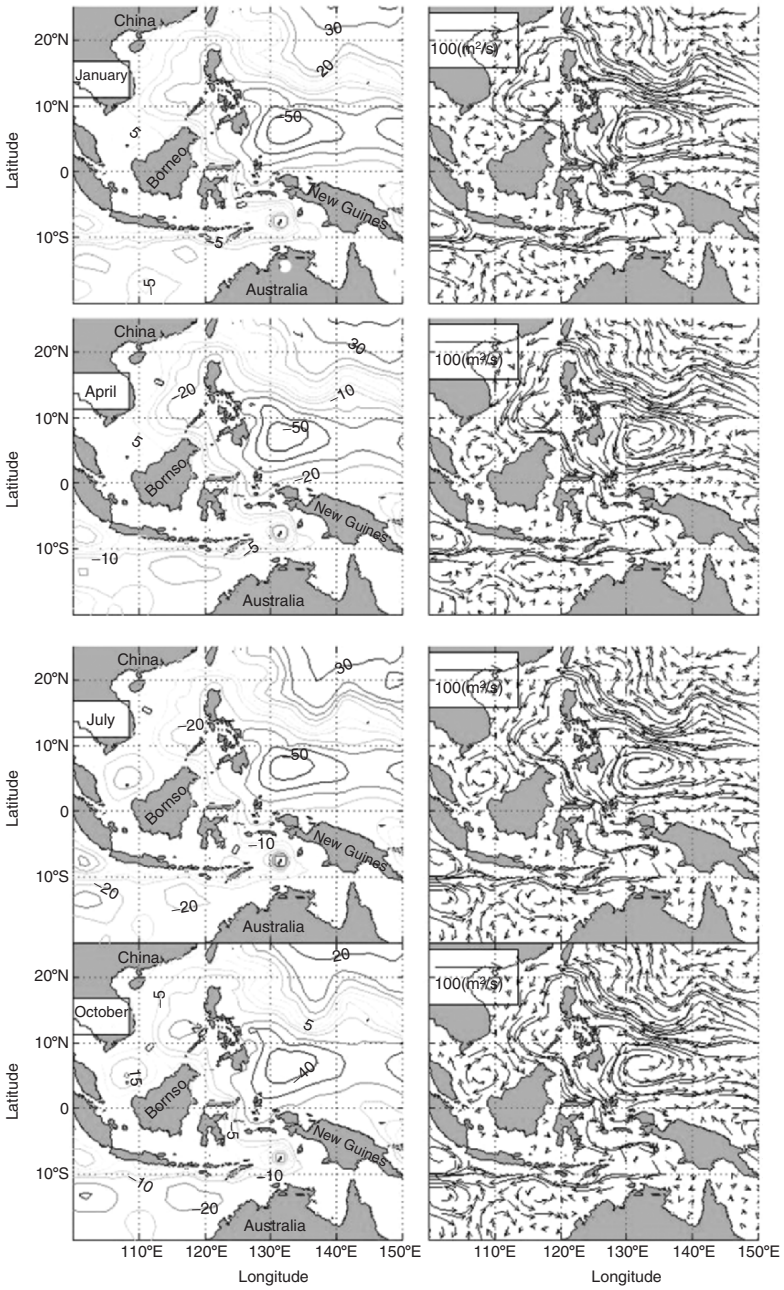

Fig. 11.3. The inverted monthly mean Ψ and (U, V) vector fields in the vicinity of water mass crossroads: (**a**) January, (**b**) April, (**c**) July, and (**d**) October

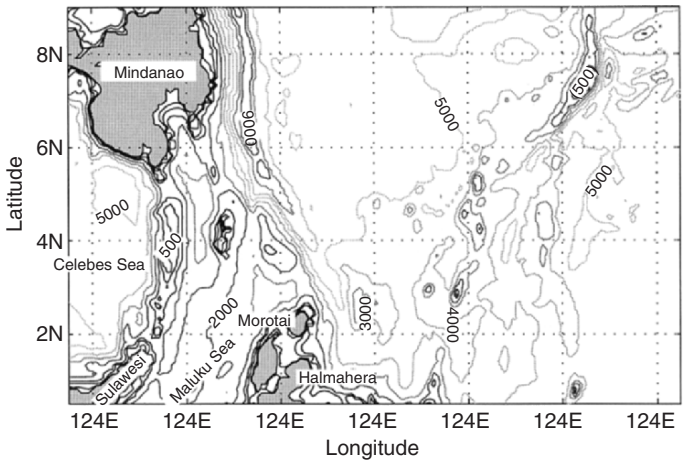

Fig. 11.4. Geography and isobaths showing the bottom topography of the southwestern Pacific near Midanao Island (from Chu et al. 2003d, Chinese Journal of Oceanology and Limnology)

The North Equatorial Counter Current bifurcates into three branches near 130°E. The central branch continues to flow eastward as the North Equatorial Counter Current. The northern branch moves northwestward and forms a cyclonic eddy near Mindanao Island, which is called the Mindanao Eddy. The southern branch moves southwestward, joins the northwest moving currents from the New Guinea Coastal Current and the New Guinea Coastal Undercurrent, which are parts of the South Equatorial Current, and forms an anticyclonic eddy near the Halmahera Sea, which is called the Halmahera Eddy.

Metzger and Hurlburt (1996) adopted a high horizontal resolution six-layer model driven by monthly climatological winds to analyze the coupled dynamics among the Sulu Sea, the South China Sea, and the Pacific Ocean. Their model simulates the existence of the dual eddy structure. The Mindanao Eddy and the Halmahera Eddy are in the middle of the water mass crossroads, surrounded by complicated topography (Fig. 11.4), and connected to major equatorial currents. Seasonal variability (thermohaline structure and circulation) of the two eddies represents the seasonal variability in low latitude dynamics and interbasin water mass exchange.

Water mass characteristics have been used to infer the flow along the isopycnal surfaces. For example, between 300 and 1,000 m the North Pacific Intermediate Water (around $\sigma_\theta = 26.8\,\mathrm{kg\ m^{-3}}$) and Antarctic Intermediate Water (around $\sigma_\theta = 27.2\,\mathrm{kg\ m^{-3}}$) reach this area (Reid 1997; Tschiya 1991; Talley 1993; Bingham and Lukas 1994, 1995; Fine et al. 1994). Kashino et al. (1996) confirm the existence of the North Pacific Intermediate Water and Antarctic Intermediate Water in the far western equatorial Pacific near the entrances

to the Celebes and Halmahera Seas. They also provide further evidence for the flow of waters from the southern hemisphere across the equator, turning eastward into the North Equatorial Counter Current.

In order to obtain current signal quantitatively from hydrographic data in this area is not easy. Godfrey (1996) pointed out that there are a number of special difficulties such as active internal tides and the geostrophy that can only be used with caution to estimate the current distribution in the area. To overcome these difficulties, the P-vector method on the isopycnal surfaces can be used to invert the absolute velocity from GDEM (Chu et al. 2003d).

11.2.1 (T, S) Fields

In the pycnocline layer (100–300 m) there are salinity maximum layers from the North and South Pacific. These water masses are called North Pacific Tropical Water and South Pacific Tropical Water by Kashino et al. (1996). It is not the intention to present a detailed climatological thermohaline structure, but only as representative features on $\sigma_\theta = 25.0\,\mathrm{kg\ m^{-3}}$ (in pycnocline) as illustration. This level is generally considered to be the level where the salinity maximum occurs (Kashino et al. 1996).

Temperature

Bimonthly mean temperature on $\sigma_\theta = 25.0\,\mathrm{kg\ m^{-3}}$ (Fig. 11.5 shows a cool (northern) – warm (southern) eddy-like structure with a strong seasonal variability. The cool (warm) eddy is enclosed by 18.25°C (20°C) isoline. The cool eddy shows up almost all year round and is located at 128–133°E and 6–9°N, and the warm eddy is evident only in winter (February) and spring (April). A weak thermal front exists between the cool and warm eddies with horizontal temperature gradient less than 1°C/100 km. This front strengthens from December to April, and weakens from April to December.

Salinity

Salinity is generally used for identifying the water masses in the area. For example, Kashino et al. (1996) used 35.0 ppt contour as the boundary of high salinity South Pacific Tropical Water in analyzing R/V Kaiyo World Ocean Circulation Experiment (WOCE) expedition I in October 1992 and II in February 1994. Both expeditions covered the same area as ours (Fig. 11.6).

Horizontal salinity distribution on $\sigma_\theta = 25.0\,\mathrm{kg\ m^{-3}}$ observed during Kaiyo WOCE I and II, shows the high-salinity South Pacific Tropical Water in the southern area. In October 1992, this water reached 2°N near Morotai Island and 3°N along 134°E. In February 1994, the South Pacific Tropical Water reached farther north than in October 1992, i.e., north of Morotai Island and 5°N along 130°E (Kashino et al. 1996).

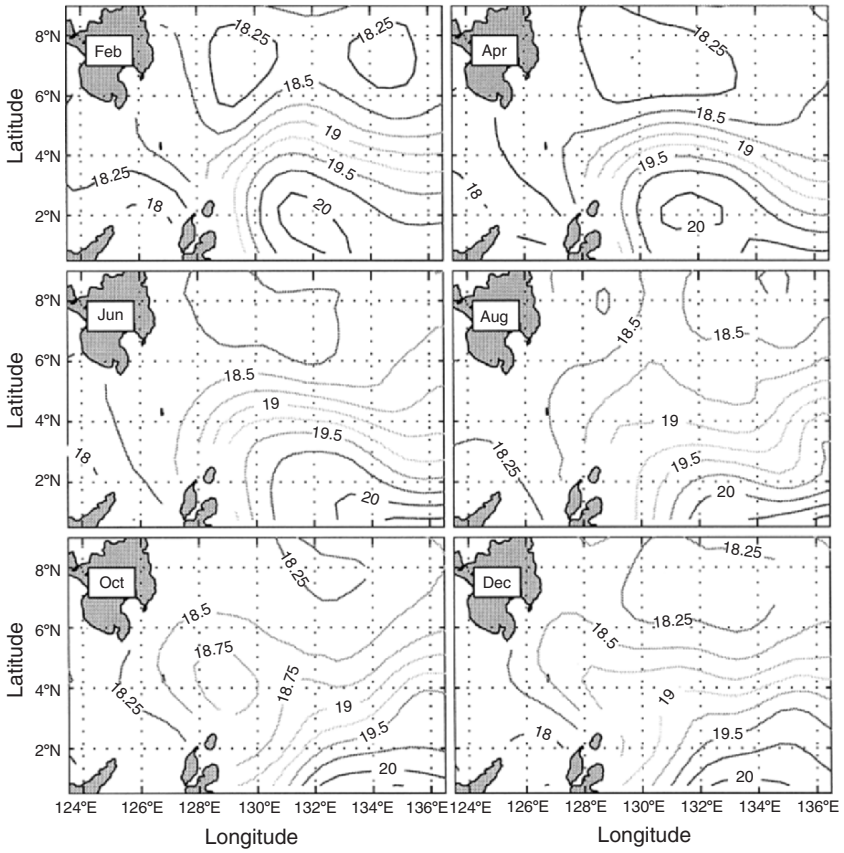

Fig. 11.5. Bimonthly mean temperature (°C) fields on $\sigma_\theta = 25.0\,\mathrm{kg\,m^{-3}}$ from GDEM (from Chu et al. 2003d, Chinese Journal of Oceanology and Limnology)

The monthly mean salinity on $\sigma_\theta = 25.0\,\mathrm{kg\ m^{-3}}$ (Fig. 11.6) shows the similar feature depicted by Kashino et al. (1996). The high-salinity South Pacific Tropical Water (≥ 35.0 ppt) is located in the southern part of the area, and expands toward the northwest in February–June, and retreats toward the southeast in August–December. In February and April, a high salinity center enclosed by 35.3 ppt occurs at 131–133°E, 1–3°N, which coincides with the warm center (Fig. 11.5).

11.2.2 Velocity Field

Most important current system is featured as the southward flowing Mindanao Current, the eastward flowing North Equatorial Counter Current, the northwestward flowing New Guinea Coastal Current, and the New Guinea Coastal Undercurrent and associated mesoscale eddies such as the cyclonic Mindanao

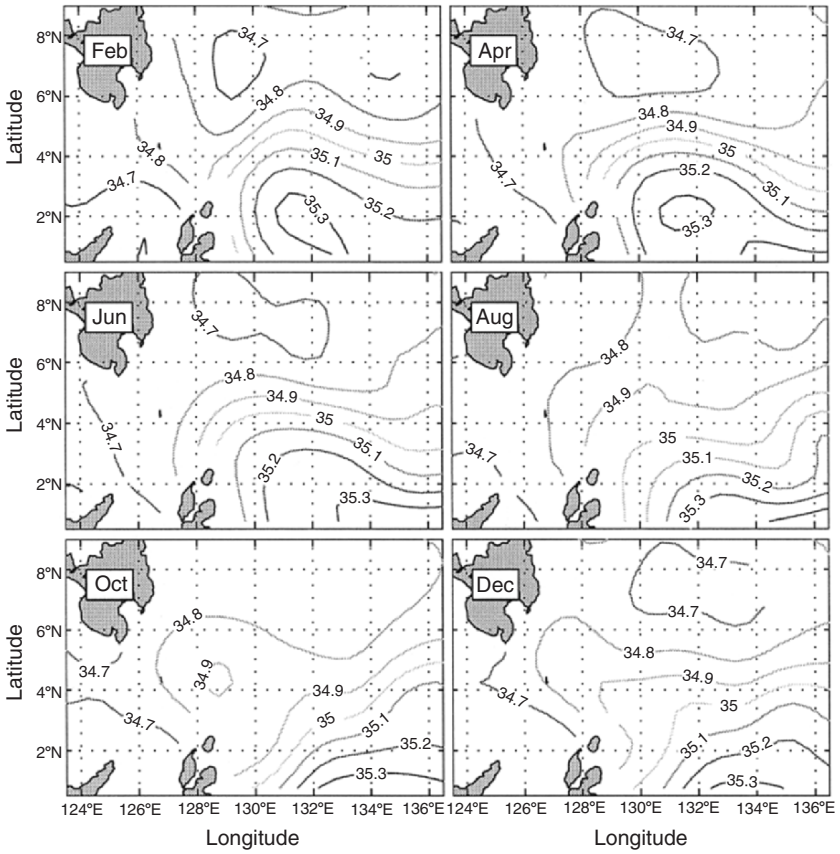

Fig. 11.6. Bimonthly mean salinity (ppt) fields on $\sigma_\theta = 25.0\,\mathrm{kg\,m^{-3}}$ from GDEM (from Chu et al. 2003d, Chinese Journal of Oceanology and Limnology)

Eddy and the anticyclonic Halmahera Eddy. Figure 11.7 shows the horizontal velocity vectors on three different σ_θ levels: pycnocline ($\sigma_\theta = 25.0\,\mathrm{kg\ m^{-3}}$), intermediate ($\sigma_\theta = 26.5\,\mathrm{kg\ m^{-3}}$), and deep ($\sigma_\theta = 27.2\,\mathrm{kg\ m^{-3}}$) levels. The last two levels may represent North Pacific Intermediate Water and Antarctic Intermediate Water in this area.

Pycnocline Level ($\sigma_\theta = 25.0\,\mathrm{kg\ m^{-3}}$)

Three major currents (Mindanao Current, New Guinea Coastal Undercurrent, and North Equatorial Counter Current) and dual eddies (Mindanao Eddy and Halmahera Eddy) are easily identified. They have strong seasonal variability. The Mindanao Current strengthens from October to February and weakens from April to August. After leaving the south tip of Mindanao Island, it flows southeastward following the continental slope (see Figs. 10.7 and 10.4) and

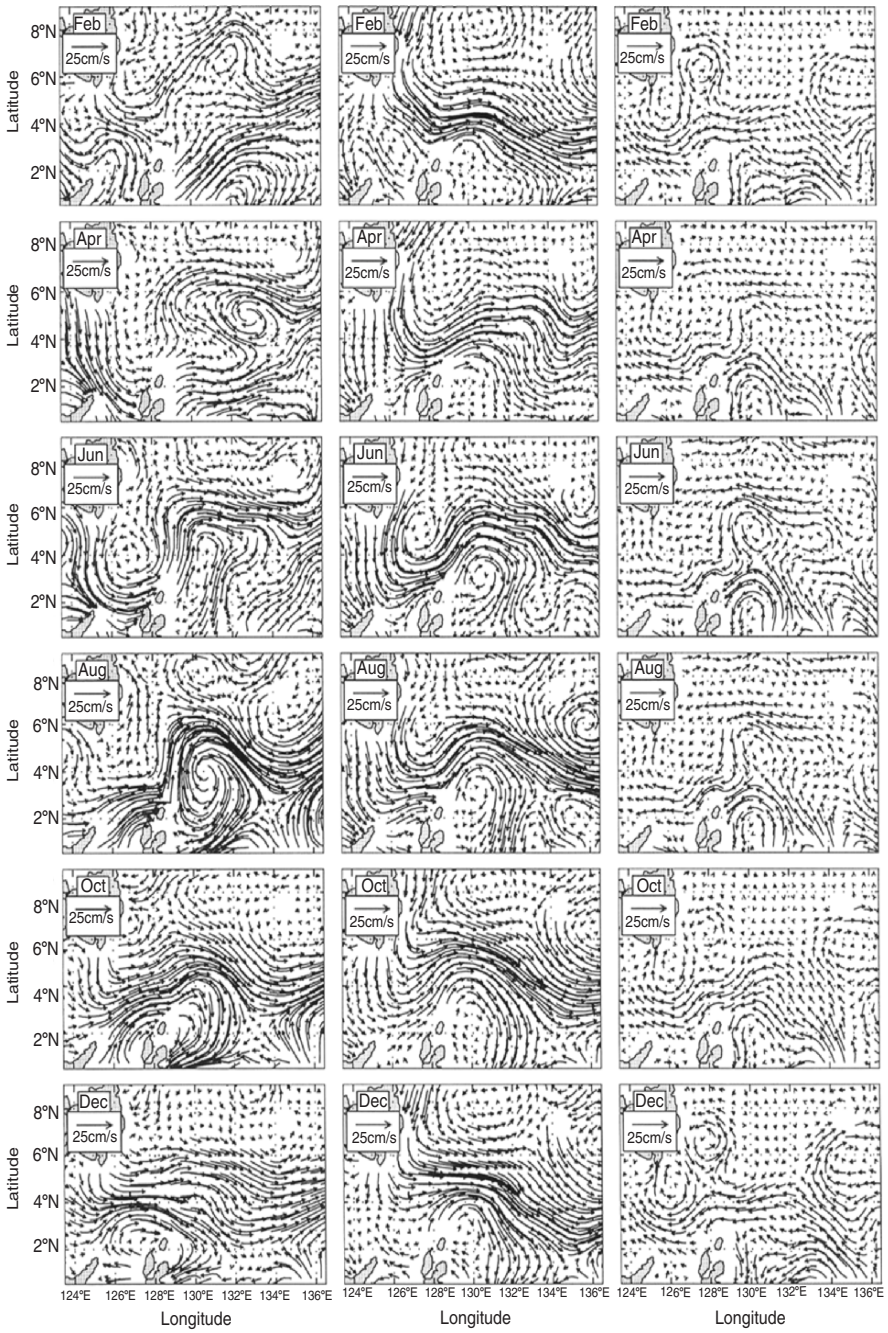

Fig. 11.7. Bimonthly mean velocity vector field east of Midanao Island on the surface of (**a**) $\sigma_\theta = 25.0\,\mathrm{kg\,m^{-3}}$, (**b**) $\sigma_\theta = 26.5\,\mathrm{kg\,m^{-3}}$, and (**c**) $\sigma_\theta = 27.2\,\mathrm{kg\,m^{-3}}$ (from Chu et al. 2003d, Chinese Journal of Oceanology and Limnology)

recirculates northeastward near Morotai Island. Such a recirculation leads to the formation of the cyclonic eddy (Mindanao Eddy). The Mindadao Current is very weak from April to August, strengthens in October, and becomes strong in the winter with the maximum speed around 0.25 m s^{-1} in February. New Guinea Coastal Undercurrent flows northwestward along the northern New Guinea Island (Fig. 10.3). After leaving the north tip of New Guinea Island, it continues to move northward and feeds into an anticyclonic eddy, the Halmahera Eddy. This eddy strengthens in summer (June–August) and weakens in winter (December). In August, the Halmahera Eddy is located at 128–133°E, 2–6°N with a maximum tangential velocity around 0.3 m s^{-1}.

Intermediate Level ($\sigma_\theta = 26.5$ kg m^{-3})

As the water depth increases, the seasonal variation of the velocity reduces. The intermediate level ($\sigma_\theta = 26.5$ kg m^{-3}) is close to the level ($\sigma_\theta = 26.8$ kg m^{-3}), where North Pacific Intermediate Water is located. The Mindanao Current is energetic; nearly 150 km wide, a southward and coastal trapped jet. It turns east after leaving Mindanao Island and feeds into the North Equatorial Counter Current, which separates into three branches near 130°E. The north and south branches feed into the Midanao eddy (cyclonic) and the Halmahera eddy (anticyclonic). The central branch continues as the North Equatorial Counter Current. In winter (December–February), the dual eddies are north–south oriented with the Mindanao Eddy (maximum tangential velocity around 15 cm s^{-1}) located at 128–133°E, 6–9°N, and the Halmahera Eddy (maximum tangential velocity around 0.25 m s^{-1}) located at 128–133°E, 0.5–4°N. In April, Mindanao eddy (Halmahera eddy) expands toward the southwest (northeast). In June, the dual eddies are east–west oriented with the Mindanao eddy in the west and the Halmahera eddy in the east. The size of both eddies is smaller in the summer than in the winter.

Deep Level ($\sigma_\theta = 27.2$ kg m^{-3})

At the deep level, where the Antarctic Intermediate Water is located, the flow pattern is quite different from the pycnocline and intermediate levels. An evident westward flowing current is identified between 2 and 6°N which is in the opposite direction of North Equatorial Counter Current on the pycnocline and intermediate level. The flow pattern clearly shows New Guinea Coastal Undercurrent entering the eastern part of southern boundary (134–136°E) and flowing northwestward with a maximum velocity larger than 20 cm s^{-1} in winter (December–February).

In winter (December–February), the New Guinea Coastal Undercurrent bifurcates at 133°E, 4°N into two branches (northward and westward). The northward branch recirculates at 6°N and forms an anticyclonic mesoscale eddy (around 200 km in diameter). The westward branch flows zonally (under North Equatorial Counter Current) to a longitude near 129°E and splits into

three branches moving southward, westward, and northward. The westward branch transports Antarctic Intermediate Water into the Celebes Sea. The northward branch turns to west at 8°N, recirculates along the west coast of Mindanao Island, and forms a cyclonic eddy (i.e., the Mindanao Eddy). In summer (June–August), the cyclonic Mindanao Eddy is identified southeast of the southern tip of Mindanao Island with 200 km in diameter and a maximum swirl velocity of 0.15 m s^{-1}.

11.2.3 Seasonal Variability of Major Currents

Mindanao Current Along 7°15′N

As mentioned earlier, the Mindanao Current is a major current in the water mass crossroads and feeds into the North Equatorial Counter Current and the Indonesia Throughflow. The seasonal variability of the Mindanao Current affects the seasonal variability of the two current systems, and, in turn, sends impacts on the seasonal variability of the Mindanao eddy (due to the variability of the North Equatorial Counter Current) and the Indian Ocean stratification (due to the variability of the Indonesia Throughflow). Kashino et al. (1999) investigated the current variability at the Pacific entrance of the Indonesia Throughflow. Shriver and Hurlburt (1997) identified the Throughflow from the global thermohaline circulation.

The north–south geostrophic velocities on isopycnal surfaces along 7°15′N are used to represent the seasonal variability of the Mindanao Current (Fig. 11.8a). Positive (negative) values show the poleward (equatorward) flow. The negative values (equatorward flow) are shaded in gray. The top-to-bottom black vertical bars represent the islands. The small black bars occurring at the top or the bottom represent those σ_θ that do not reach these values. The equatorward flowing Mindanao Current has two jet-cores, located in the upper layer above the pycnocline (from the surface to $\sigma_\theta = 25.0$ kg m^{-3}) and deep layer ($\sigma_\theta > 26.5$ kg m^{-3}), respectively. The upper layer jet-core has a strong seasonal variability. Evident equatorward Mindanao Current occurs from December to March with a maximum speed of 0.1 m s^{-1} in January and February and 0.05 m s^{-1} in March, near the east coast of Mindanao Island at $\sigma_\theta = 23.25$ kg m^{-3}. The Mindanao Current disappears from April to November. The deep layer jet-core exists all year round with a weak seasonal variability. Its strength reaches the maximum (0.25 m s^{-1}) in winter and the minimum (0.1 m s^{-1}) in summer.

The v-component is converted from σ_θ to z levels (Fig. 11.8b), and shows the existence of upper layer (around 50 m) jet-core and the deep layer jet-core (300–600 m), respectively. A maximum speed of 100 cm s^{-1} in the Mindanao Current was measured along 7°N (Lukas et al. 1991) using the ADCP. The absolute velocities calculated from GDEM underestimate the actual velocities.

Figure 11.8b also shows the existence of three northward velocity cores. Among them, two cores are close to the coast (west of 130°E) and one core

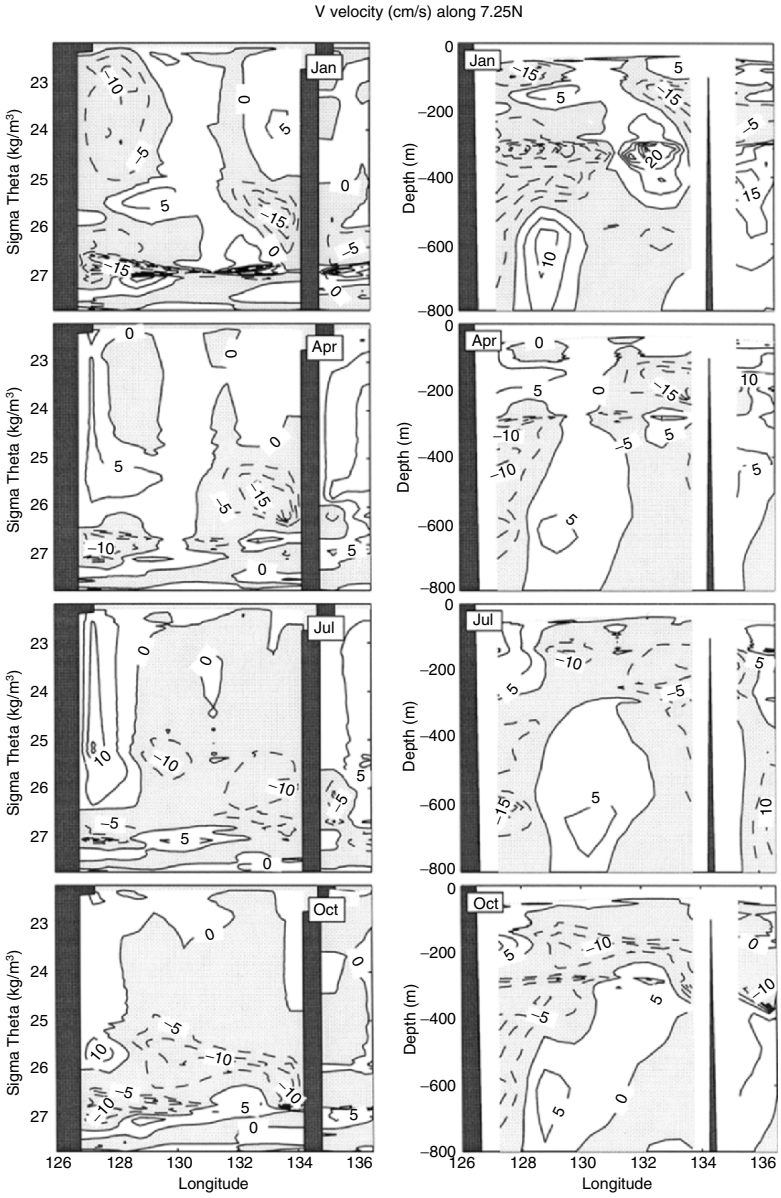

Fig. 11.8. Seasonal variation of north–south velocities (unit: $\mathrm{cm\,s^{-1}}$; northward positive) along 7°15′N latitude representing the flow east of Mindanao Island: (**a**) on σ_θ levels, and (**b**) on z levels (from Chu et al. 2003d, Chinese Journal of Oceanology and Limnology)

(centered at 300 m deep) is away from the coast (130–134°E). The two coastal cores represent the Mindanao Undercurrent described by Hu and Cui (1989), and the third core represents the eastern part of the Mindanao Eddy. The Mindanao Undercurrent has an evident seasonal variation. From April to September, the upper layer of this current, occurring from 50 to 300 m (centered at 200 m), is close to the coast with a width around 200 km and a maximum velocity of 0.1 m s^{-1}. It retreats toward the coast from October to December with a width less than 100 km, and expands toward the east to a longitude near 132°E from January to March having a maximum velocity of 0.1 m s^{-1} at around 150 m deep. The lower layer of the Mindanao Undercurrent, occurring below 400 m, is around 100 km away from the coast and has a weak seasonal variability in its location and a strong seasonal variability in its strength. It reaches a maximum strength (0.2 m s^{-1}) in February and a minimum strength (0.05 m s^{-1}) from March to October.

Mindanao Eddy along 7°15′N

The Mindanao Eddy is a subsurface system, represented by the alternate southward flow west of and northward flow east of 130°E (Fig. 11.8b). In November, the Mindanao Eddy extends from 200 to 500 m with a jet core at 300 m deep. From November to March, its position keeps quite steady, but its strength varies drastically. The Mindanao eddy enhances through February and weakens in March. The northward branch increases to 0.2 m s^{-1} in December and January and the southward branch enhances to 0.25 m s^{-1} in February. From April to October, the Mindanao Eddy shifts southwestward to 128–133°E and south of 6°N (Fig. 11.7).

New Guinea Coastal Undercurrent along 1°15′N

Similar to the Mindanao Current, the New Guinea Coastal Undercurrent is a major current from the Southern Hemisphere to the water mass crossroads and feeds into the North Equatorial Counter Current and Indonesia Throughflow. The seasonal variability of New Guinea Coastal Undercurrent affects the seasonal variability of the North Equatorial Counter Current and Indonesia Throughflow, and, in turn, sends impacts on the seasonal variability of Mindanao eddy (due to variability of the North Equatorial Counter Current) and the Indian Ocean stratification (due to variability of the Indonesia Throughflow).

Since the geostrophic balance is not generally good, we use the computed v velocities on isopycnal surfaces along 1°15′N to imply the seasonal variability of the New Guinea Coastal Undercurrent approximately (Fig. 11.9a). Positive (negative) values show the poleward (equatorward) flow. The negative values (equatorward flow) are shaded in gray. Similar to Fig. 11.8a, the top-to-bottom black vertical bars represent the islands. The vertical bars between 127°15′ and 128°45′E represent Halmahera Island (Fig. 11.4). The small black bars

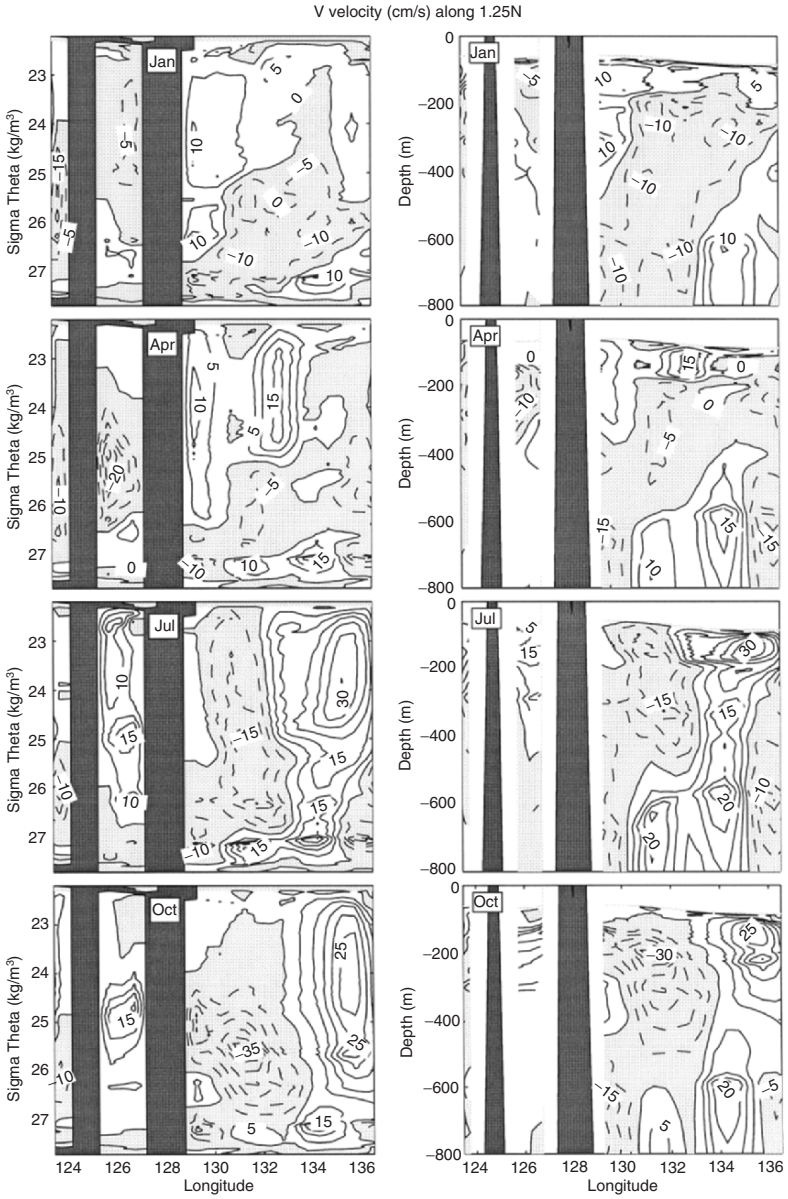

Fig. 11.9. Seasonal variation of north–south velocities (unit: $\mathrm{cm\,s^{-1}}$; northward positive) along 1°15′N latitude representing the flow east of Halmahera Island: (**a**) on σ_θ levels, and (**b**) on z levels (from Chu et al. 2003d, Chinese Journal of Oceanology and Limnology)

occurring at the top or the bottom represent those σ_θ that do not reach the value at that position. The New Guinea Coastal Undercurrent has two branches with the first one along the east coast of Halmahera Island with a width of around 400 km (coastal branch) and the second one located east of 133°E with a width around 300 km (open water branch).

An interesting feature is the out-of-phase variation between the coastal and open water branches. For example, the coastal (open water) branch strengthens (weakens) from September to March and weakens (strengthens) in spring (from March to September). From January to April, the coastal branch is strong with two cores, one in the upper layer (above the pycnocline, i.e., $\sigma_\theta < 25.0\,\mathrm{kg\ m^{-3}}$) and the other in the intermediate layer ($25.0\,\mathrm{kg\ m^{-3}} < \sigma_\theta < 26.5\,\mathrm{kg\ m^{-3}}$). The maximum northward velocity is around $0.15\,\mathrm{m\ s^{-1}}$. The open water branch is located in the deep layer ($\sigma_\theta > 26.5\,\mathrm{kg\ m^{-3}}$) with a maximum northward velocity of $0.15\,\mathrm{m\ s^{-1}}$. From April to October, the coastal (open water) branch weakens (strengthens) with a maximum northward velocity around $0.05\,\mathrm{m\ s^{-1}}$ ($0.4\,\mathrm{m\ s^{-1}}$ in August). Besides, the open water branch extends from near surface to deep layer. Such an out-of-phase variation is also easily seen in the cross section of v-component on z level (Fig. 11.9b).

North Equatorial Counter Current (Along 130°E)

The North Equatorial Counter Current, originated from the confluence of southward flowing Mindanao Current and northward flowing New Guinea Coastal Undercurrent, is an eastward equatorial flow that is centered at around 5°N (e.g., Lukas et al. 1991). We use the east–west geostrophic velocities on isopycnal surfaces along 130°E longitude to represent the seasonal variability of the North Equatorial Counter Current (Fig. 11.10a). Positive (negative) values show the eastward (westward) flow. The negative values (westward flow) are shaded in gray.

The North Equatorial Counter Current extends from the surface to the level of $\sigma_\theta = 27.0\,\mathrm{kg\ m^{-3}}$ all the year round. It occurs between 3° and 8°N from June to December and south of 8°N with two branches separated by an upper layer westward current from January to May, with two jet-cores, located in the pycnocline layer (centered around $\sigma_\theta = 25.0\,\mathrm{kg\ m^{-3}}$) and in the intermediate layer ($27.0\,\mathrm{kg\ m^{-3}} > \sigma_\theta > 26.0\,\mathrm{kg\ m^{-3}}$), respectively. The pycnocline layer jet-core has a strong seasonal variability with a maximum speed of $0.4\,\mathrm{m\ s^{-1}}$ ($0.1\,\mathrm{m\ s^{-1}}$) in August (February). The intermediate layer jet-core is usually stronger than the pycnocline layer core with less seasonal variability. The maximum speed in the intermediate layer jet-core is found to be $0.45\,\mathrm{m\ s^{-1}}$ in February and $0.2\,\mathrm{m\ s^{-1}}$ in May.

Halmahera Eddy (Along 130°E)

The v-component on σ_θ is converted to that on z levels (Fig. 11.10b). The North Equatorial Counter Current separates near 130°E into three branches,

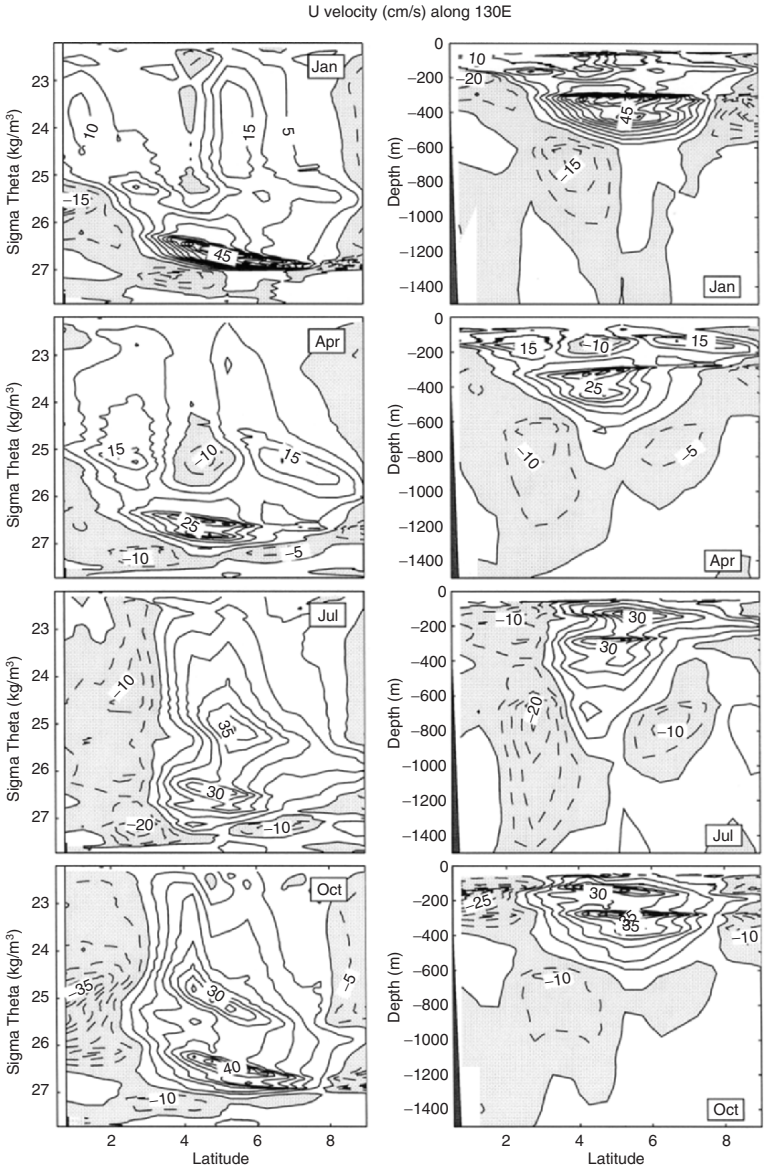

Fig. 11.10. Seasonal variation of east–west velocities (unit: $\mathrm{cm\,s^{-1}}$; eastward positive) along 130°E longitude representing the North Equatorial Counter Current: (**a**) on σ_θ levels, and (**b**) on z levels (from Chu et al. 2003d, Chinese Journal of Oceanology and Limnology)

the central branch (continuation of the North Equatorial Counter Current), the north branch feeding into the Mindanao Eddy, and south branch feeding into the Halmahera Eddy. The strength of the Halmahera Eddy is represented by the velocity of the westward flow. It strengthens in summer (June–August) and weakens in winter (December). The maximum westward speed in the southern flank reaches $0.2\,\mathrm{m\ s^{-1}}$ in summer and $0.10\,\mathrm{m\ s^{-1}}$ in winter.

11.2.5 Vertically Integrated Velocity

Monthly mean vertically integrated (for the whole water column) velocity is computed to represent the volume transport (Fig. 11.11). Three major currents (Mindanao Current, New Guinea Coast Undercurrent, and North Equatorial Counter Current) and dual eddies (Mindanao eddy and Halmahera eddy) are also identified in the integrated flow field whose seasonal variation is evident. The integrated Mindanao Current strengthens from October to February and weakens from April to August. After leaving the south tip of Mindanao Island, It flows southeastward following the continental slope and recirculates northeastward near Morotai Island and then turns towards the east. The recirculation leads to the formation of the Mindanao eddy (cyclonic eddy), and the eastward flow feeds into the North Equatorial Counter Current. The New Guinea Coastal Undercurrent flows northwestward into the area between 134° and 136°E at 0.5°N latitude and then joins the North Equatorial Counter Current at 133°E, 3°N. The dual eddy pattern is evident from June to August.

11.2.6 Volume Transport

Mindanao Current

The computed monthly total and layered (between two σ_θ levels) volume transports across 7°15′N (northward positive) between 126°45′ (Mindanao coast) and 130°45′E longitudes (Fig. 11.12) are used to represent the seasonal variability of Mindanao Current volume transport. The dashed, dotted, and solid curves indicate northward, southward, and net transports, respectively. The northward flow is weaker than the southward flow for the total transport and the most layered transports except the deep layer ($\sigma_\theta \geq 27.025\,\mathrm{kg\ m^{-3}}$), where the northward flow is dominant. The total transport is negative (southward) all the year round with a minimum value of $-40.2\,\mathrm{Sv}$ in January and a maximum value of $-5.3\,\mathrm{Sv}$ in June and July having the annual mean transport of $-23.4\,\mathrm{Sv}$, which agrees with many existing estimations such as $-26, -20\,\mathrm{Sv}$ by Lukas et al. (1991).

North Equatorial Counter Current

Monthly total and layered (between two σ_θ levels) volume transports are computed across 130°E (eastward positive) between 0°45′N and 8°15′N

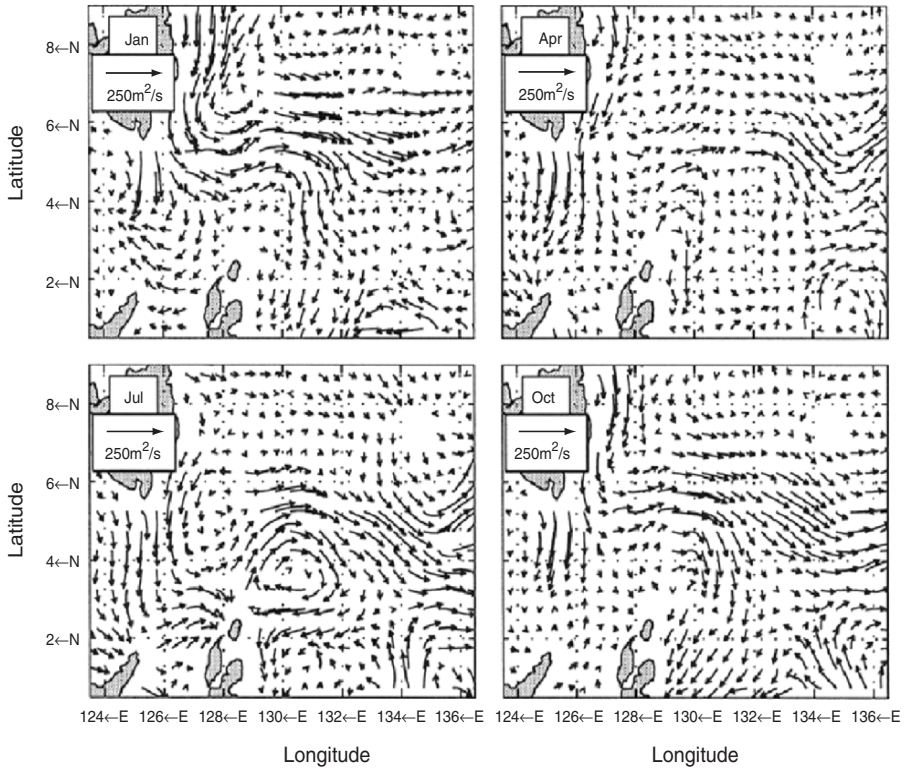

Fig. 11.11. Seasonal variability of vertically integrated velocity vectors (from Chu and Fan 2006, Journal of Marine Systems)

(Fig. 11.13) to represent the seasonal variability of North Equatorial Counter Current volume transport. The dashed, dotted, and solid curves indicate eastward, westward, and net eastward transports, respectively. The westward flow is weaker than the eastward flow for the total transport and the layered transports.

The total transport is positive (eastward) all the year round with a maximum value of 45.7 Sv in January and a minimum value of 20.0 Sv in April with the annual mean transport of 34.4 Sv, which is consistent with the estimation (35 Sv) of Johnson and McPhaden (1999) using the geostrophic calculations relative to a reference surface of 900 dbar.

Transport to the Celebes Sea

Monthly total and layered (between two σ_θ levels) volume transports are computed across 125°15′E (eastward positive) between 2°15′N and 5°45′N (Fig. 11.14) to represent the seasonal variability of volume transport to the

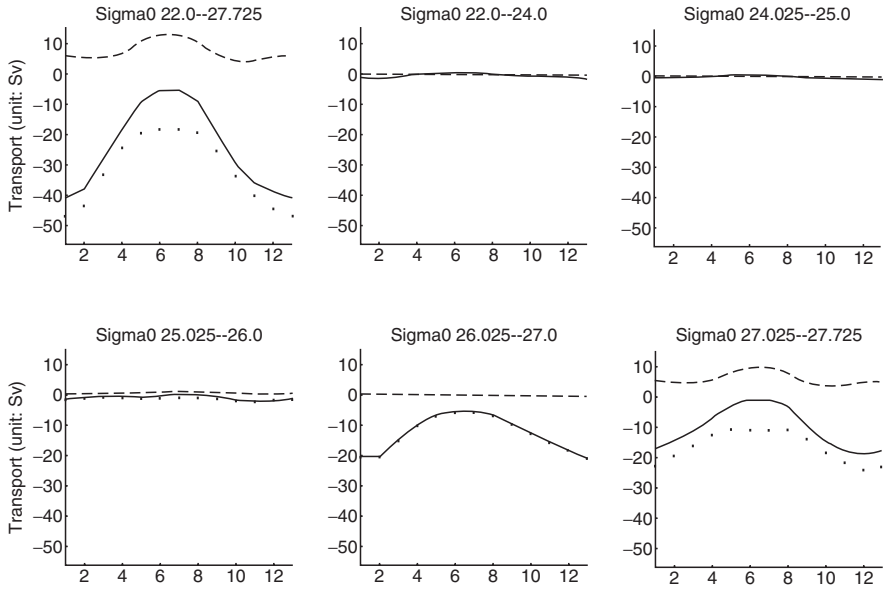

Fig. 11.12. Monthly variation of total and layered (between two σ_θ levels) latitudinal volume transports (northward positive) across 7°156′N latitude between 126°45′ and 130°45′E, representing the Mindanao Current transport (Sv): (**a**) total, (**b**) $\sigma_\theta < 24.0$, (**c**) σ_θ from 24.0 to 25.0, (**d**) σ_θ from 25.0 to 26.0, (**e**) σ_θ from 26.0 to 27.0, and (**f**) $\sigma_\theta > 27.0$. The *dashed*, *dotted*, and *solid* curves indicate the northward, the southward, and the net transports, respectively (from Chu et al. 2003d, Chinese Journal of Oceanology and Limnology)

Celebes Sea. The dashed, dotted, and solid curves indicate eastward, westward, and net transports, respectively. The eastward flow is weaker than the westward flow for the total transport (denoting water entering the Celebes Sea) in January (−16.7 Sv). The strength of the volume transport of the Mindanao Current into the Celebes Sea weakens from winter to spring, and in summer (August), the net transport (4.6 Sv) is eastward that indicates outflow from the Celebes Sea to the Pacific Ocean. The most layered transports are negative (westward) all the year round except the midlayer ($26.0\,\mathrm{kg\ m^{-3}} \geq \sigma_\theta \geq 25.025\,\mathrm{kg\ m^{-3}}$), where the eastward flow is dominant.

Transport to the Molucca Sea

Monthly total and layered (between two σ_θ levels) volume transports across 1°45′N (northward positive) between 125°45′E and 127°25′E (Fig. 11.15) to represent the seasonal variability of volume transport to the Malacca Sea. The dashed, dotted, and solid curves indicate northward, southward, and net transports, respectively. The southward flow (into the Malacca Sea) is

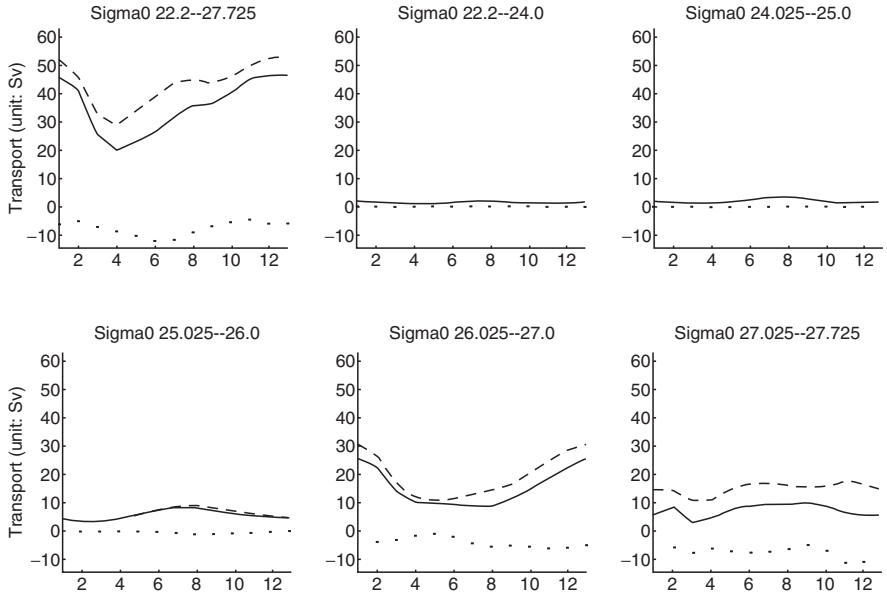

Fig. 11.13. Monthly variation of total and layered (between two σ_θ levels) zonal volume transports across 130°E longitude between 0°45′ and 6°15′E, representing the North Equatorial Counter Current transport (Sv): (**a**) total, (**b**) $\sigma_\theta < 24.0$, (**c**) σ_θ from 24.0 to 25.0, (**d**) σ_θ from 25.0 to 26.0, (**e**) σ_θ from 26.0 to 27.0, and (**f**) $\sigma_\theta > 27.0$. The *dashed*, *dotted*, and *solid* curves indicate the northward, the southward, and the net transports, respectively (from Chu et al. 2003d, Chinese Journal of Oceanology and Limnology)

little weaker than the northward flow (out of the Malacca Sea) for the total transport in January (1.5 Sv).

The net northward volume transport decreases with time. From February to May, the net volume transport is southward with the minimum value of −1.8 Sv in May. After May, the net volume transport becomes northward and enhances from 2.8 Sv in June to 7.9 Sv (maximum value) in August. The southward volume transport (into the Malacca Sea) is evident from January to June in the midlayer (26.0 kg m^{-3} $\geq \sigma_\theta \geq$ 25.025 kg m^{-3}).

Transport to the Halmahera Sea

Monthly total and layered (between two σ_θ levels) volume transports across 1°45′N (northward positive) between 129°30′E and 136°30′E (Fig. 11.16) to represent the seasonal variability of volume transport to the Halmahera Sea. The dashed, dotted, and solid curves indicate northward, southward, and net transports, respectively. The southward flow (into the Halmahera Sea) is stronger than the northward flow (out of the Halmahera Sea) for the total transport in most of the year except in June and July. The net

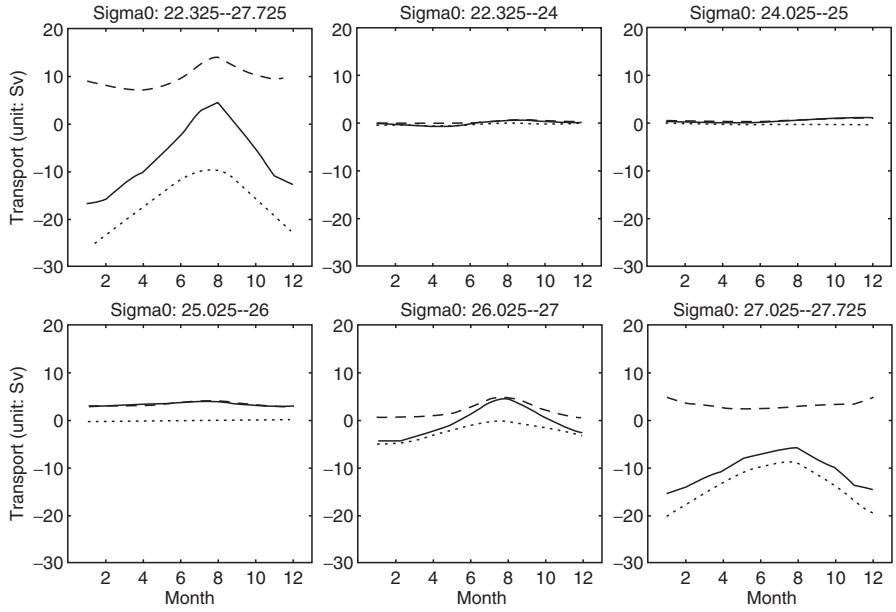

Fig. 11.14. Monthly variation of total and layered (between two σ_θ levels) zonal volume transports across 125°15′E (eastward positive) longitude between 2°15′N and 5°45′N, representing the volume transport (Sv) between the Celebes Sea and Pacific Ocean: (**a**) total, (**b**) $\sigma_\theta < 24.0$, (**c**) σ_θ from 24.0 to 25.0, (**d**) σ_θ from 25.0 to 26.0, (**e**) σ_θ from 26.0 to 27.0, and (**f**) $\sigma_\theta > 27.0$. The *dashed*, *dotted*, and *solid* curves indicate the northward, the southward, and the net transports, respectively (from Chu et al. 2003d, Chinese Journal of Oceanology and Limnology)

southward volume transport (into the Halmahera Sea) reaches the maximum strength (−19.6 Sv) in January. The net southward volume transport weakens from January to March (−4.5 Sv) and then strengthens from March to May (−16.4 Sv) with time. The net volume transport is positive (out of the Halmahera Sea) in June (5.6 Sv) and July (11.9 Sv). The net volume transport is southward from August (−3.5 Sv) to December (−18.2 Sv). The southward volume transport (into the Halmahera Sea) is dominant in the two deep layers ($27.0\,\mathrm{kg\ m^{-3}} \geq \sigma_\theta \geq 26.025\,\mathrm{kg\ m^{-3}}$) and ($27.725\,\mathrm{kg\ m^{-3}} \geq \sigma_\theta \geq 27.025\,\mathrm{kg\ m^{-3}}$).

11.3 Indonesia Throughflow

The Indonesian Throughflow is the only interbasin exchange of water at low latitudes from the Pacific to the Indian Ocean. The calculated monthly mean Ψ and (U, V) fields in the vicinity of Indonesia (Fig. 11.17) shows the volume transport and the depth-integrated circulation pattern have weak

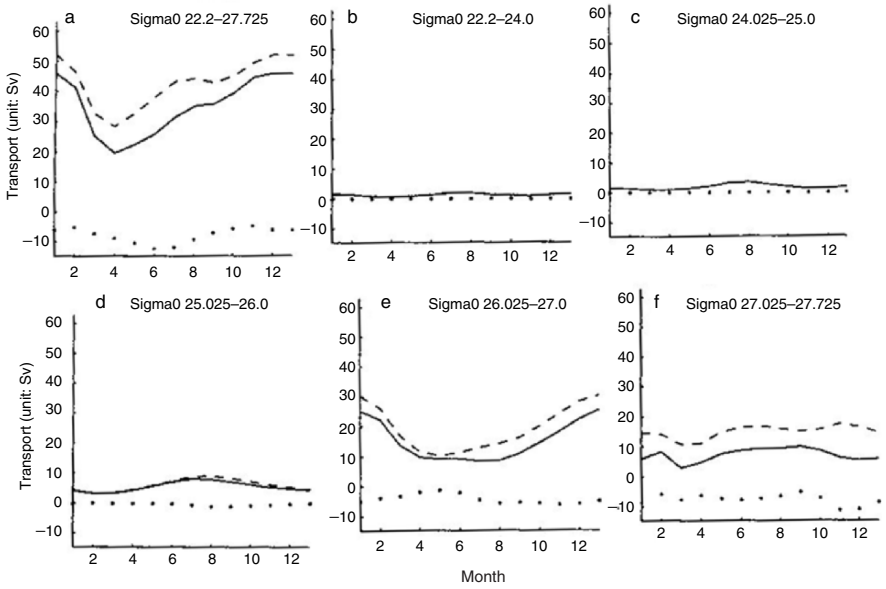

Fig. 11.15. Monthly variation of total and layered (between two σ_θ levels) latitudinal volume transports (northward positive) across 1°45′N latitude between 125°45′E and 127°25′ E, representing the seasonal variability of volume transport to the Malacca Sea: (**a**) total, (**b**) $\sigma_\theta < 24.0$, (**c**) σ_θ from 24.0 to 25.0, (**d**) σ_θ from 25.0 to 26.0, (**e**) σ_θ from 26.0 to 27.0, and (**f**) $\sigma_\theta > 27.0$. The *dashed*, *dotted*, and *solid* curves indicate the northward, the southward, and the net transports, respectively (from Chu et al. 2003d, Chinese Journal of Oceanology and Limnology)

seasonal variations and are quite similar from the surface to intermediate depth currents shown in the earlier description (e.g., Fine et al. 1994; Lukas et al. 1996; Godfrey 1996): Water from the Pacific Ocean enters the Indonesian seas near the region where the New Guinea Coast Current (10 Sv) meets the Mindanao Current (10–20 Sv), as well through the South Sulu Sea from the South China Sea (Fig. 11.3). The New Guinea Coastal Current transports 10 Sv of water around the Halmahera Eddy and joins the southeastward flowing North Equatorial Counter Current. The North Equatorial Current bifurcates east of the Philippines, with the southern branch becoming the Mindanao Current and the northern branch becoming the Kuroshio. Part of the water flowing southward in the Mindanao Current recirculates 10–20 Sv around the Mindanao Eddy to join the North Equatorial Counter Current while the remainder enters the Celebes Sea, where some South Pacific water passes into the Indonesian seas near Halmahera. The majority of the Indonesian Throughflow water exits to the Indian Ocean through the Timor Strait, with smaller transport through the Savu Sea and Lomok Strait. The

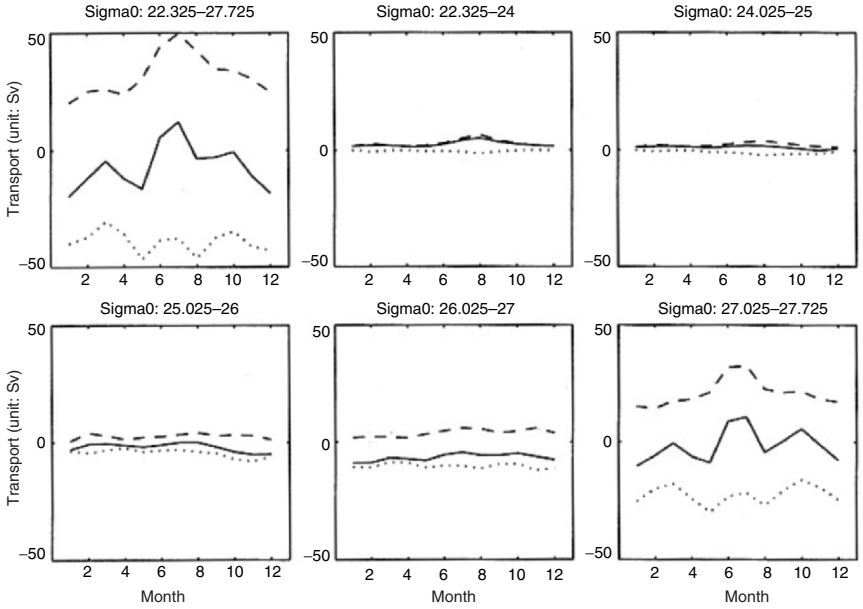

Fig. 11.16. Monthly variation of total and layered (between two σ_θ levels) latitudinal volume transports (northward positive) across 1°45′N latitude between 129°30′ E and 136°30′ E, representing the seasonal variability of volume transport to the Halmahera Sea: (**a**) total, (**b**) $\sigma_\theta < 24.0$, (**c**) σ_θ from 24.0 to 25.0, (**d**) σ_θ from 25.0 to 26.0, (**e**) σ_θ from 26.0 to 27.0, and (**f**) $\sigma_\theta > 27.0$. The *dashed*, *dotted*, and *solid* curves indicate the northward, the southward, and the net transports, respectively (from Chu et al. 2003d, Chinese Journal of Oceanology and Limnology)

Mindanao Eddy (cyclonic) near the southern Philippines and the Halmahera Eddy (anticyclonic) near Indonesia are well represented in the inverted Ψ and (U, V) fields (Fig. 11.3). No strong flow is obtained through the Makassar Strait in the present computation, which is the discrepancy with earlier studies.

The monthly volume transport between Bali (8°S, 113.5°E) and northwest coast of Australia (20°S, 120°E) represents most of the Indonesian Throughflow (Fig. 11.17) and shows a weak seasonal variability with a maximum value of 22.9 Sv in December and a minimum value of 20.3 Sv in August. This agrees qualitatively well with the observational data (16.2 Sv) collected along the same section (Bali to Australia) in August 1989 by Fieux et al. (1994) and with the numerical simulated data (25.7 Sv using the 1.5 reduced gravity model, 15.8 Sv using the nonlinear six-layer model) reported by Morey et al. (1999).

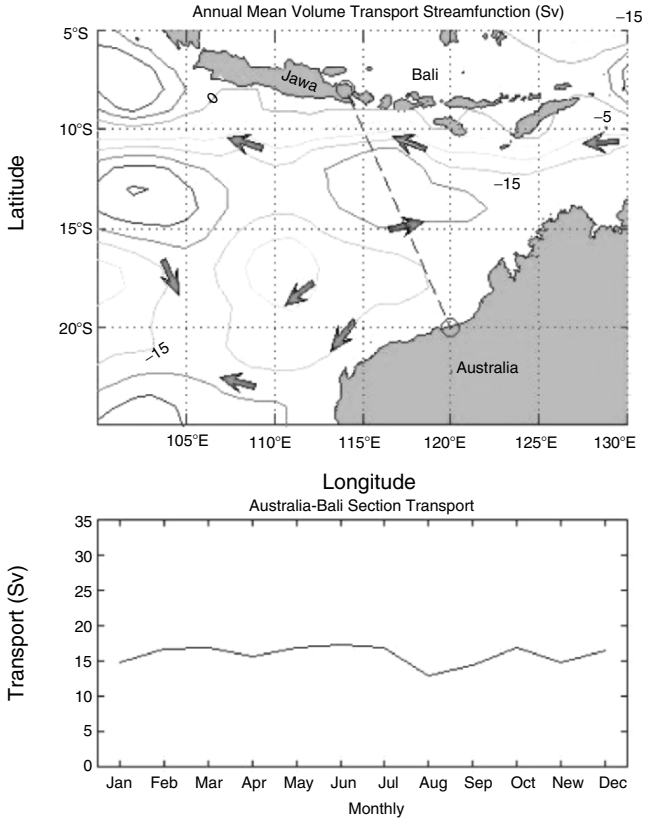

Fig. 11.17. Inverted volume transport between Bali (8°S, 113.5°E) and northwest coast of Australia (20°S, 120°E): (**a**) annual mean Ψ-field, and (**b**) monthly variability (from Chu and Fan 2006, Journal of Marine Systems)

11.4 Kuroshio Transport and its Intrusion into the South China Sea

Difference of the Ψ-values is used between Japan and the center of the subtropical gyre as the Kuroshio volume transport (Fig. 11.18). The monthly Kuroshio volume transport is very steady (very weak seasonal variation) with the transport from 57.7 to 62.4 Sv (Fig. 11.18). Our calculation of the Kuroshio volume transport agrees with Schmitz's (1996b) estimation (52.4 Sv), and larger than Bingham and Talley (1991) estimation (26.3 Sv), using an inverse method and Chen et al.'s (1992) estimation (30.3 Sv), using the geostrophic calculation (referenced to ADCP).

The seasonal variation of the intrusion of the Kuroshio Water into the South China Sea through the Luzon Strait has been investigated by many authors (e.g., Shaw 1989; Chu and Li 2000). Shaw (1989) used the discriminant

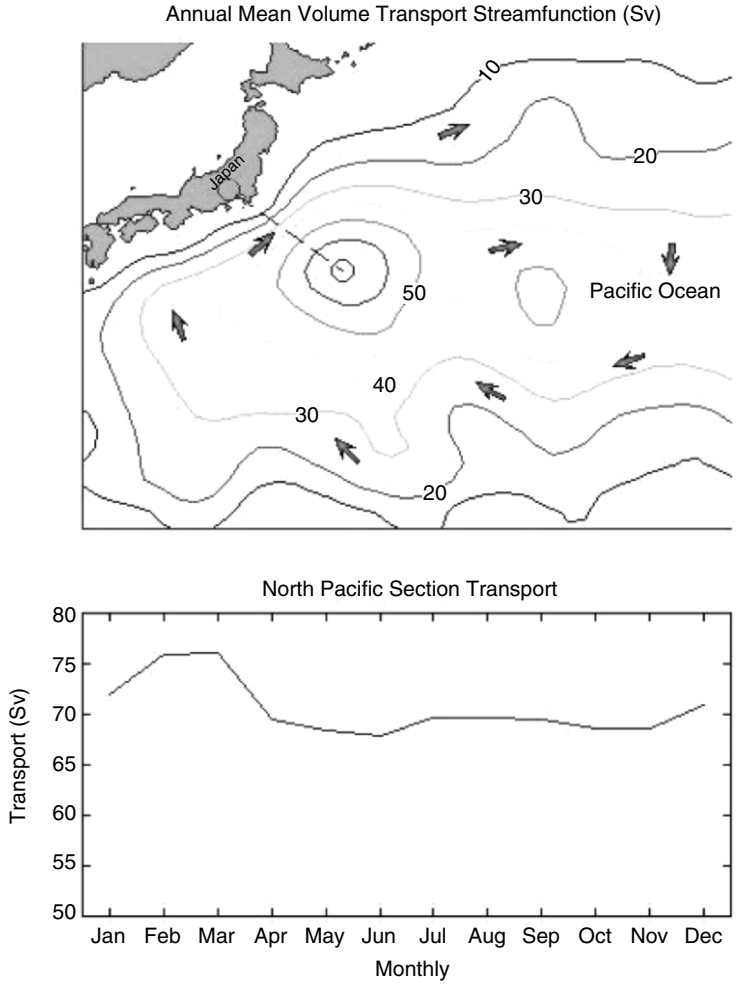

Fig. 11.18. (**a**) Annual mean Ψ field and (**b**) Monthly variation of the Kuroshio transport (from Chu and Fan 2006, Journal of Marine Systems)

analysis method to classify the water mass T, S characteristics at 150, 200, and 250 m, and found that water characteristics of the Philippine Sea (Kuroshio) were identifiable along the continental margin south of China from October to January. The presence of this water indicated an intrusion current from the Philippine Sea into the South China Sea. Chu and Li (2000) used the P-vector inverse method (Chu 1995a, b, 2000) to determine the isopycnal surface geostrophic velocities in the South China Sea. The annual and monthly mean volume transports through the Luzon Strait (Fig. 11.19) show Kuroshio intrusion all the year round with a seasonal variation (8–15 Sv). This estimation is larger than the existing estimations such as 2–3 Sv (Wyrtki 1961a, b), 8–10 Sv

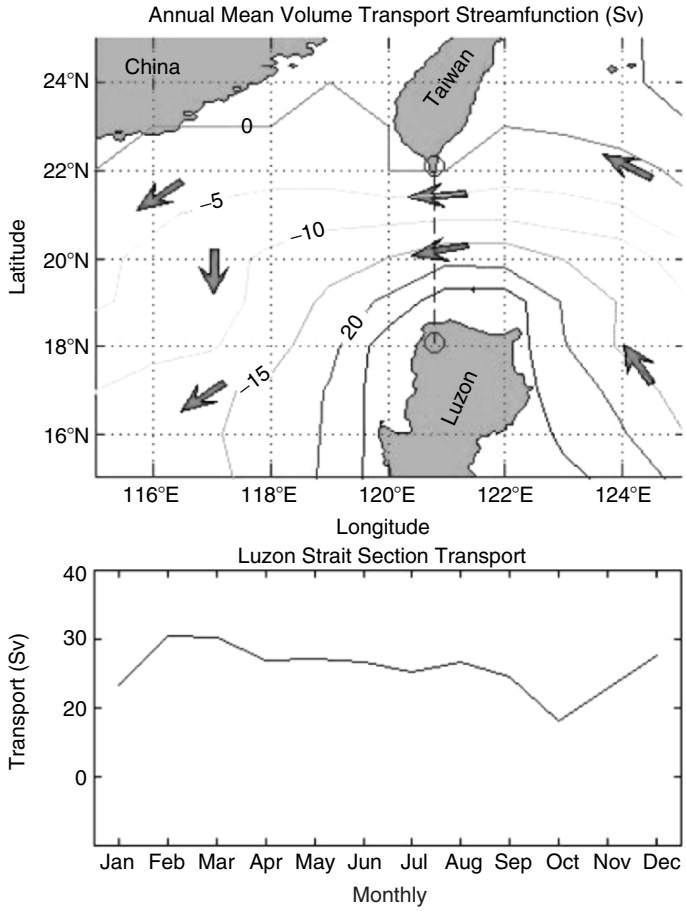

Fig. 11.19. (**a**) Annual mean Ψ field and (**b**) monthly variation of volume transport through the Luzon Strait into the South China Sea (from Chu and Fan 2006, Journal of Marine Systems)

(Huang et al. 1994), 2.4–4.4 Sv (Metzger and Hurlburt 1996), and 1.4–13.7 Sv (Chu and Li 2000) (see Table 6.3).

11.5 Northwest Pacific Subtropical Counter Current on Isopycnal Surface

11.5.1 General Features

One expects a westward flow in the subtropical northwest Pacific (Fig. 11.20), feeding the western boundary current based on the classical wind-driven theory. However, early observations (e.g., Uda 1955) show the occurrence of

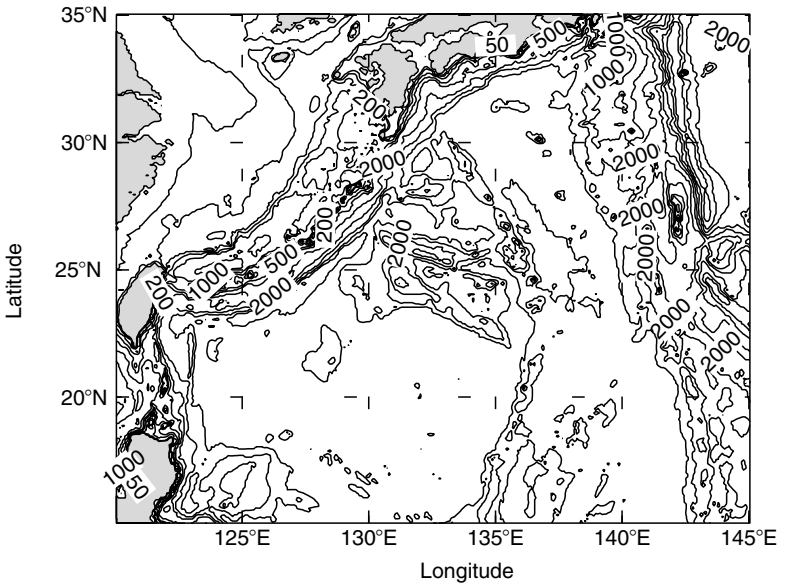

Fig. 11.20. Geography and bottom topography of the Northwestern Pacific (from Chu et al. 2002a, Geophysical Research Letters)

eastward flow segment north of 15°N. Yoshida and Kidokoro (1967a, b) predicted the existence of an eastward current in the subtropical region especially 20–25°N after computing the Sverdrup transport currents from the surface wind stress, and named it as the Subtropical Counter Current. This current was subsequently confirmed by Uda and Hasunuma (1969) from direct current meter observations and geostrophic calculations, and by White et al. (1978), using historical XBT data. Qiu (1999) inferred temporal and spatial variability of Subtropical Counter Current using the altimeter data from the first $5^1/_4$-year TOPEX/Poseidon mission, and found that the eddy kinetic energy of Subtropical Counter Current is maximum in April/May and minimum in December/January. Regardless of the advancement of the knowledge on Subtropical Counter Current, there is still lack of quantitative description of this current such as its origin and spatial variability especially on the isopycnal surface.

11.5.2 Circulations

The P-vector method on the isopycnal surfaces (see Chap. 6) is used to compute the absolute velocity in the northwest Pacific [15–35°N, 120–145°E] from the Navy's GDEM climatological June temperature and salinity data set with $0.5° \times 05°$ resolution (Teague et al. 1990). It is noted that only the geostrophic velocity is obtained using the P-vector method. Near the surface

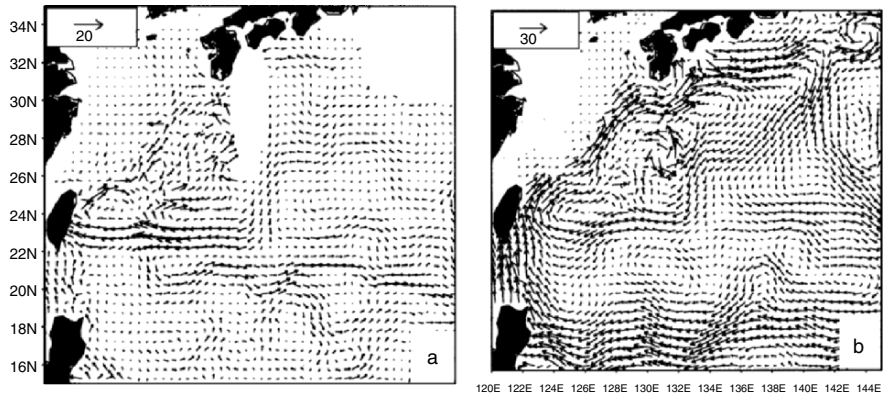

Fig. 11.21. Absolute velocity vectors (unit: cm s^{-1}) in June on isopycnal surface (**a**) $\sigma_\theta = 23.5$, and (**b**) $\sigma_\theta = 25.0$ (from Chu et al. 2002a, Geophysical Research Letters)

the geostrophic current is strong, at least in the Kuroshio. Since the isopycnal $\sigma_\theta = 23.5\,\mathrm{kg\ m^{-3}}$ outcrops at 26–30°N (Fig. 11.21a), the isopycnal surface circulations near $\sigma_\theta = 23.5\,\mathrm{kg\ m^{-3}}$ might not be consistent when the direct measurements are taken, with current meters south of Honsu. Thus, the velocity at $\sigma_\theta = 25.0\,\mathrm{kg\ m^{-3}}$ is chosen to represent the Kuroshio Current and its extension near Honsu (Chu et al. 2002a).

Most important features from the computation are the westward flowing North Equatorial Current, the northeast flowing Kuroshio Current and the associated eddies and recirculation current from Kuroshio, and the eastward flowing Subtropical Counter Current. At $\sigma_\theta = 23.5$, the North Equatorial Current is very weak. The eastward flowing Subtropical Counter Current originates mainly from the southward turning of Recirculation Current from Kuroshio (westward flowing) at (127–128°E, 23°N).

At $\sigma_\theta = 25.0$ (Fig. 11.21b), the North Equatorial Current is quite strong. Between 128 and 134°E a weak current flowing eastward along 21°N is the north flank of an anticyclonic eddy located at 18–21°N, 128–134°E (Fig. 10.21b). Evident eastward flow (i.e., Subtropical Counter Current) occurs east of 135°E, which is different from the Subtropical Counter Current at $\sigma_\theta = 23.5$. At deeper level ($\sigma_\theta = 25.8$), there is no eastward current in the subtropics.

Two theories are available to explain the formation of the Subtropical Counter Current: (a) the Ekman convergence (e.g., Roden 1980) induced by westerlies to the north and trade winds to the south, and (b) the geostrophic convergence, which causes the midgyre front and its associated zonal current (Cushma-Roisin 1984; Kubokawa 1997). Since the velocity is wholly determined by the density structure, the identification of the Subtropical Counter Current at this point tends to confirm the validity of the geostrophic convergence theory. Comparison between Fig. 11.21a, and b shows a strong vertical

shear in the Subtropical Counter Current. The baroclinic instability associated with the vertical shear causes Subtropical Counter Current to meander between 19 and 25°N with the main axis at around 21.5°N, and makes the eddy generation along it. As the Subtropical Counter Current flows eastward entraining water from eddies, it becomes wider with a maximum width of 6° of latitude (18–24°N) at 136–140°E.

11.5.3 Spatial Variability of the Subtropical Counter Current

The spatial variability of the Subtropical Counter Current is represented by four meridional cross sections (127.5°E, 129.5°E, 133.5°E, 138.5°E) of the east–west absolute velocities on isopycnal surfaces (Fig. 11.22).

The Subtropical Counter Current is the eastward flow near the Tropic of Cancer (23.5°N), and occurs in the upper layer above $\sigma_\theta = 25.8$. The core of Subtropical Counter Current is not located at the surface. The axis of this

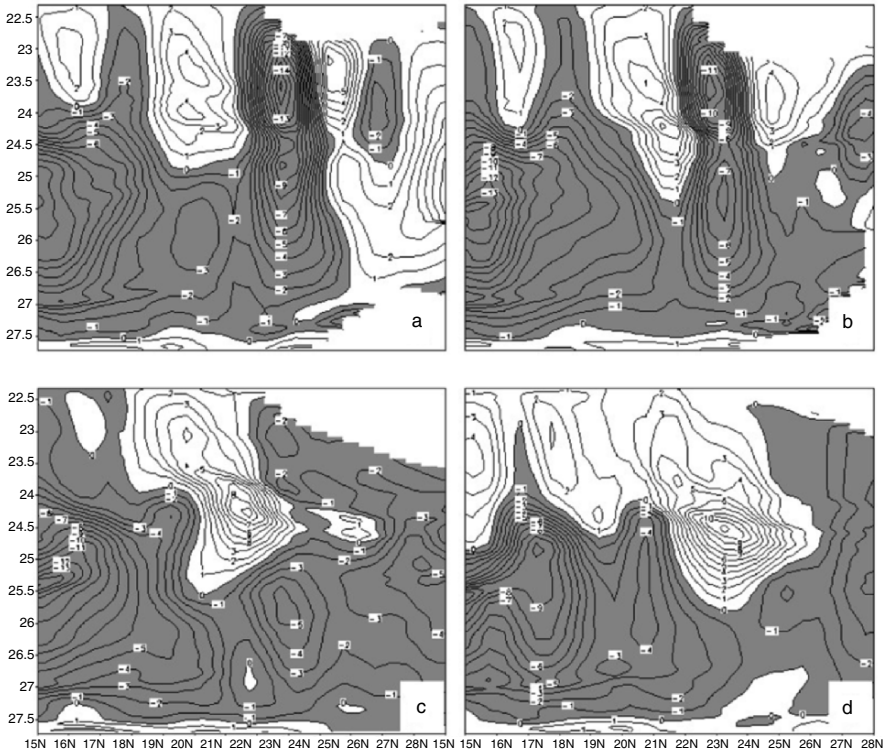

Fig. 11.22. East–west absolute velocity (unit: cm s^{-1}) in June at meridional cross sections: (**a**) 127.5°E, (**b**) 129.5°E, (**c**) 133.5°E, and (**d**) 138.5°E. Here, the *shaded* part (negative values) refers to the westward velocity (from Chu et al. 2002a, Geophysical Research Letters)

Current shifts northward as σ_θ increases and the speed increases eastward. For example, the maximum velocity of Subtropical Counter Current is around $0.04\,\mathrm{m\ s^{-1}}$ near 20°N between $\sigma_\theta = 23.0$ and $\sigma_\theta = 24.0$ at 127.5°E cross section (Fig. 11.22a), greater than $0.06\,\mathrm{m\ s^{-1}}$ near 21°N and $\sigma_\theta = 24.2$ at 129.5°E cross section (Fig. 11.22b), greater than $0.09\,\mathrm{m\ s^{-1}}$ near 21.5°N and $\sigma_\theta = 24.3$ at 133.5°E cross section (Fig. 11.22c), and greater than $0.12\,\mathrm{m\ s^{-1}}$ near 23°N and $\sigma_\theta = 24.5$ at 138.5°E cross section (Fig. 11.22d). At the σ_θ level, where the core of the Subtropical Counter Current is located, the speed of this Current is usually higher than the speed of the North Equatorial Current. This is because the core of the North Equatorial Current is located at deeper layers. The volume transport of the Subtropical Counter Current at 138.5°E is estimated as 8 Sv.

11.5.4 Potential Vorticity

The Subtropical Counter Current mainly comes from southward turning of the recirculation current from Kuroshio, which originates at the southern latitudes (∼15°N) where the potential vorticity is relatively low. Scale analysis shows that the dissipative force alone is not sufficient to remove the low potential vorticity anomalies (Pedlosky 1987) for a narrow boundary current such as the Kuroshio and the recirculation from the Kuroshio. Talley (1988) pointed out the existence of a minimum potential vorticity area corresponding to the subtropical mode water located at $\sigma_\theta = 25.4$ level in the western Pacific. The minimum potential vorticity enclosed by $2.5\times10^{-7}\,\mathrm{m^{-1}s^{-1}}$ at the cross section of 138.5°E (Fig. 11.23) indicates the location of the subtropical mode water. The core of the Subtropical Counter Current is located above the southern boundary of the subtropical mode water (i.e., minimum potential vorticity) from the comparison between Figs. 11.22d and 11.23. This result consists of the recent modeling studies (e.g., Kubokawa 1997).

11.5.5 Major Features

The eastward currents at upper levels (above $\sigma_\theta = 24.5$) reveal multicore structure. The Subtropical Counter Current is located at 19–23°N. Eastward flow segments occurring south of 17°N are usually the southern flanks of local cyclonic eddies rather than a part of a continuous current. Below the level of $\sigma_\theta = 24.5$, the Subtropical Counter Current has a single core located 19–23°N west of 134°E and 22–26°N east of 134°E.

The Subtropical Counter Current originates at 122.5°E at $\sigma_\theta = 23.5$. As σ_θ increases, the origin of the Subtropical Counter Current shifts eastward. The major source of the Current is the southeastward turning of the recirculation current from Kuroshio. This Current strengthens and broadens as it flows eastward. The volume transport of the Subtropical Counter Current at 138.5°E is estimated as 8 Sv.

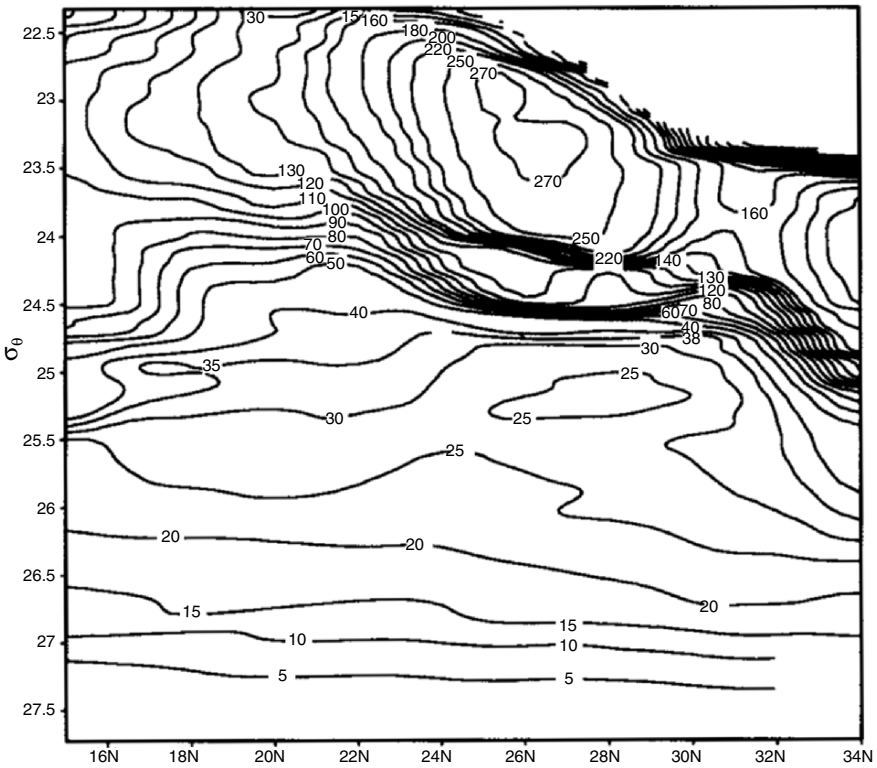

Fig. 11.23. Meridional cross section (138.5°E) of June potential vorticity (in $10^{-10}\,\mathrm{cm^{-1}s^{-1}}$) (from Chu et al. 2002a, Geophysical Research Letters)

The core of the Subtropical Counter Current is not located at the surface, but in the layer between $\sigma_\theta = 23.0$ and $\sigma_\theta = 24.7$, where this Current is stronger than North Equatorial Current. Moreover, the Subtropical Counter Current core is above the southern boundary of the subtropical mode water. The Subtropical Counter Current disappears below the level of $\sigma_\theta = 25.8$, that is to say, this Current is an upper ocean current. Its maximum depth is around 300 m.

11.6 Seasonal Variability of the South China Sea Thermohaline Structure

11.6.1 General Thermal Characteristics

The South China Sea is the largest marginal sea in the West Pacific Ocean. It has a bottom topography that makes it a unique semienclosed ocean basin overlaid by a pronounced monsoon surface wind. Based on limited data sets,

studies show that surface eddies in the South China Sea are predominantly cyclonic in winter and spring and anticyclonic in summer, with sizes ranging from small to mesoscale (Wyrtki 1961a, b; Huang et al. 1994). Both cold and warm eddies exist in the South China Sea. Dale (1956) and Uda and Nakao (1972) reported a cold eddy off the central Vietnamese Coast in summer, and Nitani (1970) found a cold eddy located to the northwest of Luzon. Reports from the South China Sea Institute of Oceanology (1985) indicate that in the central South China Sea a warm-core eddy appears in summer and winter, which is closer to Vietnam in summer at the surface. In addition, a cold-core eddy was detected in the central South China Sea from the 29th December 1993 to 5th January 1994 according to analysis of the TOPEX/Poseidon data (Soong et al. (1995)).

Chu et al. (1997c) and Chu and Chang (1997) identified a central South China Sea surface warm-core eddy in mid-May from a more complete historical data set – the MOODS. From the composite analysis of the US National Centers for Environmental Prediction (NCEP) monthly SST fields (1982–1994), Chu et al. (1997d) found that during the spring-to-summer monsoon transition (March to May) a warm anomaly (greater than 1.8°C) is formed in the central South China Sea at 112°E–119°30′E, 15°N–19°30′N. This warm eddy appears in the central South China Sea (west of Luzon Island) during the late spring season and strengthens until the onset of the summer monsoon (mid-May) and then weakens and disappears at the end of May. Although its size and intensity varies, the warm eddy releases large moisture and heat fluxes into the atmosphere and in turn affects the monsoon circulation. Most of the existing studies on the seasonal eddy variability were based on the surface data. Recently, the seasonal and interannual variability of temperature field was identified by Wang et al. (1999) using the XBT data; and the seasonal and interannual variability of (T, S) fields was identified by Chu et al. (2002c) using the MOODS data. In this section, we present the thermohaline variability using the MOODS data.

11.6.2 Establishment of Monthly Gridded Data from the MOODS

The MOODS for the South China Sea contains 116,019 temperature and 9,617 salinity profiles (Fig. 11.24) from 1964 to 1984. The primary editing procedures included removal of profiles with obviously erroneous location, profiles with large spikes, and profiles displaying features that do not match the characteristics of surrounding profiles. In the shallow water, this procedure can be partially automated, but it also involves subjective interpretation because of the under sampling of MOODS, compared to the spatial and temporal variability of the ocean. Furthermore, vertical resolution and data quality are also highly variable depending much on instrument type and sampling expertise. Temporal and spatial irregularities along with the data resolution and quality problems must be carefully weighed in order to avoid mathematically induced variability.

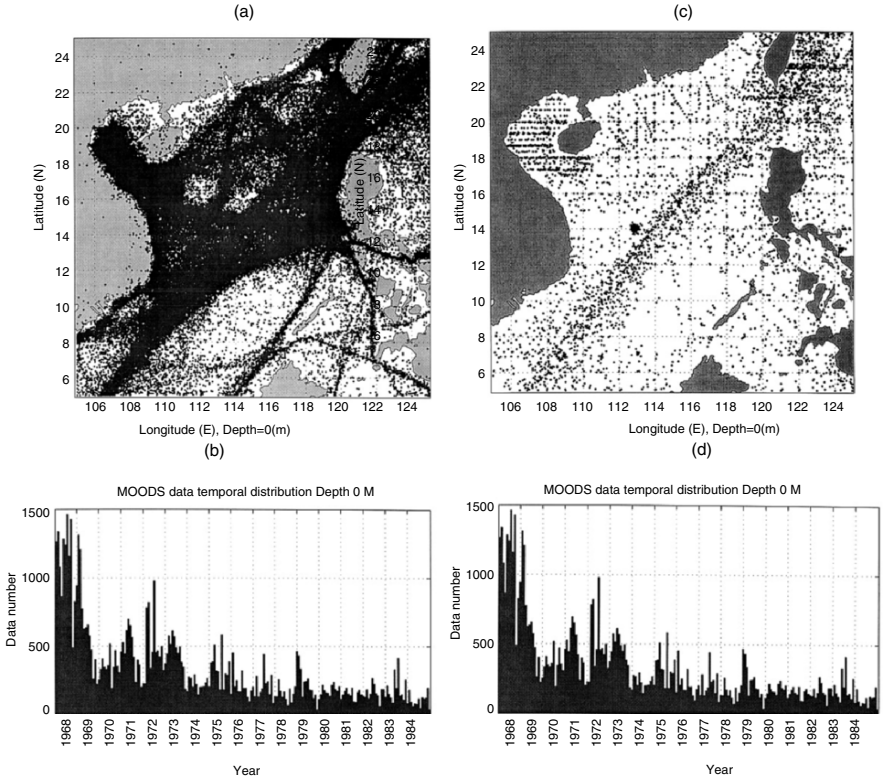

Fig. 11.24. (**a**) Spatial and (**b**) temporal distributions of the MOODS temperature stations, (**c**) spatial and (**d**) temporal distributions of the MOODS salinity stations, during 1964–1984 (from Chu et al. 2002c, Acta Oceanologia Sinica)

The temperature profiles are binned from 1968 to 1984 into monthly data for an individual year which produced 204 temperature data sets. The salinity profiles are binned into monthly climatology data which have 12 mean monthly salinity data sets.

The climatological T, S data are computed from the MOODS data using the z-level analysis. A two-scale optimal interpolation (OI) scheme (Gandin 1965; Lozano et al. 1996) is used to map the MOODS observations to a $0.5° \times 1°$ grid (finer resolution in the zonal direction) at 13 levels (Table 11.1) and to establish monthly climatology of temperature and salinity data set (total 12 fields). The large-scale OI was used to estimate the background mean with a decorrelation scale of 450 km. The mesoscale OI was used to map the observational anomaly from the background mean field into a regular grid with a spatial decorrelation scale of 75 km and a temporal decorrelation scale of 10 days. The spatial and temporal decorrelation scales associated to the mean field were estimated from the covariance matrix obtained from the MOODS

Table 11.1. Standard vertical levels

level	depth (m)	level	depth (m)	level	depth (m)	level	depth (m)
1	**0**	**5**	**50**	**9**	**150**	**13**	**400**
2	**10**	**6**	**75**	**10**	**200**		
3	**20**	**7**	**100**	**11**	**250**		
4	**30**	**8**	**125**	**12**	**300**		

for the South China Sea (Chu et al. 1997c). The large-scale mean was computed using the temperature and salinity profiles. The decorrelation length scale for the fluctuations from the mean was estimated from the MOODS data. The results shown below are relatively insensitive to the length scale in the range of 60–90 km. The decorrelation timescale was selected to ensure synopticity. Our interpolated fields are quite similar to the fields depicted by Chu et al. (2002c), using the cubic spline method.

11.6.3 Composite Analysis

Let $\psi(x_i, y_j, z_k, \tau_l, t_m)$ represent temperature and salinity (withoutτ_l) gridded data, where (x_i, y_j) are the horizontal grids; $z_k = 1, 2, \ldots, 13$, represents vertical levels; $\tau_l = 1968, 1969, \ldots, 1984$, is the time sequence in years; and $t_m = 1, 2, \ldots, 12$, is the time sequence in months. Two temporal averages are defined before investigating the seasonal variation,

$$\bar{\psi}(x_i, y_j, z_k, t_m) = \frac{1}{\Delta\tau} \sum_l \psi(x_i, y_j, z_k, \tau_l, t_m),$$

$$\Delta\tau \equiv 17 \text{ yr } (1968 - 1984), \tag{11.1}$$

which is the long-term monthly (t_m) mean value and

$$\bar{\bar{\psi}}(x_i, y_j, z_k) = \frac{1}{12} \sum_{m=1}^{12} \bar{\psi}(x_i, y_j, z_k, t_m), \tag{11.2}$$

which is the annual mean.

Annual Mean Temperature Field

The annual mean (1968–1984) temperature $\bar{\bar{T}}(x_i, y_j, z_k)$ over the South China Sea shows the pattern of northeast–southwest oriented isotherms at the upper layer from the surface to 75 m depth (Fig. 11.25). The annual surface mean temperature has a rather weak horizontal temperature gradient, decreasing from 28.5°C near the Borneo coast to 25°C near the southeast China coast. A strong temperature front is found near the Luzon Strait in the subsurface layer from 100 to 400 m. In that layer, the water temperature is quite uniform (e.g.,

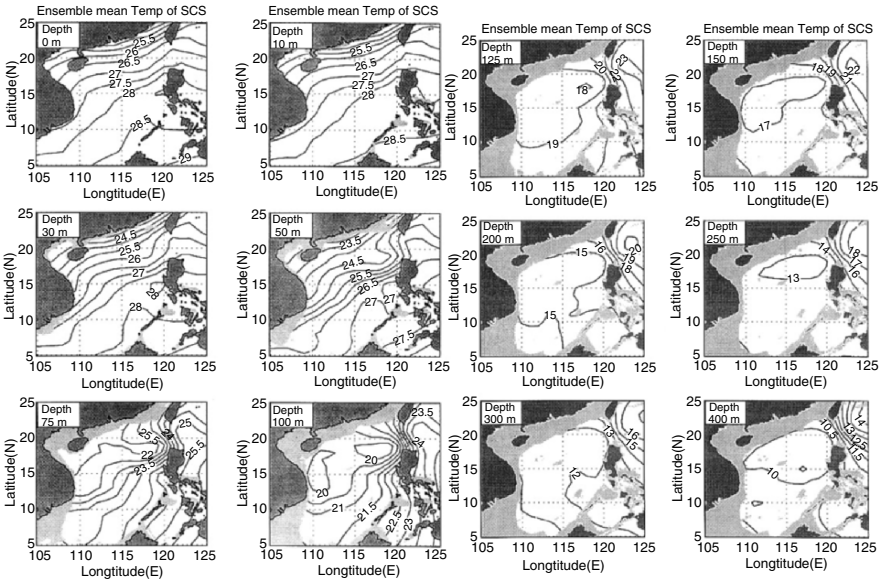

Fig. 11.25. Annual mean temperature (°C) field at 12 different depths from the surface to 400 m (from Chu et al. 2002c, Acta Oceanologia Sinica)

near 15°C at 200 m) and much lower than the water to the east of the Luzon Strait, which is the West Pacific Ocean Water. In the central South China Sea at 15°N zonal cross section (Fig. 11.26), the isotherms of $\bar{\bar{T}}$ bend slightly downward from west to east and no frontal structure is found. However, in the northern South China Sea region at 20°N zonal cross section, the isotherms of $\bar{\bar{T}}$ show a strong frontal structure near 120°E to 125°E, which may suggest two distinguished water masses, the South China Sea water mass (surface and under-surface) and the West Pacific Ocean water mass. The front between the two water masses strengthens from the surface to 400 m depth.

Annual Mean Salinity Field

The annual mean (1968–1984) salinity $\bar{\bar{S}}$ field shows more complexity than temperature. In the upper layer (Fig. 11.27), a large amount of freshwater enters the South China Sea from the Zhujiang (Pearl) River in the northwestern South China Sea and from the Mekong River in the southwest. The Kuroshio brings the salty water through the Luzon Strait into the northern South China Sea and forms a salty tongue (34 ppt) stretching into the southeast China coast (see Fig. 6.27). As the depth increases, both the Kuroshio intrusion and the river run-off effects become less important. At 75 m depth, the Kuroshio intrusion effect is still evident, but not the river run-off effect. Below 200 m depth (Fig. 11.27), the salinity is more uniform (near 34.6 ppt at 200 m) throughout the whole South China Sea.

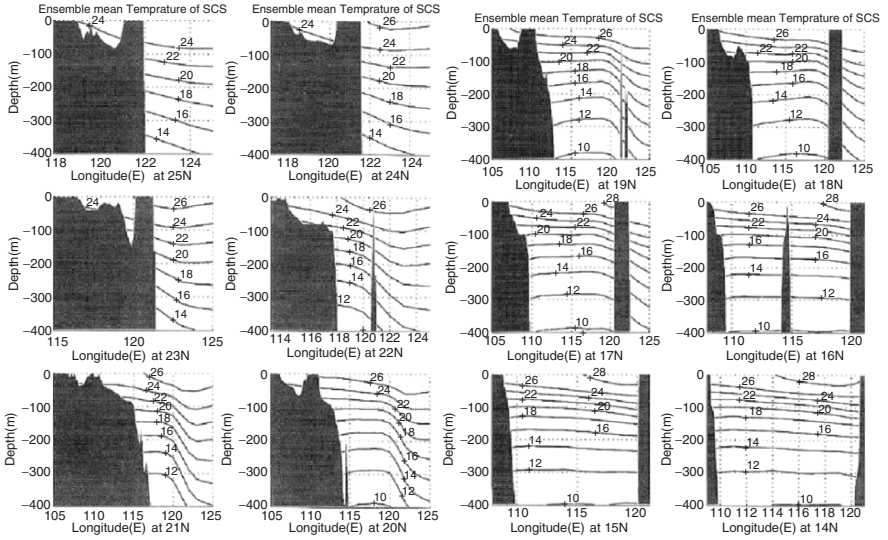

Fig. 11.26. Zonal cross sections of annual mean temperature (°C) field from 25 to 14°N with 1° increment (from Chu et al. 2002c, Acta Oceanologia Sinica)

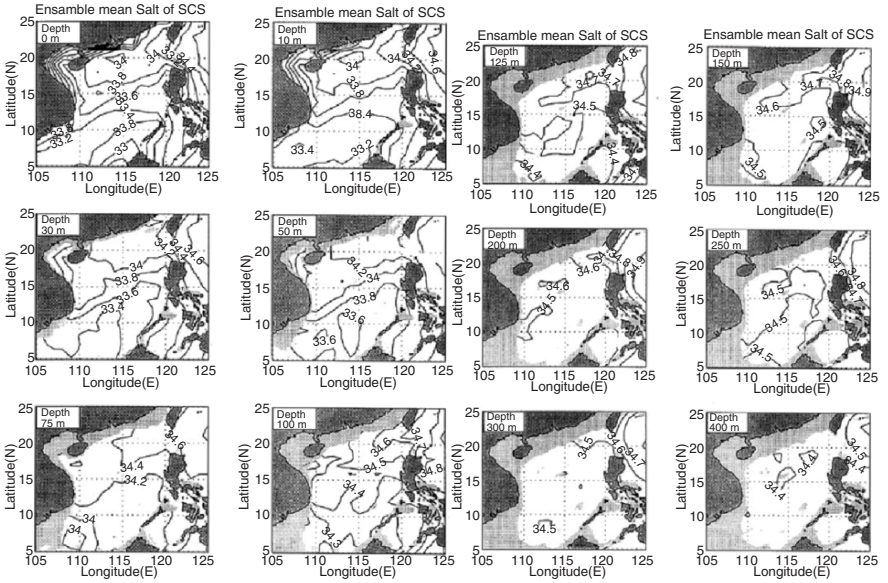

Fig. 11.27. Annual mean salinity (ppt) field at various depths from the surface to 400 m depth (from Chu et al. 2002c, Acta Oceanologia Sinica)

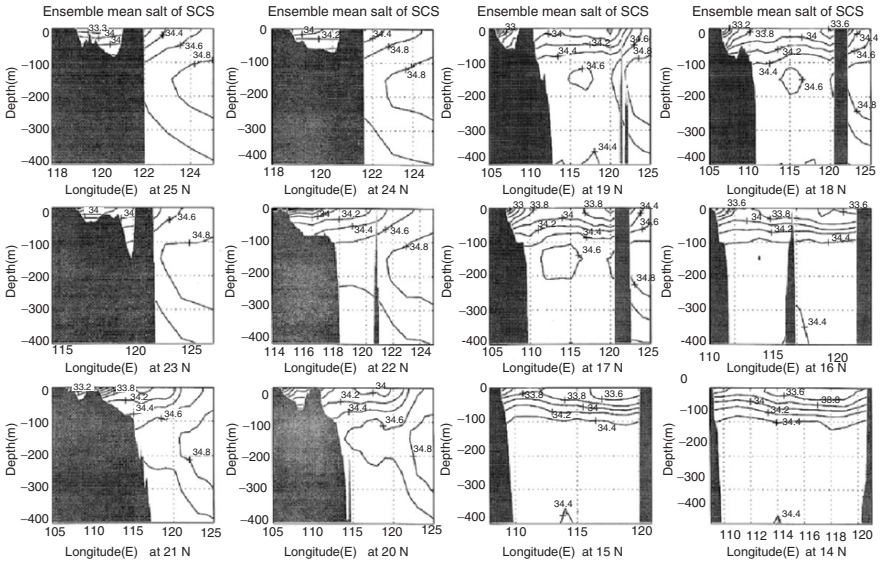

Fig. 11.28. Zonal cross sections of annual mean salinity (ppt) field from 25 to 14°N with 1° increment (from Chu et al. 2002c, Acta Oceanologia Sinica)

In the central region near 15°N zonal cross section (Fig. 11.28), the isohalines of $\bar{\bar{S}}$ are almost parallel to the isobaths in the upper 100 m. Below 100 m depth, the salinity is very uniform (34.4 ppt). However, in the northern region near 20°N zonal cross section (Fig. 11.28), the 34.6 ppt isohaline clearly shows the Kuroshio intrusion from the Luzon Strait into the northern South China Sea in the layer between 100 and 220 m reaching 115°E.

Monthly Mean Temperature Anomalies

The long-term monthly mean values relative to the ensemble mean, $\bar{\bar{T}}(x_i, y_j, z_k)$,

$$\hat{T}(x_i, y_j, z_k, t_m) = \bar{T}(x_i, y_j, z_k, t_m) - \bar{\bar{T}}(x_i, y_j, z_k), \tag{11.3}$$

is defined as the monthly mean anomalies, which represent the composite features of the monthly mean thermal variability. The seasonal SST variation obtained from the MOODS consists of the earlier investigations based on the NCEP data (Chu et al. 1997d). During winter (January), $\hat{T}$ is negative almost everywhere throughout the whole South China Sea (Fig. 11.29).

The typical winter (January) pattern contains northeast-to-southwest oriented isotherms in the northern South China Sea (north of 12°N), a warm anomaly ($\hat{T} > -1.2$°C) west of Borneo–Palawan islands, and a cool anomaly ($\hat{T} < -2.4$°C) near the South Vietnam coast (south of 12°N). The spring-to-summer transition (March to May) pattern shows the northward expansion of the warm anomaly west of Borneo–Palawan islands and the formation

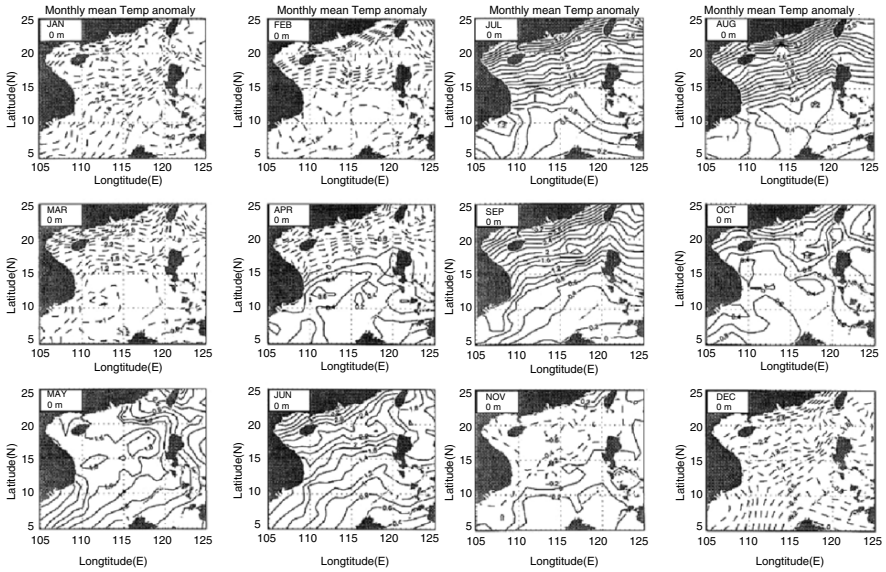

Fig. 11.29. Monthly mean surface temperature anomalies (°C) (from Chu et al. 2002c, Acta Oceanologia Sinica)

of a central South China Sea (10–15°N) warm anomaly with $\hat{T} > 0.6$°C. The isotherm line of 1°C encloses almost all the South China Sea in May.

The summer (July) pattern is characterized by northeast-to-southwest oriented isotherms in the northern South China Sea (north of 15°N) (Fig. 11.29), a cool anomaly ($\hat{T} < 0.4$°C) occurs west of Borneo–Palawan islands, and a warm anomaly ($\hat{T} > 1.2$°C) near the South Vietnamese coast (south of 12°N). The summer pattern is opposite to the winter pattern. The fall-to-winter transition (September to November) pattern shows the northward expansion of the cool anomaly west of Borneo–Palawan islands and the formation of the central South China Sea (10–15°N) cool anomaly.

At 200 m depth (intermediate level), the seasonal variation of temperature is featured by a basin-wide cool eddy ($\hat{T} < -0.8$°C), a strong warm eddy ($\hat{T} > 0.8$°C) near the South Chinese coast, and a weak warm eddy ($\hat{T} > 0.2$°C) west of Borneo–Palawan islands during winter (Fig. 11.28) and a basin-wide warm eddy ($\hat{T} > 0.4$°C), and a weak cool eddy ($\hat{T} < 0$°C) near the South Vietnamese coast (south of 12°N) during summer (Fig. 11.30).

Near the western Luzon coast, a cool eddy ($\hat{T} < -1.0$°C) occurs in winter and a warm eddy ($\hat{T}° > -0.8$°C) appears in summer. The weak WBP warm eddy strengthens, expands toward the northeast in spring (Fig. 11.30), gradually occupies the whole South China Sea, and turns to the summer pattern in July (Fig. 11.30). In autumn, the weak cool eddy near the South Vietnamese coast strengthens and expands toward northeast, and gradually occupies the

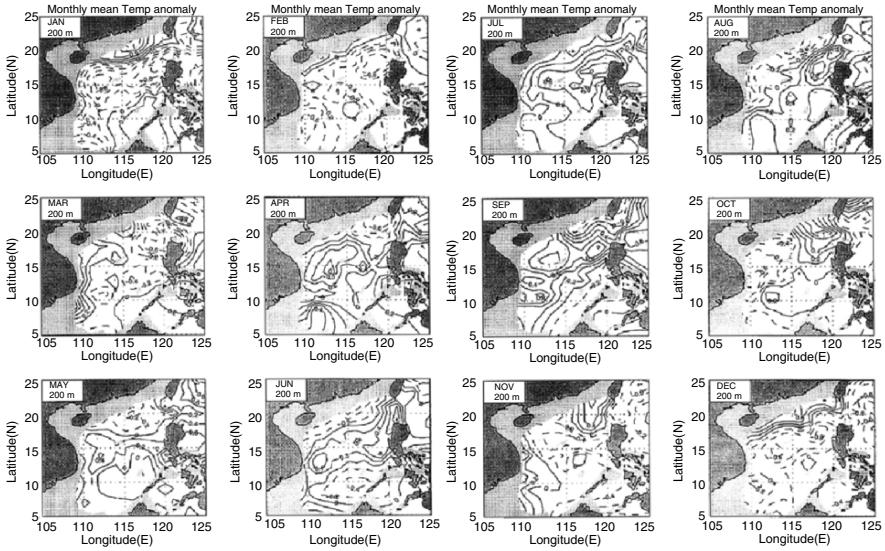

Fig. 11.30. Monthly mean temperature anomalies (°C) at 200 m depth (from Chu et al. 2002c, Acta Oceanologia Sinica)

whole South China Sea, and turns to the winter pattern in January. Below 300 m depth, there is no significant seasonal variability.

The zonal cross section of $\hat{T}$ along 19°N, shows the vertical structure of the winter cool eddy and the summer warm eddy near the western Luzon coast (Fig. 11.31). Both winter cool-core and summer warm-core eddies reach 250 m depth. The winter cool-core ($\hat{T} < -3$°C) and the summer warm-core ($\hat{T} > 2.5$°C) are located between 50 and 100 m depth.

Monthly Mean Salinity Anomalies

The monthly mean salinity anomaly $\hat{S}$ is evident only in the layer above 200 m depth, and very weak below 200 m depth. Surface salinity has a strong seasonal variability. During winter (January), $\hat{S}$ is positive almost everywhere throughout the whole South China Sea except near the South Vietnamese coast and the Gulf of Tonkin (Fig. 11.32).

A salty tongue with $\hat{S} > 0.4$ ppt stretches from the Luzon Strait to the continental shelf along the southeast China coast, representing a strong Kuroshio intrusion. Another weak fresh eddy with $\hat{S} < -0.2$ ppt is found west of Luzon Island. During summer (July), a salty tongue with $\hat{S}$ around 0.4 ppt stretches from the Vietnamese coast to 118°E between 10 and 17°N, occupying the central South China Sea (Fig. 11.32). The rest of the area is occupied by negative $\hat{S}$. A strong fresh tongue occupies the continental shelf along the southeast China coast and the Gulf of Tonkin.

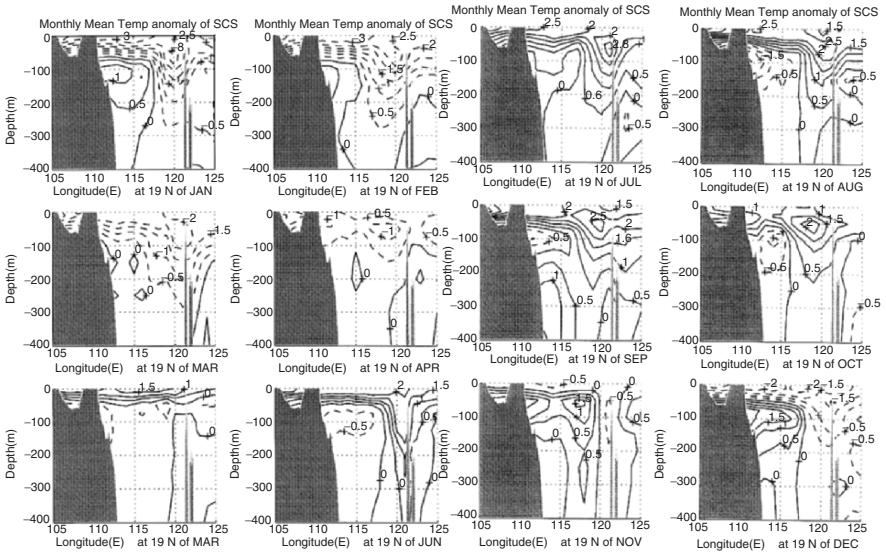

Fig. 11.31. Zonal cross sections of monthly mean temperature anomalies (°C) at 19°N (from Chu et al. 2002c, Acta Oceanologia Sinica)

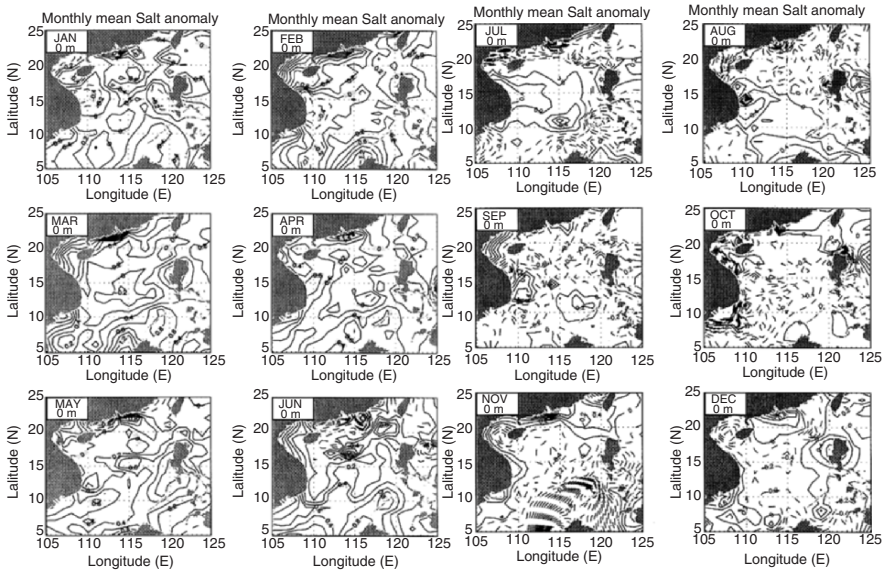

Fig. 11.32. Monthly mean surface salinity anomalies (ppt) (from Chu et al. 2002c, Acta Oceanologia Sinica)

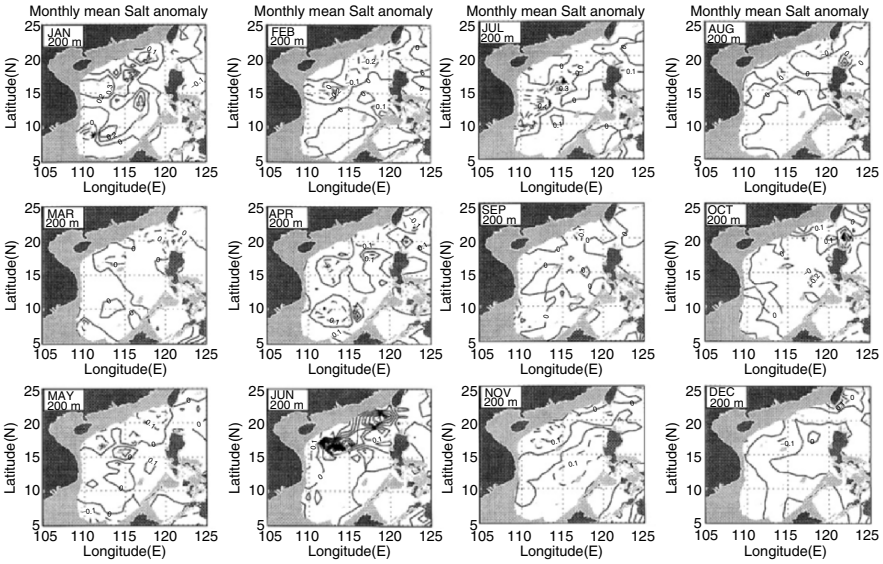

Fig. 11.33. Monthly mean salinity anomalies (ppt) at 200 m depth (from Chu et al. 2002c, Acta Oceanologia Sinica)

At 200 m depth, the seasonal variation of $\hat{S}$ is also evident. In winter (Fig. 11.33), positive $\hat{S}$ with a maximum value of 0.3 ppt occupies most of the area of the South China Sea, except the southwest corner near the Mekong River, where $\hat{S}$ is negative (-0.4 ppt). In summer (Fig. 11.33), a narrow fresh tongue with a minimum value of -0.4 ppt stretches northeastward from the southwest corner near the Mekong River to 20°N (Fig. 11.33).

11.7 Seasonal Variability of the South China Sea Circulation

The P-vector inverse method in z-coordinate (see Chap. 6) is used to compute the absolute velocity from monthly mean T, S fields described in the previous section.

11.7.1 General Description

The most obvious features of the inverted summer and winter South China Sea circulation are flow separation, basin gyres, and mesoscale eddies. Hinted in Wyrtki's (1961a, b) depiction but more explicit in our computation, are the upper level (10 m depth) west-to-east cross-basin currents, which are almost parallel to 16°N latitude from February to July. The inverted monthly South China Sea circulation agrees quite well with earlier observational

study (Wyrtki 1961a, b). As the commonly used inverse methods, the P-vector inverted western boundary currents are rather small. This could be caused by the neglect of relative vorticity in the potential vorticity calculation (Chu 1995a).

11.7.2 Surface Circulation

During the winter monsoon period (November to March), the winter Asian high pressure system brings strong winds from the northeast and the South China Sea surface circulation pattern is cyclonic (Wyrtki 1961a, b). At the surface inflow from the Luzon Strait (the Kuroshio intrusion) turns southwest along the Asian continental shelf, then turns south along the coast of Vietnam (Fig. 11.34). In November, this current splits into two currents at 12°N: a southward along-shore current and an eastward off-shore current. The southward branch turns east at 6°N, then turns northeast and joins the eastern branch at 115°E. An evident multieddy structure is obtained with two cyclonic eddies in the northern South China Sea (north of 12°N) and cyclonic and anticyclonic eddies in the southern South China Sea (south of 12°N). The eddy near Luzon was first identified by Nitani (1970) from the surface data. It is called the Luzon cyclonic eddy. The flow pattern does not change very much from November to December, except the cyclonic eddy near the Luzon Strait strengthens. In January, the west cyclonic eddy in the northern South China Sea expands toward the south. In March, the west cyclonic eddy in the northern South China Sea disappears and instead a cross-basin flow appears along 16°N latitude and joins the cyclonic eddy near the Luzon Strait. The southern South China Sea is occupied by an anticyclonic eddy. This anticyclonic eddy expands to the north and forms the only evident eddy in the central South China Sea in March (Fig. 11.34). This eddy is associated with the central South China Sea warm eddy in spring (Fig. 11.34) and expands toward the south in April. May is the month of the summer monsoon transition. The anticyclonic eddy reduces its strength and becomes unidentifiable.

During the summer monsoon period (mid-May to August), winds blow from the southwest and the surface circulation generally follows suit with anticyclonicity in the southern basin (Wyrtki 1961a). Inflow is through the southern boundary and outflow is through the northern Taiwan Strait and eastern Luzon Strait. The position of the inverted July indicates that the general circulation pattern has the following features. Velocities reach $0.2\,\mathrm{m\ s^{-1}}$ near the Vietnam Coast and split into two currents at 12°N: the coastal current and off-shore current. The off-shore current further bifurcates and partially leaves the coast; the bifurcation point is at 110°E. The northern branch moves northeast to 113°E and then turns zonally between 15 and 18°N. The southern branch moves zonally until on reaching Palawan Island, then turns north and joins with the north branch at 16°N. A cyclonic eddy appears in July near the South Vietnam coast and strengthens in August. This eddy was reported by Dale (1956) and Uda and Nakao (1974).

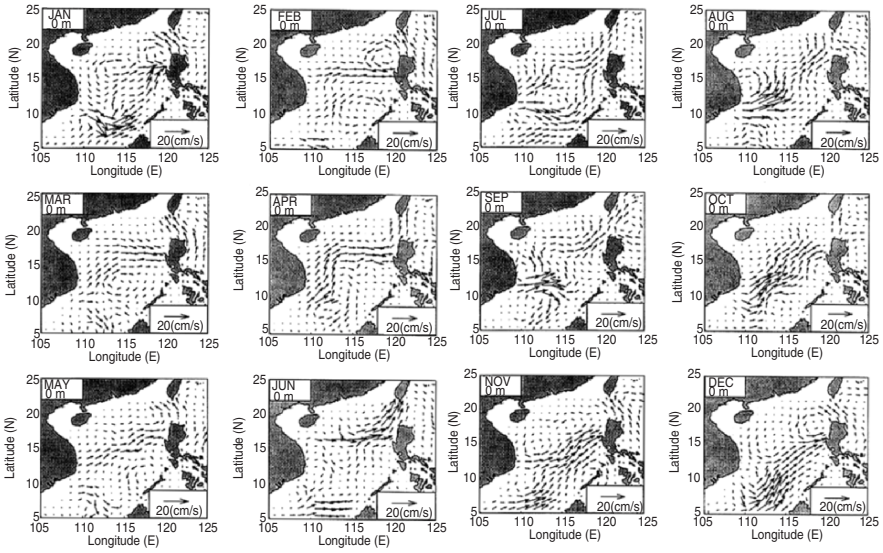

Fig. 11.34. Inverted monthly mean surface circulation (from Chu et al. 2002c, Acta Oceanologia Sinica)

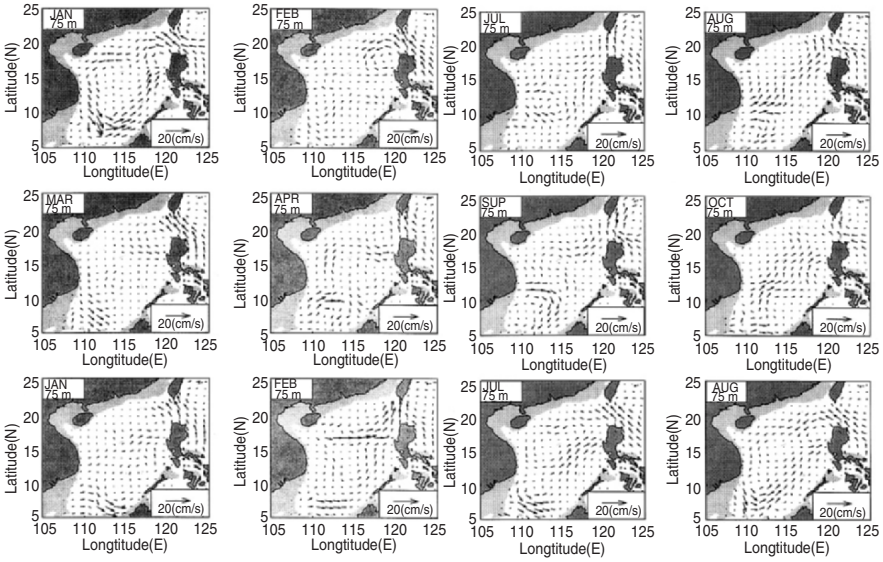

Fig. 11.35. Inverted monthly mean subsurface (75 m) circulation (from Chu et al. 2002c, Acta Oceanologia Sinica)

11.7.3 Subsurface (75 m)

The subsurface (75 m) shows a strong seasonal variation (Fig. 11.35). Warm and salty Kuroshio water enters the South China Sea through the Luzon Strait

in October–March, the transition to and during the winter monsoon season. The winter circulation pattern is the basin-wide cyclonic gyre. A cyclonic mesoscale eddy splits from the gyre near the Luzon Strait in January and keeps its strength in February. On the other hand, the basin-wide cyclonic gyre weakens and shrinks toward the southwest in February and disappears in March.

During the summer monsoon period (June–September), the Kuroshio intrusion through the Luzon Strait ceases. A weak anticyclonic eddy occurs in June near the South Vietnam coast and strengthens in July. A cross-basin current establishes in August from the north branch of that eddy to the Luzon Strait and forms a weak cyclonic gyre in the northwest and an anticyclonic gyre in the southeast. During the winter monsoon transition period, the southeast anticyclonic gyre weakens and the northeast cyclonic gyre gains strength and eventually it occupies the whole South China Sea, indicating the beginning of the winter circulation pattern.

11.7.4 Intermediate Level (150 m)

As the water depth increases, the inverted velocity generally reduces with depth. We choose 150 m depth as a representative of the intermediate level (Fig. 11.36). The seasonal circulation variability is featured by strengthening, weakening, and splitting of a basin-wide cyclonic gyre. This gyre is evident to strengthen in winter and weakens in summer. As spring approaches (March),

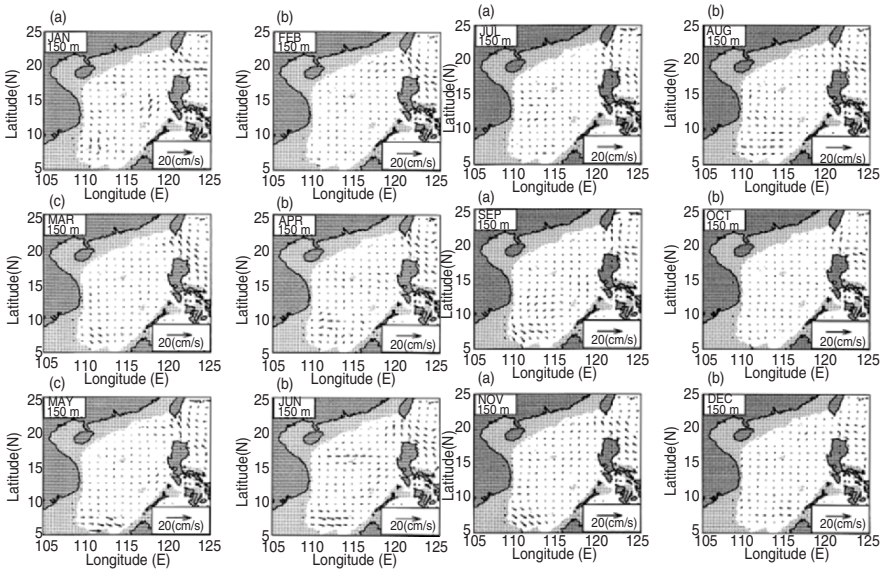

Fig. 11.36. Inverted monthly mean intermediate level (150 m) circulation (from Chu et al. 2002c, Acta Oceanologia Sinica)

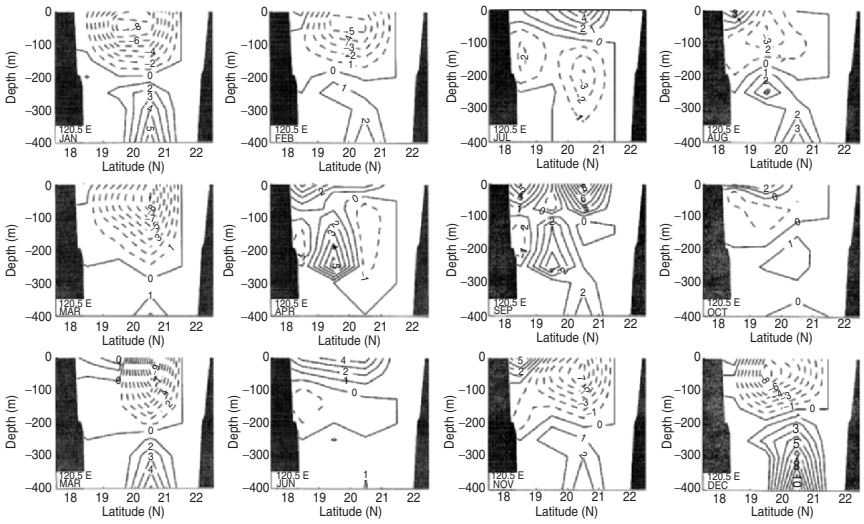

Fig. 11.37. Inverted monthly upper layer (0–400 m) mean zonal velocity across the Luzon Strait (120°E) (from Chu et al. 2002c, Chinese Journal of Oceanology)

a cyclonic eddy in the area northwest of Luzon occurs and the cyclonic gyre is located south of 16°N. In summer (July), the cyclonic gyre is pushed further south and a cyclonic eddy appears off the central Vietnam coast (14–18°N).

The South China Sea joins the Pacific Ocean through the Luzon Strait. The seasonal variations of the intrusion of the Kuroshio Water into the South China Sea through the Luzon Strait have been investigated in earlier studies (Fan and Yu 1981; Shaw 1989, 1991). As pointed out by Shaw (1991), the intrusion process is important not only to the transport of water masses into the South China Sea, but also to the shelf circulation off the southeast coast of China. Shaw (1989, 1991) used the discriminant analysis method to classify the water mass T, S characteristics at 150, 200, and 250 meters, and found that water characteristics of the Philippine Sea (Kuroshio) were identifiable along the continental margin south of China from October to January. The presence of this water indicated an intrusion current from the Philippine Sea into the South China Sea. The monthly zonal velocity in 120.5°E cross section is given in Fig. 11.37. The negative values indicate westward flow through the Luzon Strait (Kuroshio intrusion). The positive values show the outflow from the South China Sea to the Philippine Sea. Flow through the Luzon Strait has a strong seasonal variation, as well as a vertical shear. Evident Kuroshio intrusion (negative values) occurs during the winter monsoon season (November–March) in the upper 200 m. Below 200 m, the velocity is quite small, and most values are positive.

11.8 South China Sea Thermohaline Front

NASA's MCSST data clearly show the appearance of a cross basin, thermal front in winter (Fig. 11.38a) and disappearance of such a front in summer (Fig. 11.38b). In Sect. 10.6, the monthly mean upper layer (0–400 m) T, S data are computed at 13 depths (z-level analysis) using the OI method. An upper layer thermohaline front across the South China Sea basin can also be identified from Figs. 11.25 and 11.27 from the South Vietnamese coast (around 15°N) to Luzon Island (around 19°N). Is this thermohaline front realistic or unrealistic (computationally generated)? To answer this question, the climatological T, S dataset calculated using the curve-fitting model (i.e., GDEM) is used to identify the existence of this front (Chu and Wang 2003).

11.8.1 Thermohaline Front Identified Using GDEM

The SST variation obtained from the GDEM data is quite consistent with the monthly mean data obtained using the z-level analysis (Fig. 11.25). An important feature, yet to be explored, is the thermohaline front across the South China Sea basin from Vietnam Bight (109°E, 10°N) to the northwestern tip of Luzon (120°E, 19°N). Figure 11.39 shows the monthly mean sea surface temperature with contour interval of 0.5°C.

The horizontal gradient across the thermohaline front strengthens in the winter monsoon season (November to April) with a maximum value of 1.4°C/100 km and weakens drastically in the summer monsoon seasons (June to September). Figure 11.40 shows the monthly mean temperature at 50 m depth. Different from the surface, the temperature gradient is evident all the year round.

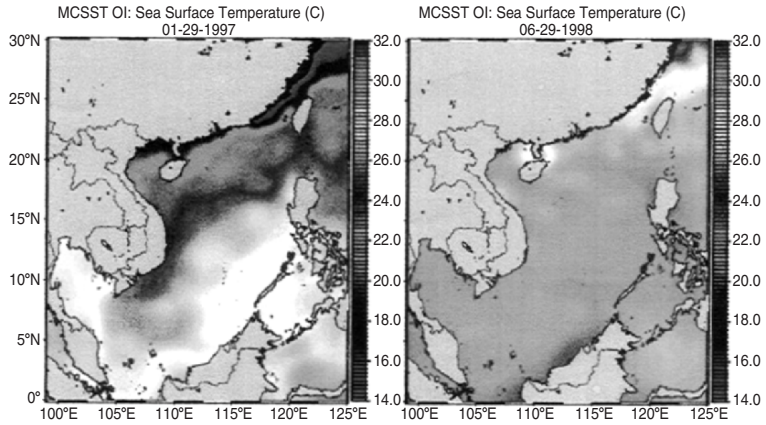

Fig. 11.38. NASA's MCSST data for (**a**) January 29, 1997, and (**b**) June 29, 1998. The data were interpolated by the Naval Research Laboratory (from Chu and Wang 2003, Journal of Oceanography)

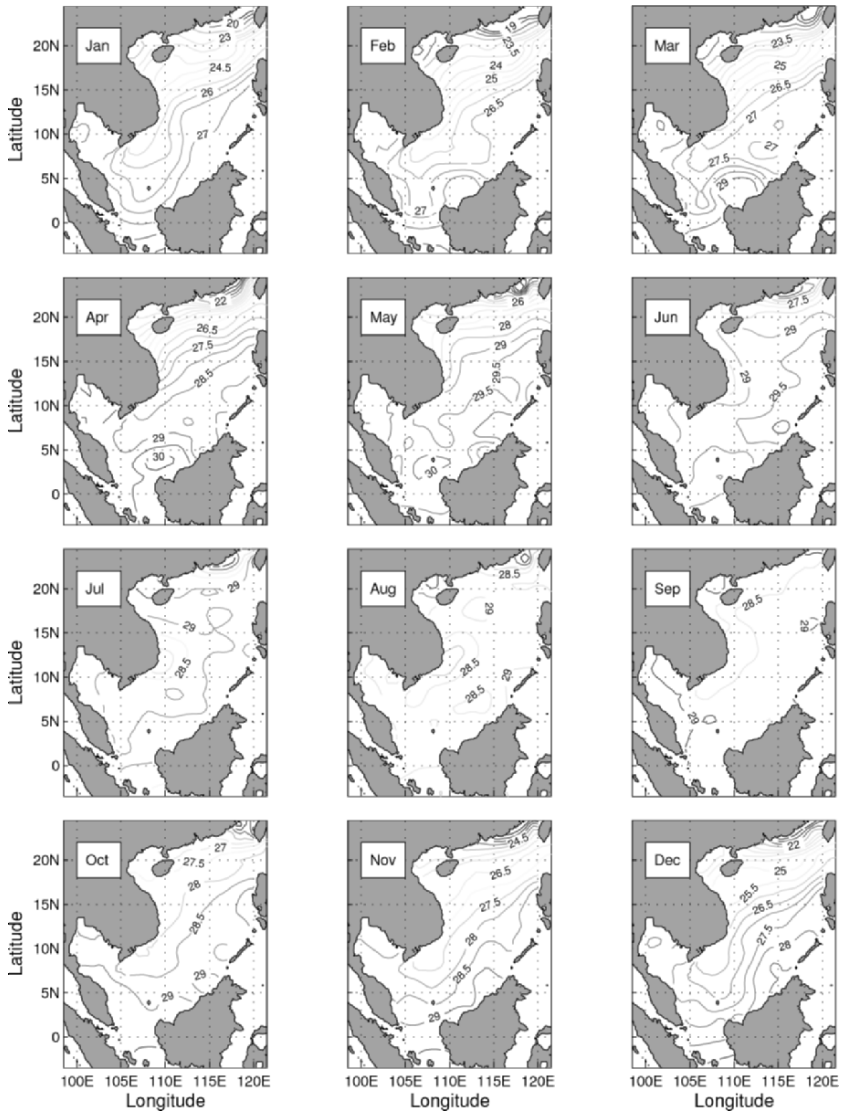

Fig. 11.39. Monthly mean sea surface temperature (°C) field with 0.5°C contour interval (from Chu and Wang 2003, Journal of Oceanography)

Figure 11.41 shows the monthly mean surface salinity with contour interval of 0.25 ppt. The isoline of 33.75 ppt (or 33.5 ppt) in February to April (or May to January) divides the South China Sea into saltier northwestern Sea and fresher southeastern Sea. The horizontal salinity gradient across thermohaline front in winter is comparable to that in summer (nearly 0.25 ppt/100 km).

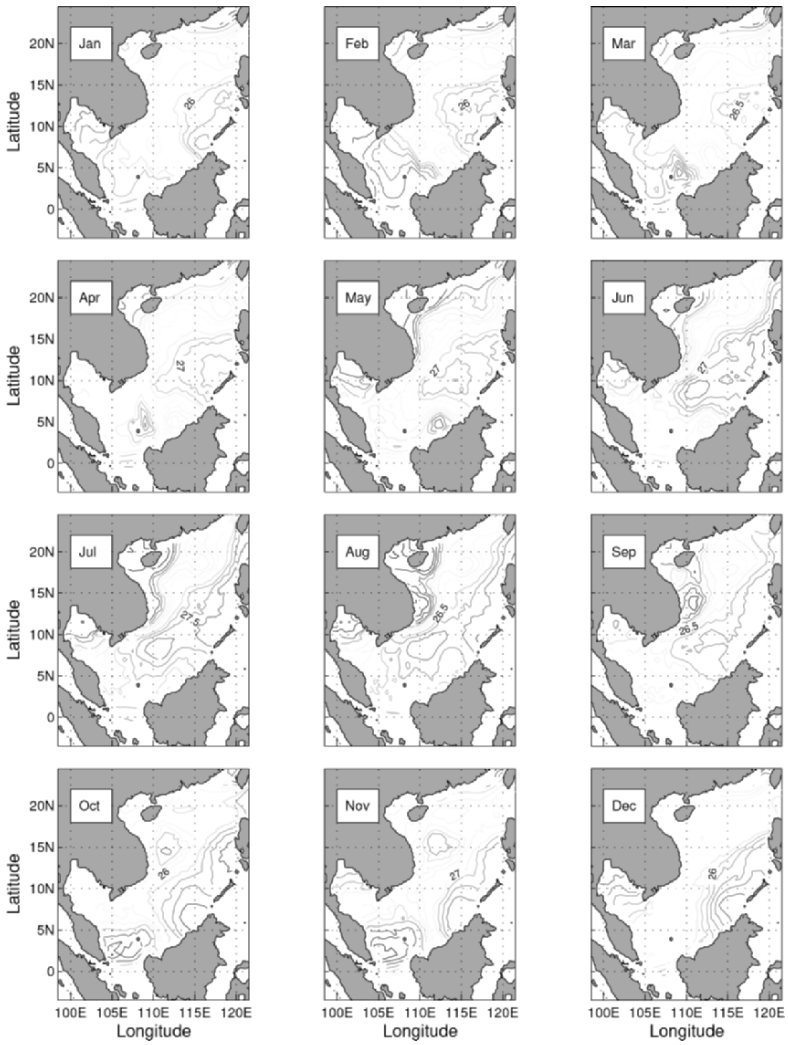

Fig. 11.40. Monthly mean temperature (°C) field at 50 m depth with 0.5°C contour interval (from Chu and Wang 2003, Journal of Oceanography)

Figure 11.42 shows the monthly mean salinity at 50 m depth. The 34.0 ppt isoline separates the saltier, northwestern South China Sea from the fresher, southeastern Sea. A strong horizontal salinity gradient (0.1 ppt/100 km) is found near the Vietnam Bight in the summer monsoon season (July to October). The thermohaline front appears strong all the year round at the surface and subsurface (50 m).

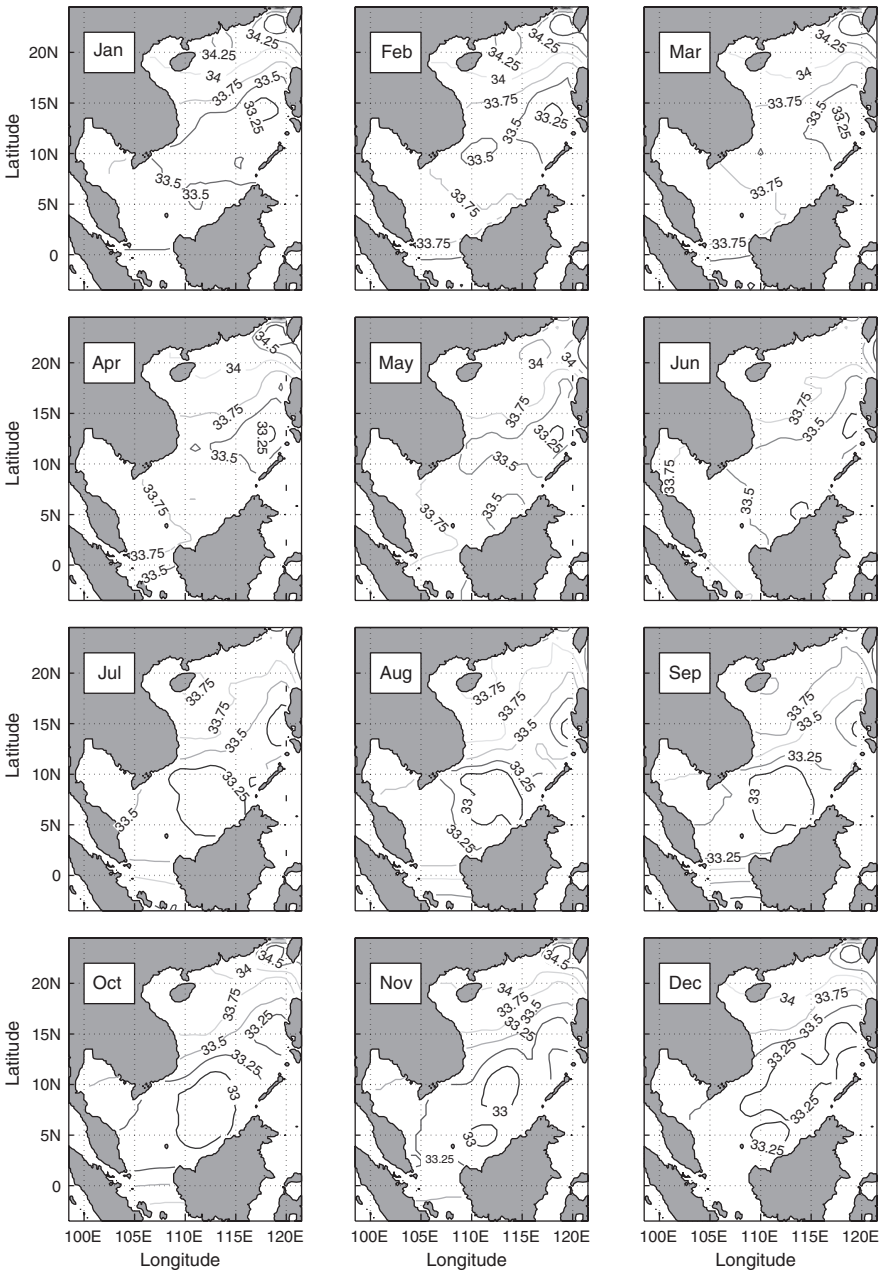

Fig. 11.41. Monthly mean sea surface salinity (ppt) field with 0.025 ppt contour interval (from Chu and Wang 2003, Journal of Oceanography)

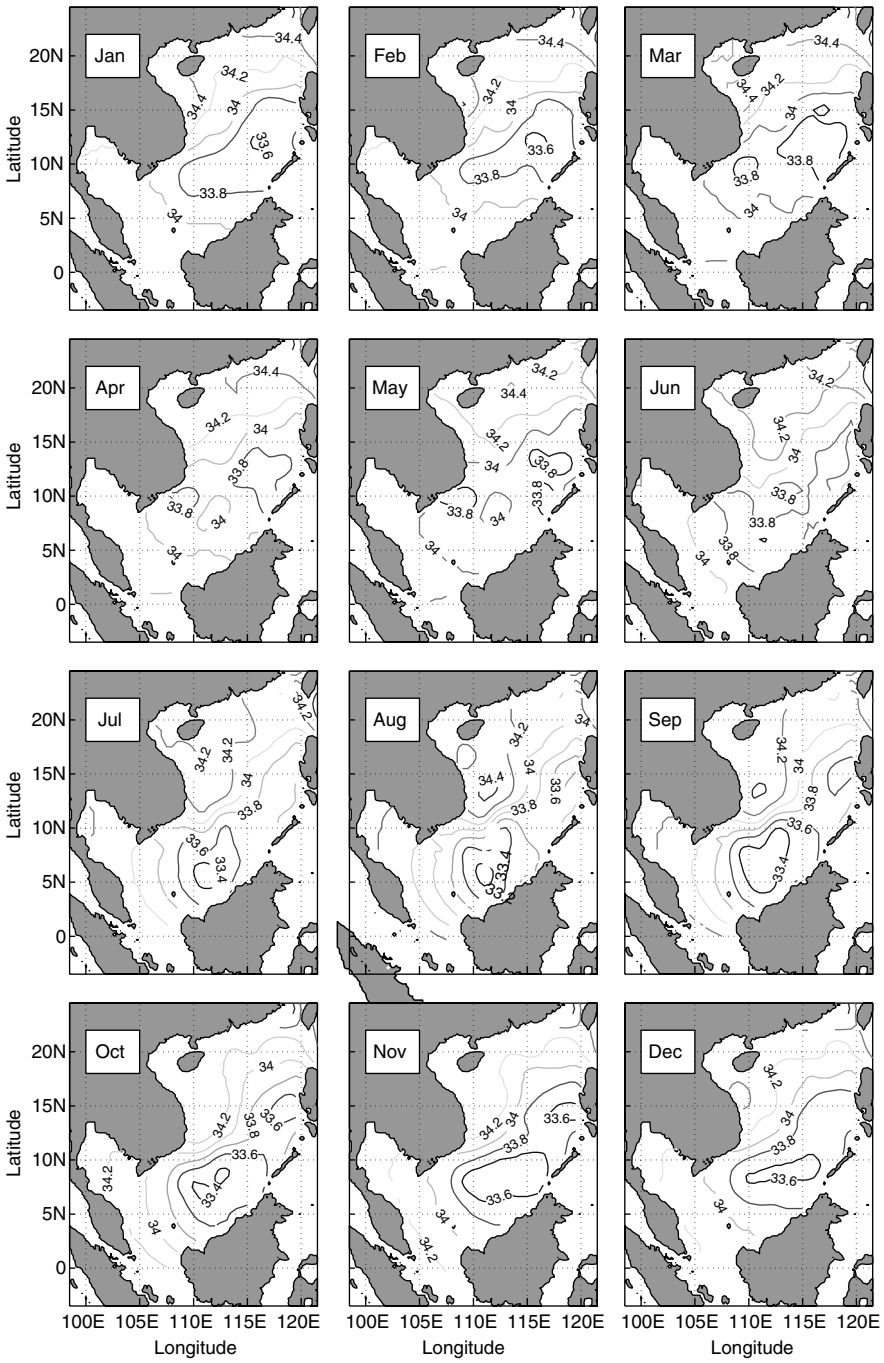

Fig. 11.42. Monthly mean salinity (ppt) field at 50 m depth with 0.02 ppt contour interval (from Chu 2003, Journal of Oceanography)

11.8.2 Forcing Mechanism

Preconditioning

The South China Sea is occupied by two separate water masses. In the north, the waters are cold and saline. The annual variability of salinity is small, due to the inflow and diffusion of high salinity water from the Pacific Ocean through the Luzon Strait. However, in the south the tropical conditions cause the waters to be warmer and fresher (Wyrtki 1961a). High temperature and low salinity water in the south, and low temperature and high salinity water in the north is the precondition for the thermohaline front formation in the central South China Sea.

Sverdrup Transport

For the ensemble mean (Fig. 11.43a and winter (Fig. 11.43b) wind stress curl (ζ) fields, the northeast-to-southwest oriented zero-curl line separates the South China Sea into anticyclonic curls (causing southward Sverdrup transport) northwest of it and cyclonic curls (causing northward Sverdrup transport) southeast of it.

This process forces the two water masses to converge at the zero-curl line, causing the formation and/or strengthening of the thermohaline front. For the summer (Fig. 11.43b) ζ field, the zero-curl line separates the South China Sea into cyclonic curls (causing northward Sverdrup transport) northwest of it and anticyclonic curls (causing southward Sverdrup transport) southeast of it. This process forces the two water masses to divergence at the zero-curl line, weakening the thermohaline front. Use of the Sverdrup theory also predicts the existence of a jet-like flow associated with the zero-curl line.

11.8.3 Cross-Basin Current

Flow Pattern

Wyrtki (1961a) published an overview of South China Sea seasonal surface circulations and postulated a cross-basin current flowing northeastward all the year round. A wind-driven circulation is formed with the beginning of the southwest monsoon in May and June. Off the coast of Vietnam a northward flowing western boundary current is clearly visible. The wide, uniform drift in the northern South China Sea shows a deflection of the current to the right of the wind and forms the cross-basin current from the Vietnam bight to Luzon island. In September the strength of the currents decreases and in October the northeast monsoon starts blowing with considerable strength. Under the influence of the winds, water masses of the North Equatorial Current are intruded through Luzon Strait into South China Sea. This water flows along the coast of China to the southwest with a remarkable westward intensification

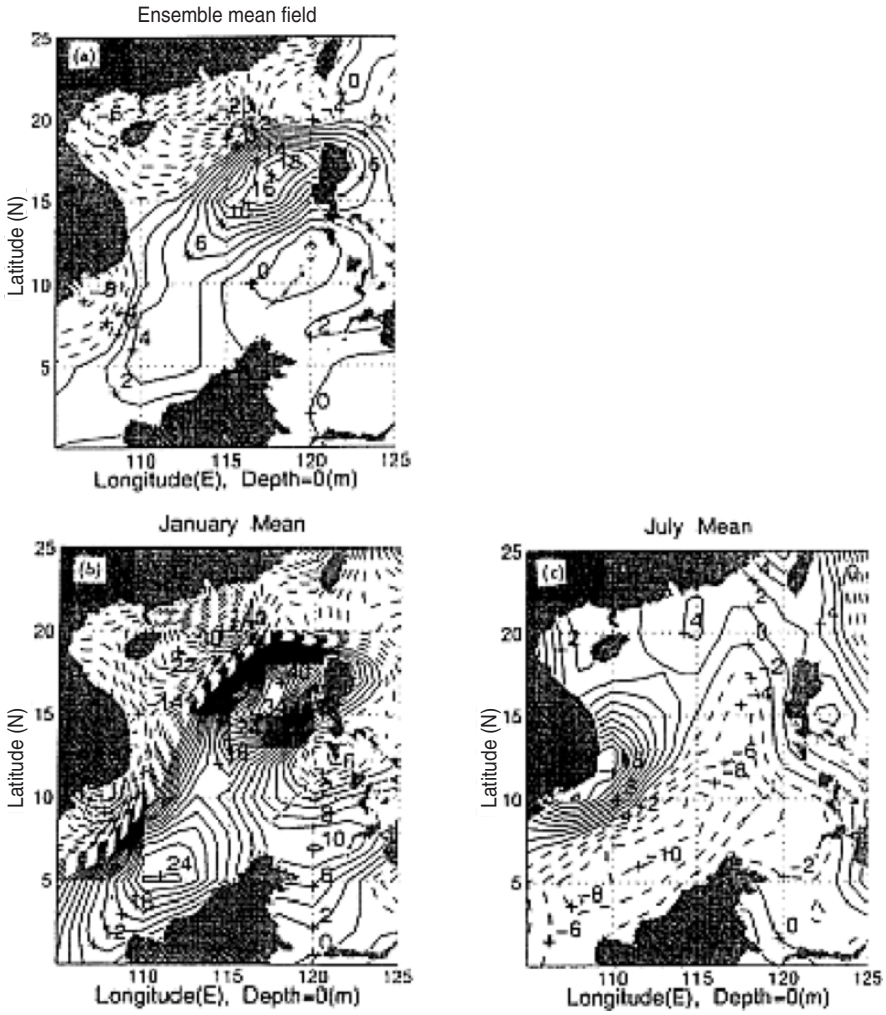

Fig. 11.43. Surface wind stress curl: (**a**) ensemble mean, (**b**) January, and (**c**) July. The unit is 10^{-8} N m^{-3} (from Chu et al. 1997d, Journal of Geophysical Research)

of the current. In the central South China Sea a counter current (i.e., cross-basin current) is developed north of 10°N.

The calculated absolute velocity field (Figs. 11.44 and 11.45) using the z-level P-vector method clearly shows the existence of the cross-basin current flowing northeastward from the Vietnam bight to Luzon island. Different from Wyrtki's cartoons, the coastal currents are not well obtained using the P-vector method. A comparison of Figs. 11.44, 11.45 with Figs. 11.39–11.42 shows the colocation of the crosscoastal current and the thermohaline front.

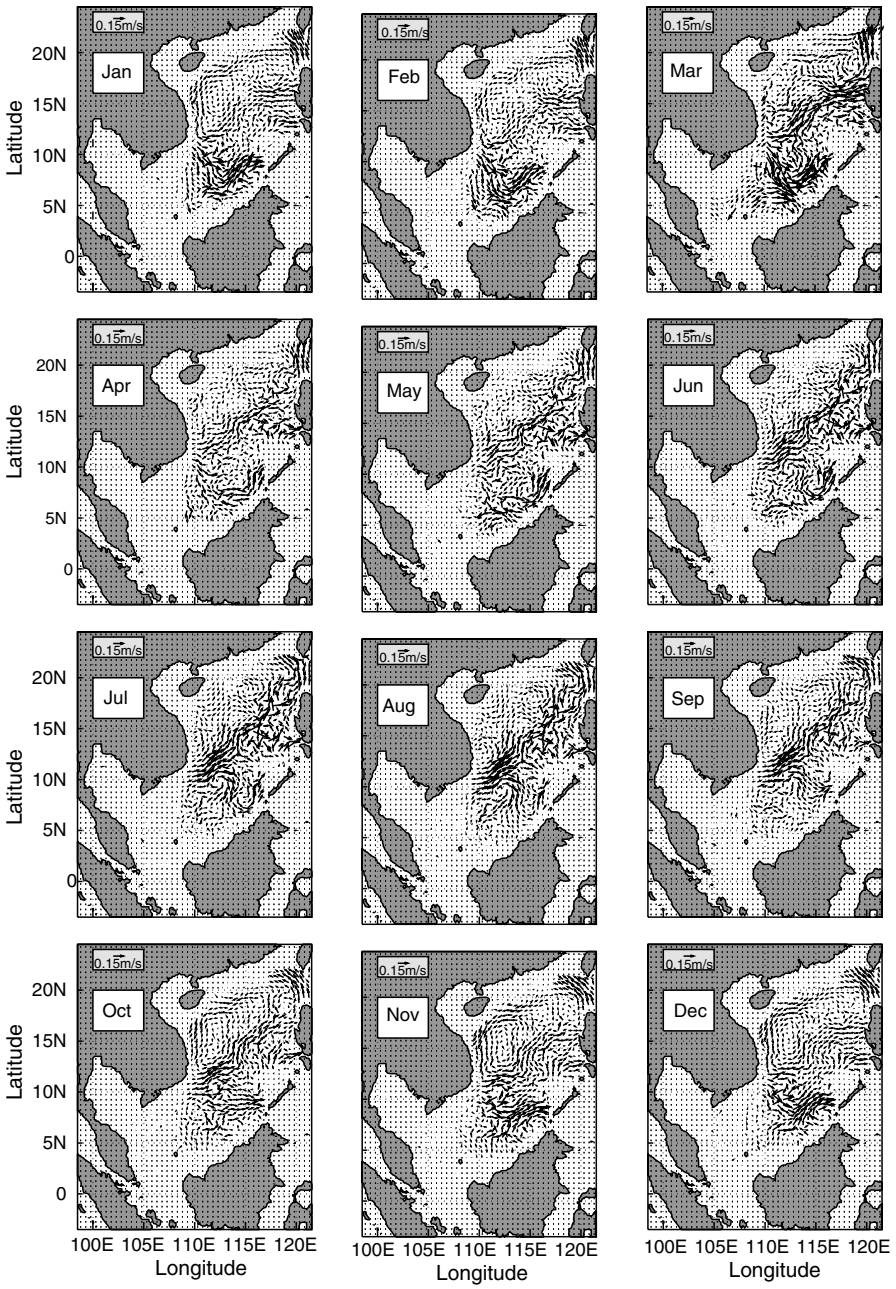

Fig. 11.44. Inverted monthly mean velocity field at the surface using the P-vector method (from Chu and Wang 2003, Journal of Oceanography)

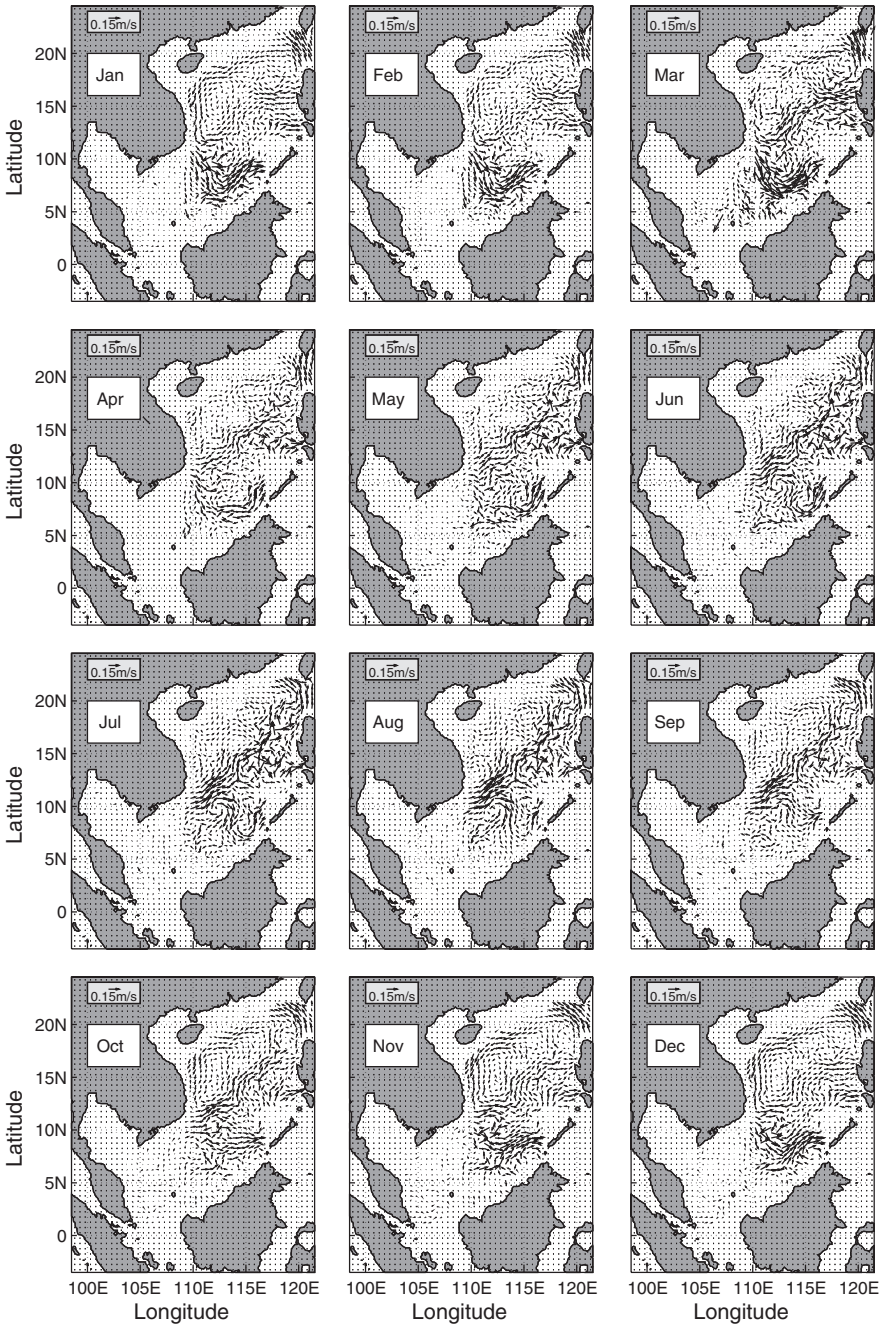

Fig. 11.45. Inverted monthly mean velocity field at 50 m depth using the P-vector method (from Chu and Wang 2003, Journal of Oceanography)

The cross-basin current has a weak seasonal variation in flow direction and a strong seasonal variation in current speed. It strengthens in summer and weakens in winter. In July and August, the maximum speed of the cross-basin current reaches $0.25\,\mathrm{m\ s^{-1}}$($0.2\,\mathrm{m\ s^{-1}}$) in the southern part near the Vietnam bight at the surface (50 m depth). In January and February the cross-basin current is very weak, around $0.05\,\mathrm{m\ s^{-1}}$ at the surface and 50 m deep. The seasonal variation of the cross-basin current is well reproduced by numerical modeling (e.g., Shaw and Chao 1994).

The cross-basin current meanders and generates cyclonic (anticyclonic) eddies to the northwest (southeast). For example, it meanders at (110°E, 10°N) from June to August. An anticyclonic eddy has been identified with its center at (112°E, 9°N) and a size of around 300 km. The tangential velocity of this eddy is nearly $0.2\,\mathrm{m\ s^{-1}}$. This multieddy structure will be discussed in the next section.

Axis of the Cross-Basin Current

The orientation of the maximum velocity along the cross-basin current is defined as the axis that extends from (110°E, 10°N) to (120°E, 18°N) in a straight line at 50 m depth (as an example) from April to September (Fig. 11.46).

In October, the axis maintains as a straight-line course and shifts southward with a larger displacement in the northern part (250 km in the north tip) than in the southern part (100 km in the south tip). From November to March, the axis of the cross-basin current is no longer a straight line. The western part of the axis (west of 115°E) jumps around 200 km northward compared to October. The eastern part (east of 115°E) of the axis becomes zonal along 15°N latitude.

11.8.4 Water Mass Characteristics across the Front

Subareas

As described in Sect. 11.8.3, the water masses have different characteristics north and south of the thermohaline front, with high temperature low salinity water in the south, and low temperature high salinity water in the north. Analysis of T, S data in the latitudinal strip (112.5–115°E) is necessary to quantify the thermohaline variability across the thermohaline front and for a further understanding of the driving and variation mechanism of the thermohaline front.

This strip is divided from 6 to 22°N into eight rectangles with 2.5° in the zonal direction and 2° in the latitudinal direction (Fig. 11.47). These boxes can be grouped into three subareas: the thermohaline front (4 and 5), south of the thermohaline front (1–3), and north of the thermohaline front (6–8). The change of T–S features among these boxes leads to an understanding of the structure and the forcing mechanism of the thermohaline front.

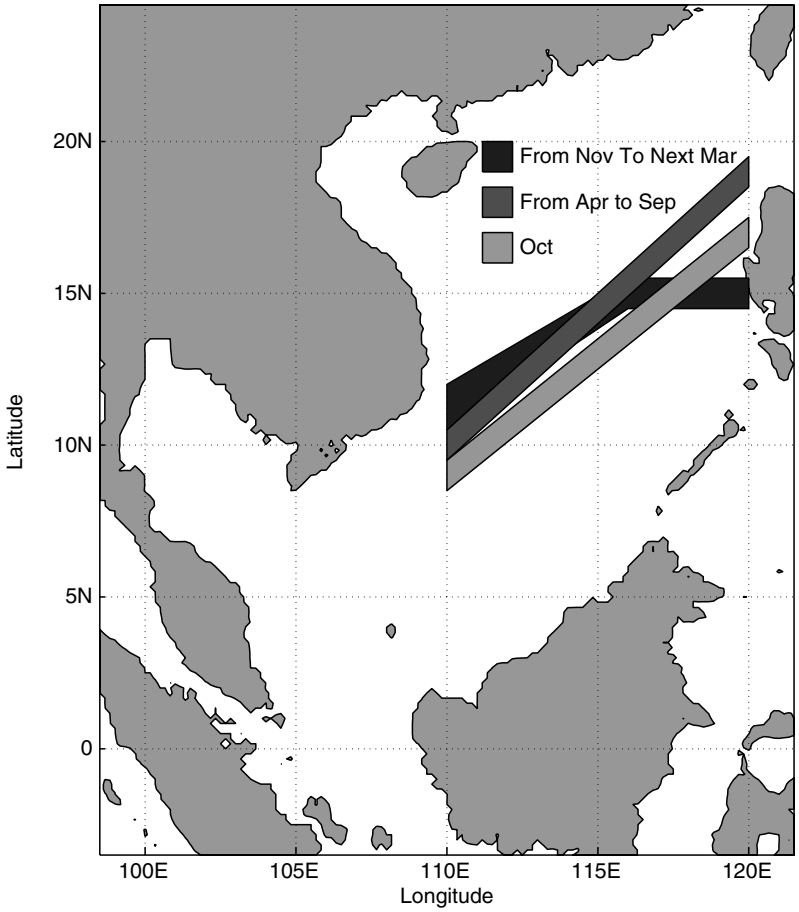

Fig. 11.46. Seasonal variation of the axis of the cross-basin current at 50 m depth (from Chu and Wang 2003, Journal of Oceanography)

T–*S* Diagrams

The upper layer (0–300 m deep) T–S diagrams are plotted for each box in January (Fig. 11.48) and July (Fig. 11.49), respectively. The T–S curves in all boxes are of the same type (reverse-C shape) with a salinity maximum (nearly 34.65 ppt north of the thermohaline front and around 34.52 ppt south of the thermohaline front) layer. The maximum salinity has been previously discussed by Qu (2000) using T, S profiles from NODC. The location and the strength of the maximum salinity are comparable whether they are studied using the GDEM (Chu and Wang 2003) or NODC data (Qu 2000).

The T–S curves, however, have a larger range in both T and S south of the thermohaline front (Boxes 1–3) than to the north (Boxes 6–8), and the salinity maximum occurs at a shallower depth, north of the thermohaline front

Fig. 11.47. Division of subareas across the thermohaline front (from Chu and Wang 2003, Journal of Oceanography)

($\sigma_t \simeq 25\,\mathrm{kg\ m^{-3}}$ in Boxes 6–7) than to the south ($\sigma_t \simeq 25.6$–$25.8\,\mathrm{kg\ m^{-3}}$ in Boxes 1–3). Thus, the thermohaline variability is larger at the south than at the north of the thermohaline front.

T–*S* Profiles

The mean vertical T and S profiles are plotted for each box in January (Fig. 11.50) and July (Fig. 11.51), respectively. The thermohaline structure below 150 m is quite uniform horizontally and has weak seasonal variability between January and July, which indicates that the thermohaline front is an upper layer phenomenon. The halocline is stronger at the south than at the

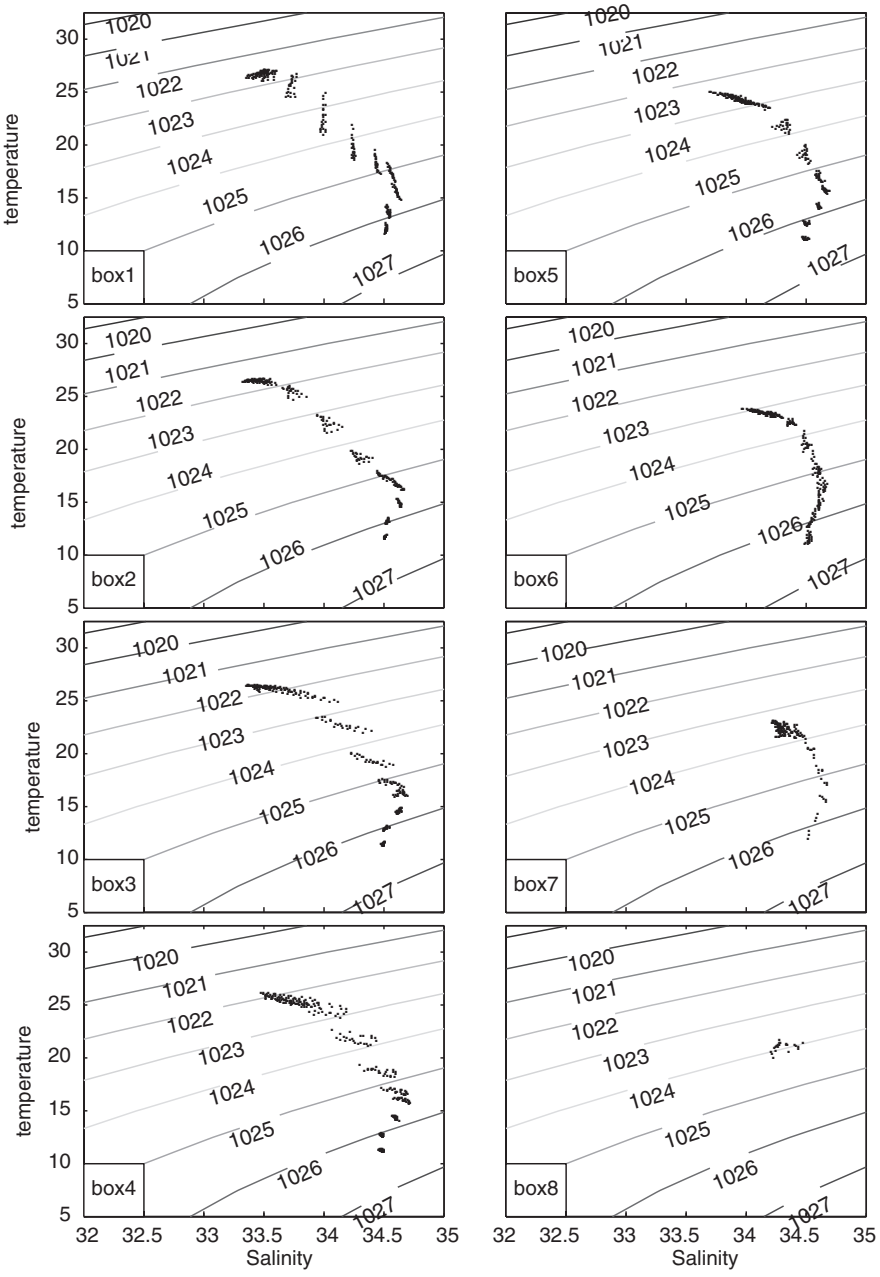

Fig. 11.48. Change of T–S diagrams across the thermohaline front in January (from Chu and Wang 2003, Journal of Oceanography)

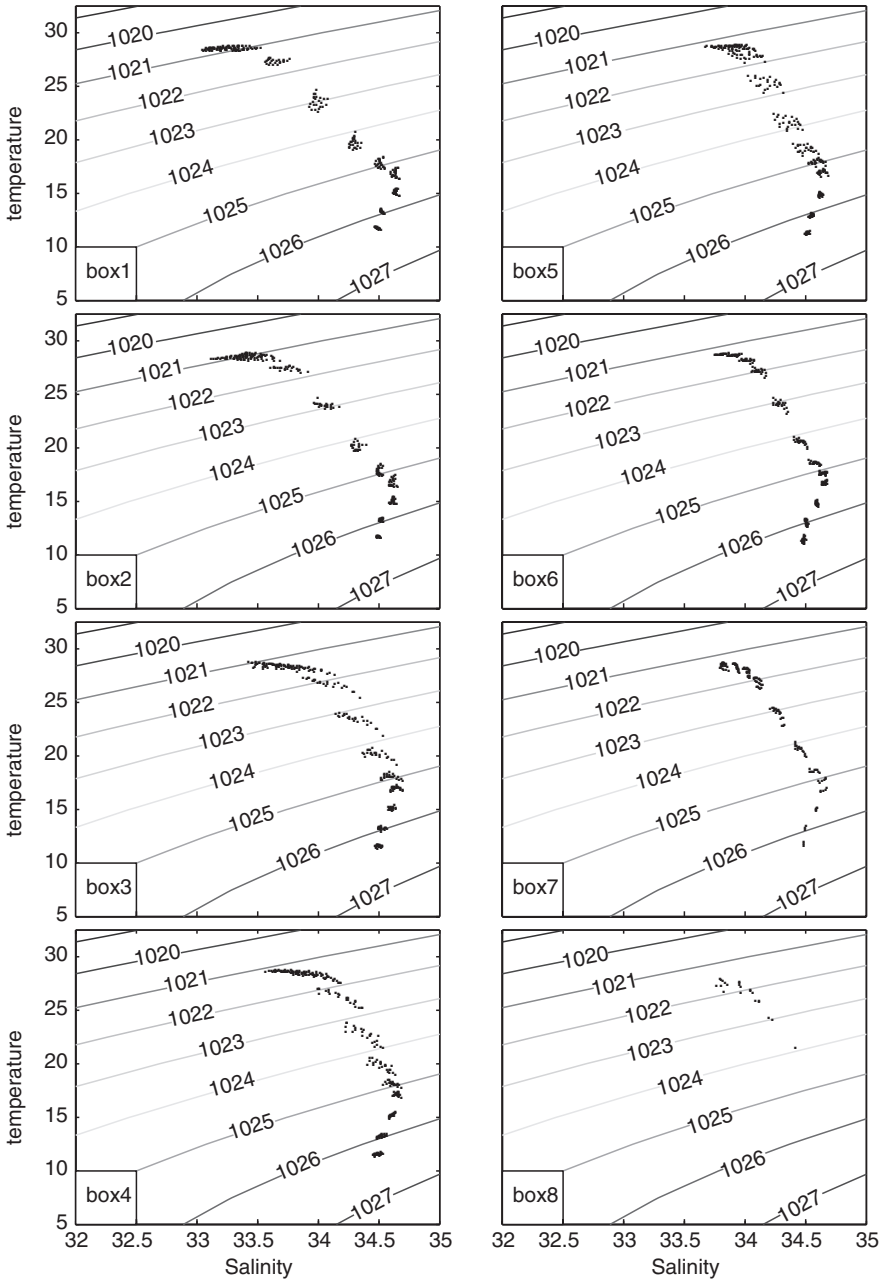

Fig. 11.49. Change of T–S diagrams across the thermohaline front in July (from Chu and Wang 2003, Journal of Oceanography)

north of the thermohaline front in both seasons (January and July). For example, the vertical salinity gradient in January is around 0.83 ppt/100 m in Box 2 (south of the thermohaline front) and nearly 0.38 ppt/100 m in Box 6 (north of the thermohaline front), and the vertical salinity gradient in July is around 0.92 ppt/100 m in Box 2 (south of the thermohaline front) and nearly 0.56 ppt/100 m in Box 6 (north of the thermohaline front). The salinity maximum ($\sim$ 34.65 ppt) occurs at shallower depth north of the thermohaline front (around 150 m deep in Boxes 6–7) than south of the thermohaline front (around 200 m deep in Boxes 1–3). There is no noticeable seasonal variability.

Seasonal thermohaline variability is evident above 150 m depth, and is stronger north than south of the thermohaline front. For example, January temperature profiles (Fig. 11.50) show deeper mixed layers north of the thermohaline front (e.g., around 60 m in Box 6) than south of the thermohaline front (e.g., 35 m in Box 2). This is caused by the dipole of the surface wind stress curl with anticyclonic (cyclonic) curl north (south) of the thermohaline front. July temperature profiles (Fig. 11.51) show shallower mixed layers north of the thermohaline front (e.g., around 10 m in Box 6) than south of the thermohaline front (e.g., 30 m in Box 2) with the same mechanism as January.

Surface Temperature

Monthly mean SST data show a larger seasonal variability north (Box-6) than south (Box-2) of the thermohaline front (Fig. 10.52a, b). The coldest SST occurs in February in both boxes: 23.5°C in Box-6 (north of the thermohaline front), and 26.6°C in Box-2 (south of the thermohaline front). The warmest SST north (south) of the thermohaline front is 29.1°C(29.6°C) appearing in July (May). The seasonal variability (warmest minus coldest temperature) is around 5.6°C in Box-6 and 3°C in Box-2.

The SST difference $\Delta\mathrm{SST} = \mathrm{SST}_{\mathrm{Box}-2} - \mathrm{SST}_{\mathrm{Box}-6}$ is used to represent the strength of the surface thermohaline front in temperature (Fig. 11.52c). The difference (ΔSST) reaches a maximum value (3.1°C, strongest surface thermohaline front) in January, and a minimum value of 0.2°C in July and August (no surface thermohaline front).

Subsurface Temperature (50 m)

Monthly mean temperature at 50 m depth shows a larger seasonal variability at the north (Box-6) than at the south (Box-2) of the thermohaline front (Fig. 11.53a, b). The coldest temperature occurs in February in both boxes: 23.3°C in Box-6 (north of the thermohaline front), and 25.5°C in Box-2 (south of thermohaline front). The warmest temperature north (south) of the thermohaline front is 26.8°C(27.8°C) appearing in October (June). The seasonal variability is around 3.5°C in Box-6 and 2.3°C in Box-2.

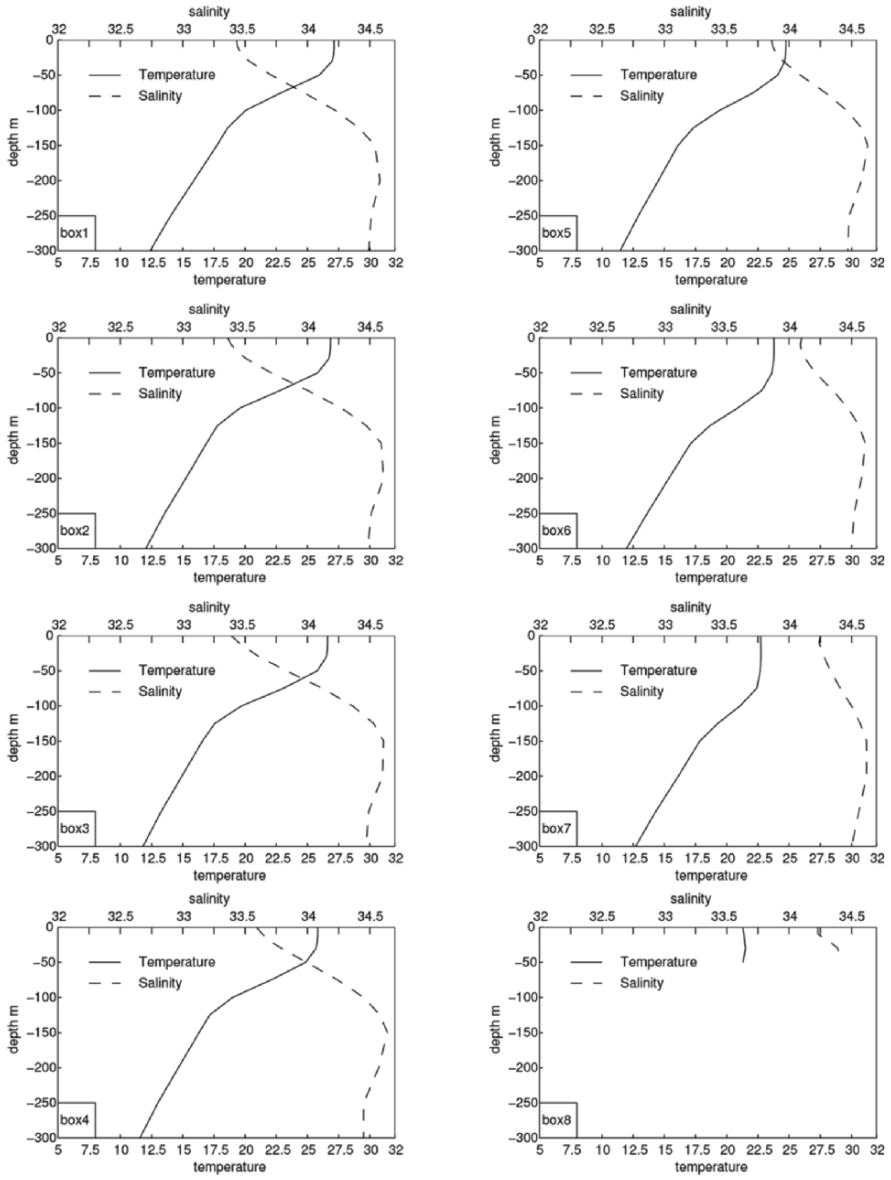

Fig. 11.50. Change of T and S profiles across the thermohaline front in January (from Chu and Wang 2003, Journal of Oceanography)

The temperature difference,

$$\Delta T = T_{\mathrm{Box}-2} - T_{\mathrm{Box}-6}$$

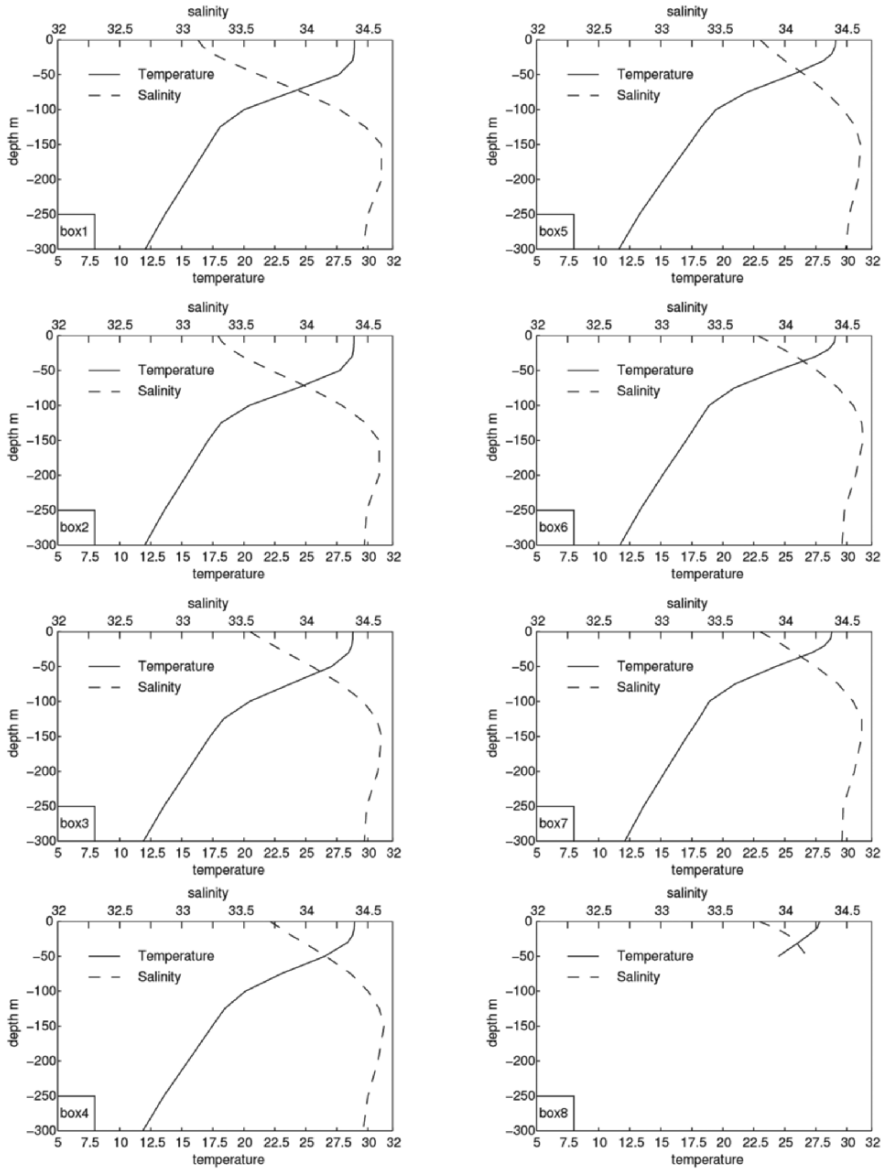

Fig. 11.51. Change of T and S profiles across the thermohaline front in July (from Chu and Wang 2003, Journal of Oceanography)

is used to represent the strength of the thermohaline front (Fig. 11.53c) at 50 m depth. The difference (ΔT) is larger in summer than in winter, and reaches 3.6°C (strongest subsurface thermohaline front) in June, and 0.9°C in October (weak subsurface thermohaline front).

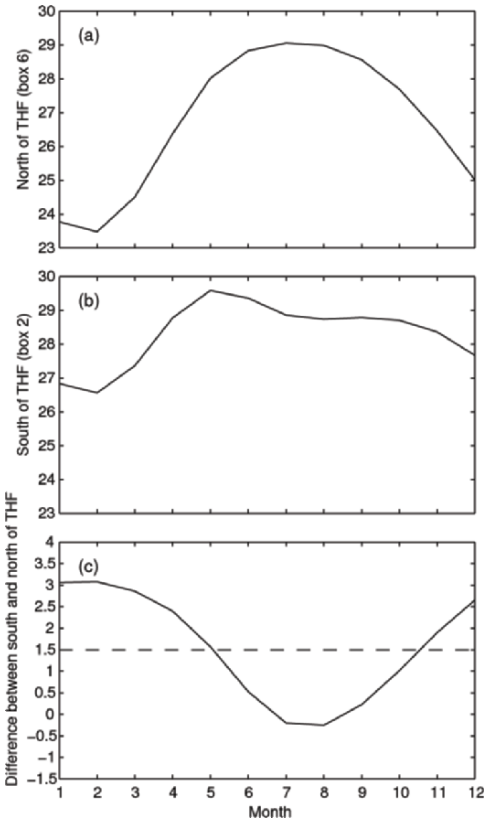

Fig. 11.52. Monthly evolutions of (**a**) SST (°C) north of the thermohaline front (Box-6), (**b**) SST (°C) south of the thermohaline front (Box-2), and (**c**) the difference between the two ($\Delta\ SST$). A criterion of $\Delta\ SST = 1.5$°C (denoted by the *dashed line*) is used to represent the occurrence of the thermohaline front. Below the *dashed line*, ΔSST ≤ 1.5°C, the temperature difference is not evident across the thermohaline front (from Chu and Wang 2003, Journal of Oceanography)

Surface Salinity

Monthly mean surface salinity shows different seasonal variability north (Box-6) and south (Box-2) of the thermohaline front (Fig. 11.54a, b). Low salinity is 33.78 ppt (32.96 ppt) north (south) of thermohaline front appearing in July and August (October and November). High salinity is 34.14 ppt (33.57 ppt) north (south) of the thermohaline front appearing in February (March). The seasonal variability is around 0.61 ppt (0.36 ppt) north (south) of the thermohaline front.

The difference,

$$\Delta S = S_{\mathrm{Box-2}} - S_{\mathrm{Box-6}},$$

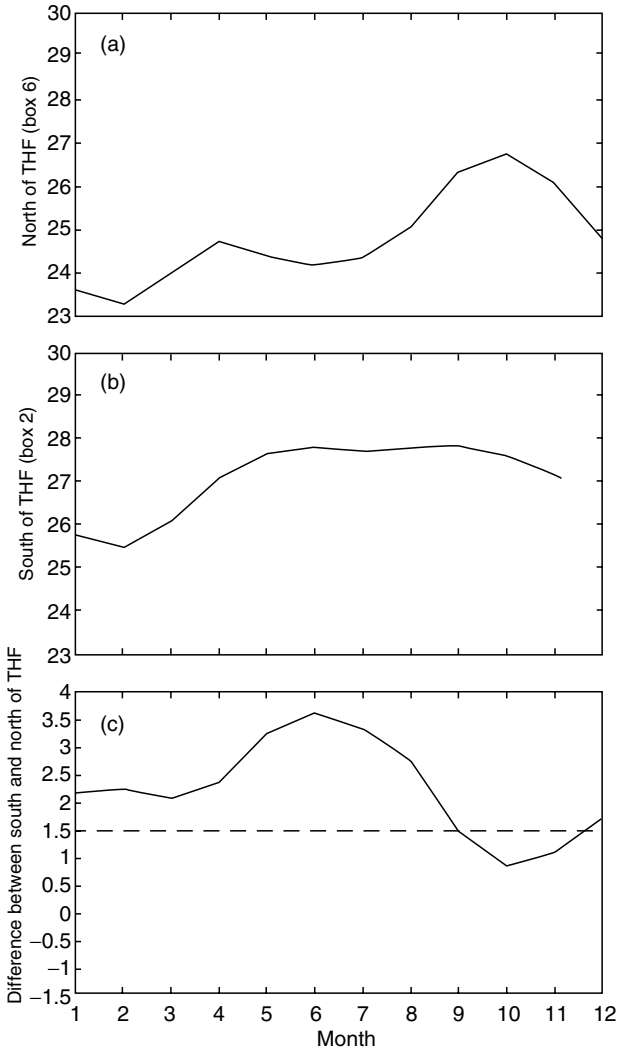

Fig. 11.53. Monthly evolutions at 50 m depth of (**a**) temperature (°C) north of the thermohaline front (Box-6), (**b**) temperature (°C) south of the thermohaline front (Box-2), and (**c**) the difference between the two (ΔT). A criterion of $\Delta T = 1.5$°C (denoted by the *dashed* line) is used to represent the occurrence of the thermohaline front. Below the dashed line ($\Delta T < 1.5$°C), the temperature difference evident across the thermohaline front (from Chu and Wang 2003, Journal of Oceanography)

is used to represent the strength of the surface thermohaline front in salinity (Fig. 11.54c). The values of ΔS are all negative, indicating that the surface water is more saline to the north than south of the thermohaline front. The difference (ΔS) reaches a maximum value (0.96 ppt, strongest surface

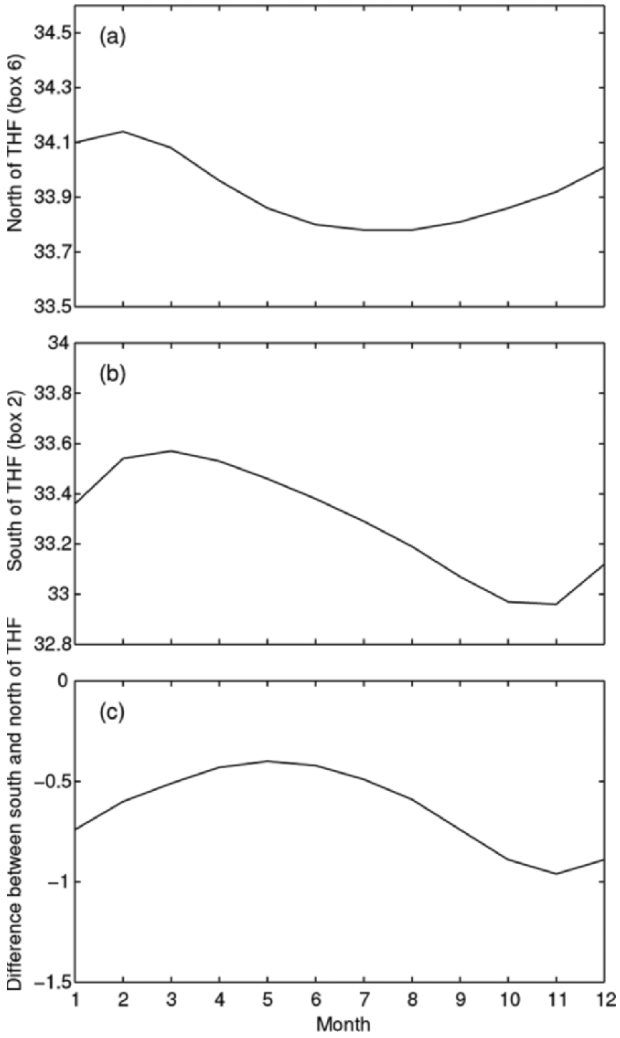

Fig. 11.54. Monthly evolutions at the surface of (**a**) salinity (ppt) north of the thermohaline front (Box-6), (**b**) salinity (ppt) south of the thermohaline front (Box-2), and (**c**) the difference between the two (ΔS) (from Chu and Wang 2003, Journal of Oceanography)

thermohaline front in salinity) in November, and a minimum value of 0.4 ppt in May (weak surface thermohaline front in salinity). The seasonal variation of ΔS is mainly caused by the salinity decrease in the southern South China Sea (Fig. 11.54b). This confirms that the major mechanism for the formation of the thermohaline front is the local expansion-blocking mechanism described in Sect. 11.8.3.

Subsurface (50 m) Salinity

Monthly mean salinity values at 50 m depth show a nearly in-phase seasonal variability north (Box-6) and south (Box-2) of thermohaline front (Fig. 11.55a, b). The minimum salinity north (south) of thermohaline front is 34.14 ppt (33.64 ppt) appearing in November (August and September). The maximum salinity occurs in May: 34.36 ppt north of thermohaline front, and 33.87 ppt south of thermohaline front. The seasonal variability is around 0.22 ppt in Box-6 and 0.23 ppt in Box-2, representing comparable seasonal variability north and south of the thermohaline front.

The salinity difference between Box-2 and Box-6 (Fig. 11.55c) represents the strength of the subsurface thermohaline front in salinity. The values of ΔS are all negative, indicating that the subsurface water is more saline at the north than at the south of the thermohaline front. The difference ΔS is nearly 0.5 ppt all the year round.

11.9 MultiEddy Structure Detected from AXBT Data

Climatological data (i.e., GDEM) show the existence and seasonal variability of the thermohaline front and associated cross-basin current in the central South China Sea. Lateral temperature and salinity gradients across the front may cause baroclinic instability which makes the cross-basin current to meander. Mesoscale eddies may be generated by the baroclinic instability. Wang et al. (2003) identified the multieddy structure using the satellite altimetry data. This section will discuss the multieddy structure in the South China Sea.

11.9.1 General Description

Seasonal occurrence of the South China Sea eddies have been reported by several authors. Dale (1956) and Uda and Nakao (1972) reported a cold eddy off the central Vietnam coast in summer. Nitani (1970) found a cold eddy located northwest of Luzon in summer. Reports from the South China Sea Institute of Oceanology (1985) indicate that a warm-core eddy appears in summer and winter in the central South China Sea, but in summer, it is closer to Vietnam at the surface. Recently, a cold-core eddy was detected in the central South China Sea during December 29, 1993, to January 5, 1994, from the analysis of TOPEX/Poseidon data (Soong et al. 1995). Chu et al. (1997c) and Chu and Chang (1997) identified a central surface warm-core eddy in mid-May from a historical data set: the MOODS. From the composite analysis on the NCEP monthly SST fields (1982–1994), Chu et al. (1997d) found that during the spring-to-summer monsoon transition (March–May) a warm anomaly (greater than 1.8°C) is formed in the central South China Sea at 112°–119°30′E, 15°–19°30′N.

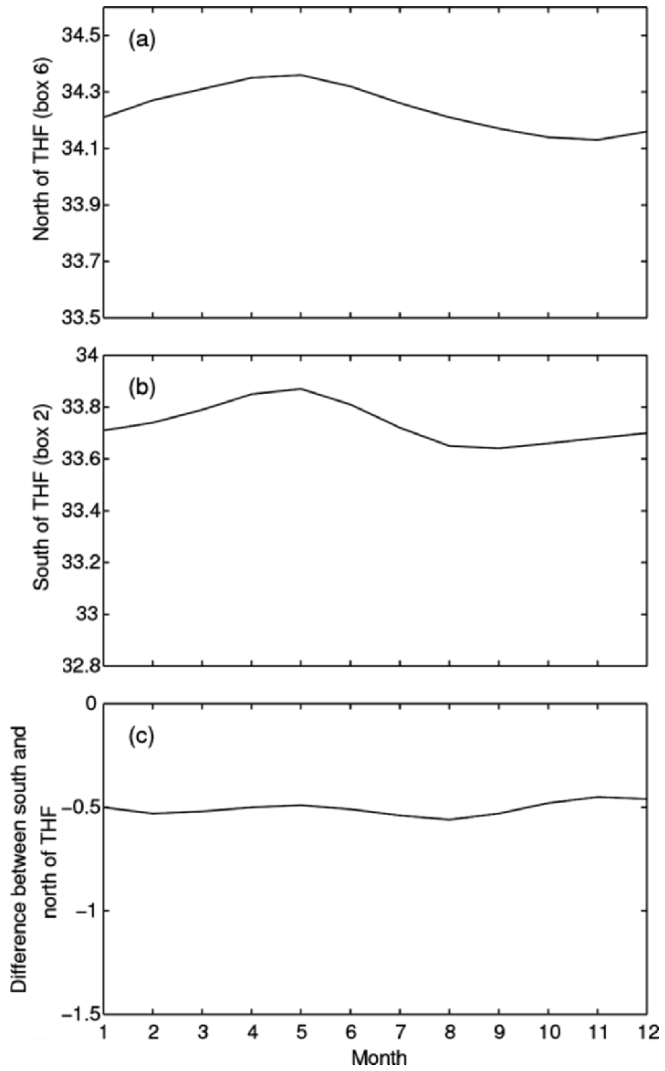

Fig. 11.55. Monthly evolutions at 50 m depth of (**a**) salinity (ppt) north of the thermohaline front (Box-6), (**b**) salinity (ppt) south of the thermohaline front (Box-2), and (**c**) the difference between the two (ΔS) (from Chu and Wang 2003, Journal of Oceanography)

The Naval Oceanographic Office conducted an intensive AXBT survey during May 14–25, 1995, over the majority of the South China Sea down to about 300 m depth. Figure 11.56 shows the daily AXBT deployment. This data set provides something close to a "snapshot" of the temperature in the upper ocean in the South China Sea during the transition time before the onset of the monsoon. Since only temperature-measuring AXBTs were used,

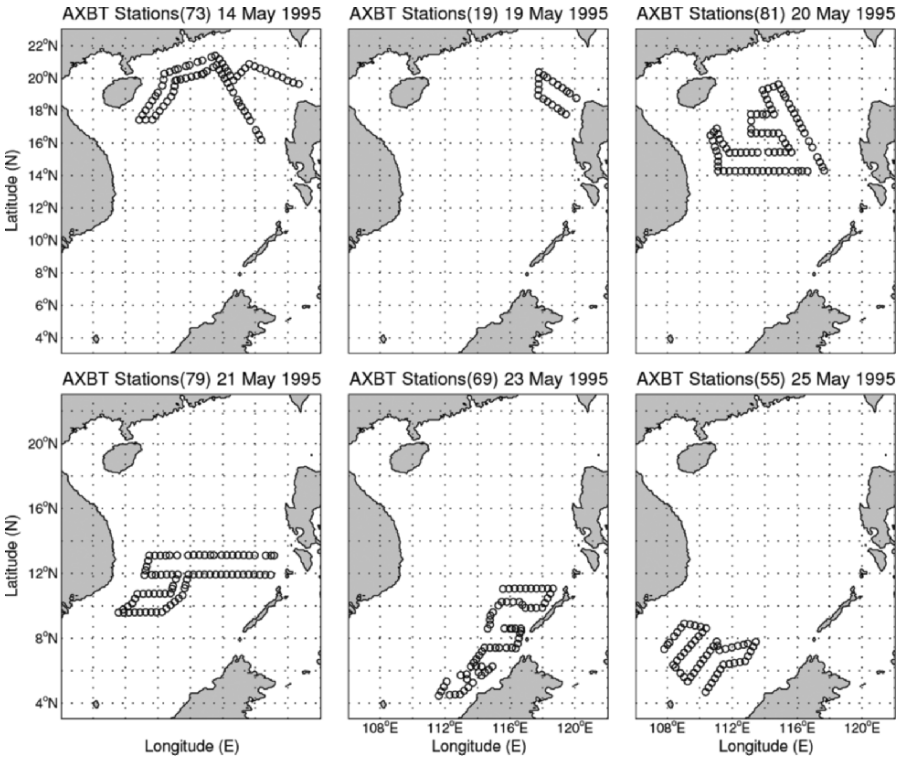

Fig. 11.56. Deployment pattern of AXBT survey during May 14–25, 1995 (from Chu et al. 1998d, Journal of Geophysical Research)

no salinity measurements were made at the same time. The three-dimensional velocity field is inverted from analysis of this temperature data set using climatological salinity data (Levitus et al. 1994) in lieu of in situ salinity data. Chu et al. (1998d) identified three dimensional multieddy structures from the AXBT data using the P-vector method.

11.9.2 AXBT Measurements

Most of the 376 AXBTs were deployed at six intervals over a 12 day period from May 14–25, 1995 (Chu et al. 1998d; Fig. 11.56). The majority of the AXBTs were nominally capable of reaching a depth of 360–400 m. The ensemble of temperature profiles (Fig. 11.57a) and the mean profile with an envelope of a standard deviation (Fig. 11.57b) show the existence of a mixed layer with depths ranging from 20 to 60 m and a thermocline with a vertical temperature gradient of 6–7°C per 100 m below the mixed layer.

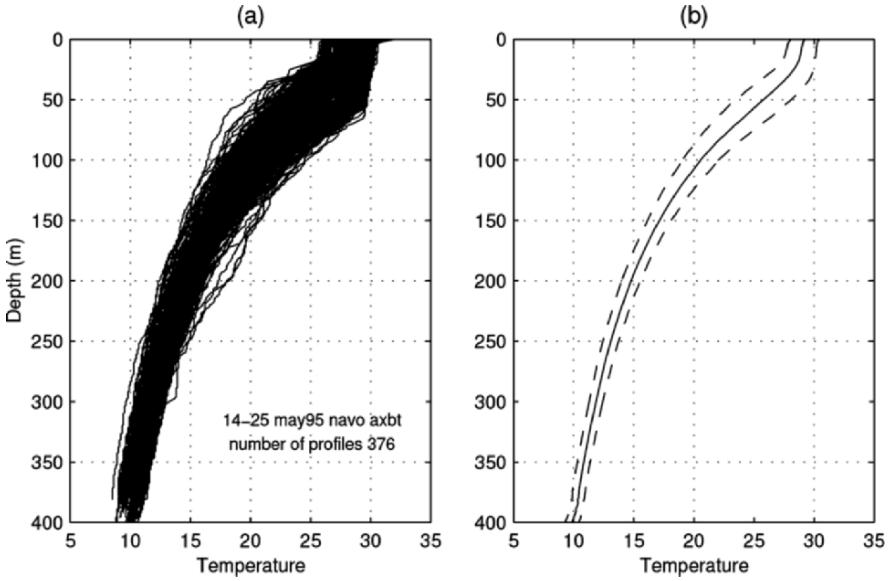

Fig. 11.57. Temperature profiles of AXBT survey during May 14–25, 1995. (**a**) Ensemble of profiles and (**b**) the mean profile with an envelope of a standard deviation. Both show the existence of a mixed layer with depths ranging from 20 to 60 m and a thermocline with a vertical temperature gradient of 6–7°C/100 m below the mixed layer (from Chu et al. 1998d, Journal of Geophysical Research)

The AXBT observations were mapped to a regular grid at 12 levels (Table 11.1) using a two-scale OI scheme (Gandin 1965; Lozano et al. 1996). The large-scale OI was used to estimate the background mean with a decorrelation scale of 450 km. The mesoscale OI was used to map the observational anomaly from the background mean field into a regular grid with a spatial decorrelation scale of 75 km and a temporal decorrelation scale of 10 days. The spatial and temporal decorrelation scales associated to the mean field was estimated from the covariance matrix obtained from the MOODS for the South China Sea (Chu et al. 1997c). The large-scale mean was computed using the temperature and salinity profiles. The large-scale pattern for the surface (not shown) resembles the pattern previously estimated by Chu et al. (1997c). The decorrelation length scale for the fluctuations from the mean was estimated from the AXBT data. The results shown below are relatively insensitive to the length scale in the range of 60–90 km. The decorrelation timescale was selected to ensure synopticity. The SST horizontal scales seem rather larger than temperatures in the seasonal thermocline. Here, we choose horizontal scales to be uniform in the vertical for convenience and for lack of sufficient data to discriminate these differences properly.

11.9.3 Temperature

Horizontal Structures

Figure 11.58a–e shows horizontal depictions of temperature at 0, 50, 100, 200, and 300 m depths, respectively. The contour interval is 0.5°C. In them, we see that warmer water is situated at the central South China Sea with surrounding cooler water.

At 50 m depth, 28°C isotherm separates the warm central South China Sea water from the surrounding cooler water. The maximum temperature reaches 29°C. This central South China Sea warm pool extended to the 300 m depth and was surrounded by Dongsha, Hainan, South-Vietnamese Bight, and Liyue cool pools and also Xisha warm pool. The location and thermal features of these warm and cool pools are listed in Table 11.2.

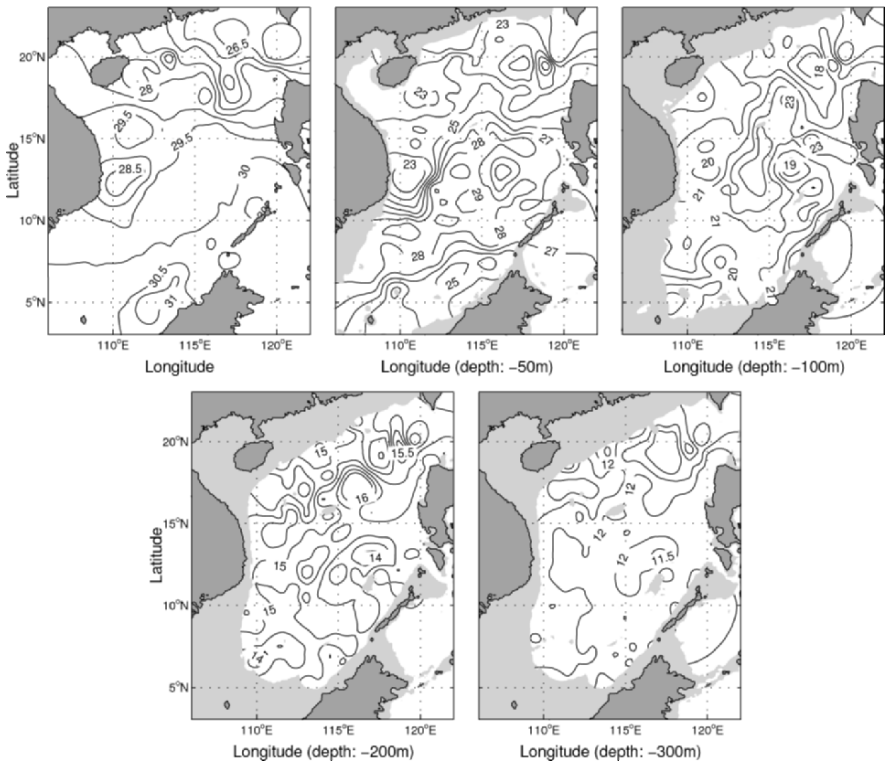

Fig. 11.58. Horizontal temperature fields at different depths: (**a**) 0 m, (**b**) 50 m, (c) 100 m, (**d**) 200 m, and (**e**) 300 m. The central South China Sea warm pool was surrounded by Dongsha, Hainan, South-Vietnamese Bight, and Liyue cool pools and Xisha warm pool (from Chu et al. 1998d, Journal of Geophysical Research)

Table 11.2. Locations, typical temperatures, and tangential velocities of the South China Sea warm-core and cool-core eddies detected during May 14–25, 1995 (from Chu et al. 1998d, Journal of Geophysical Research)

depth (m)	central (W)	Xisha (W)	Dongsha (C)	Hainan (C)	South Vietnamese Bight (C)	Liyue (C)
0	112–117°E	110–112°E	116–118°20′E	110–112°E	108–112°E	115–118°E
	12–18°N	14–16°N	18–20°20′N	18–20°N	10–14°N	12–14°N
	29.5–30°C	29.5°C	27°C	28°C	28.5°C	29.5–30°C
	0.4 m s^{-1}	0.2 m s^{-1}	0.4 m s^{-1}	0.1 m s^{-1}	0.2 m s^{-1}	0.3 m s^{-1}
30	112–117°E	110–112°E	116–118°20′E	110–112°E	108–112°E	115–118°E
	12–18°N	14–16°N	8–20°20′N	16–18°N	10–14°N	12–14°N
	29°C	24°C	22°C	23°C	23°C	26°C
	0.3 m s^{-1}	0.1 m s^{-1}	0.25 m s^{-1}	0.08 m s^{-1}	0.1 m s^{-1}	0.3 m s^{-1}
100	112–117°E	110–112°E	116–118°20′E	109–111°30′E	110–112°E	115–118°E
	12–18°N	14–15°N	18–20°20′N	16°40′–20°N	12–14°N	12–14°N
	23°C	21°C	18°C	18°C	20°C	19°C
	0.25 m s^{-1}	0.08 m s^{-1}	0.2 m s^{-1}	0.05 m s^{-1}	0.1 m s^{-1}	0.2 m s^{-1}
200	112–117°E	110–112°E	116–118°20′E	109–113°E		114–117°E
	12–18°N	14–15°N	18–20°20′N	16–18°N		11–14°N
	16°C	15°C	13°C	13.5°C		14°C
	0.1 m s^{-1}	0.04 m s^{-1}	0.1 m s^{-1}	0.04 m s^{-1}		0.09 m s^{-1}
300	115–117°E		110–113°E	116–118°20′E		114–116°E
	12–18°N		18–20°20′N	16–18°N		10–14°N
	12°C		11°C	11°C		11.5°C
	0.02 m s^{-1}		0.03 m s^{-1}	0.01 m s^{-1}		0.03 m s^{-1}

Vertical Structures

Four zonal cross sections (19°N, 17°N, 13°N, and 7°N) of temperature show the vertical structure of the mixed layer and the thermocline as well as the warm and cool pools (Fig. 11.59). The mixed layer was not evident at 19°N cross section but develops as latitude decreases. For 17°N and 7°N cross sections, the mixed layer shallows toward the east. At 13°N cross section, the mixed layer deepens at 114°E. The trough and ridge of the isotherms may be considered as centers of warm and cool pools.

At 19°N cross section, it shows the existence of Dongsha cool pool near 117°E from the uplifting (ridge) of isotherms. The ridge is located at 117°E at the surface, eastward shifted with depth, and kept at 117°E below the 100 m depth. The longitudinal span of Dongsha cool pool is around 2°.

The two cross sections at 17°N and 13°N show the occurrence of a central South China Sea warm pool from the downward bending (trough) of isotherms: 116°E at 17°N and 114°E at 13°N. The longitudinal span of central South China Sea warm pool is around 4° for both latitudes. The warm water is nearly isolated from the surrounding cooler water. This may suggest

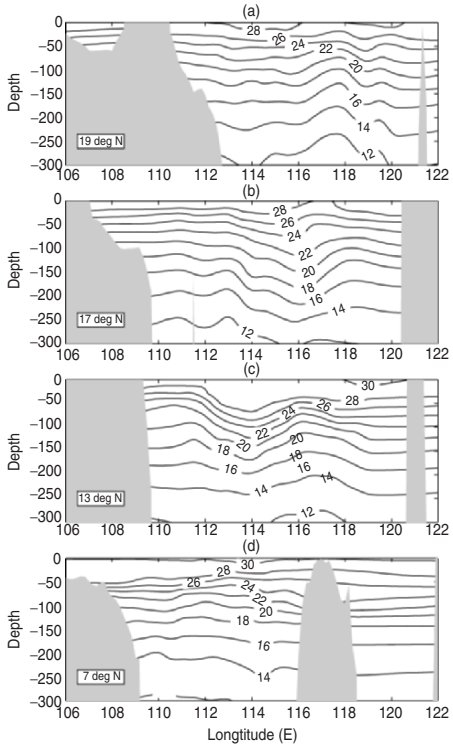

Fig. 11.59. Temperature distribution at several zonal cross sections: (**a**) 19°N, (**b**) 17°N, (**c**) 13°N, and (**d**) 7°N (from Chu et al. 1998d, Journal of Geophysical Research)

that local forcing might be important for the central South China Sea warm pool formation.

At 7°N cross section, it shows the eastward uplift of the thermocline depth from 50 m at 110°E to 25 m at 115°E. A surface warm pool with SST higher than 30°C is found between 112 and 115°E, and a midlevel (100 m) cool pool is detected between 110 and 112°E. In the eastern part (113–115°E), an isolated warm pool appeared below the 175 m depth.

Three latitudinal cross sections (111°E, 114°E, and 117°E) of temperature also show the vertical structure of the mixed layer and the thermocline as well as the warm and cool pools (Fig. 11.60). The mixed layer had a shallow-deep-shallow pattern in the latitudinal direction. Taking 114°E cross section as an example, the mixed layer had a shallow depth (about 10 m) near 5°N. Its depth increased with latitude to about 60 m at 13°30′N and decreased with latitude to almost zero (no mixed layer) near 20°N.

The trough and ridge of the isotherms may be considered as centers of warm and cool pools. The three cross sections indicated the occurrence of

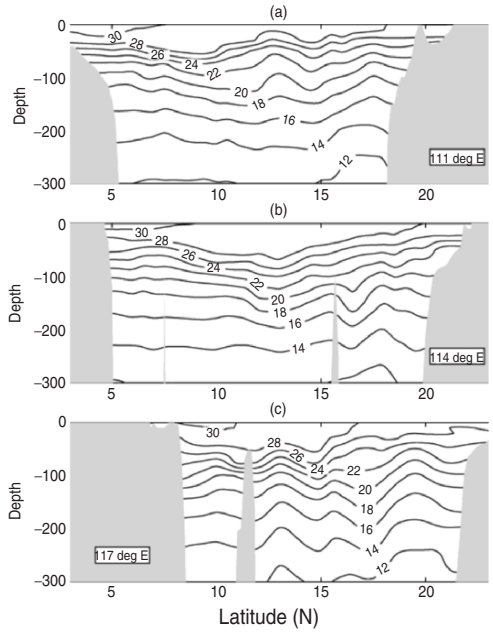

Fig. 11.60. Temperature distribution at several latitudinal cross sections: (**a**) 111°E, (**b**) 114°E, and (**c**) 117°E (from Chu et al. 1998d, Journal of Geophysical Research)

central South China Sea warm eddy evident from the downward bending (trough) of isotherms: 9°N at 111°E, 13°N at 114°E, and 15°N and 17°N at 117°E.

11.9.4 Circulations

T–S and $T - \bar{S}$ relations

The P-vector method for z-level is used to determine the velocity field from hydrographic data. Since there were no salinity (S) observations in the South China Sea during May 14–25, 1995, May WOA climatological salinity is interpolated to the AXBT stations and those salinity values ($\bar{S}$) were used for the P-vector computation. To validate this technique, we plotted two T–S diagrams: one diagram (Fig. 11.61a) is the plot of 3,478 (T, S) profiles from the MOODS in May 1933–1986 and the other diagram (Fig. 11.61b) is the plot of 376 T (AXBT) and $\bar{S}$ profiles. The spatial and temporal distributions of the MOODS data are illustrated in Fig. 11.62a, b. A comparison between the two diagrams shows that the T–S characteristics remain stable. However, we should be aware of the shortcomings in using the climatological salinity values ($\bar{S}$). If the temperature field is relatively homogeneous in space, the density

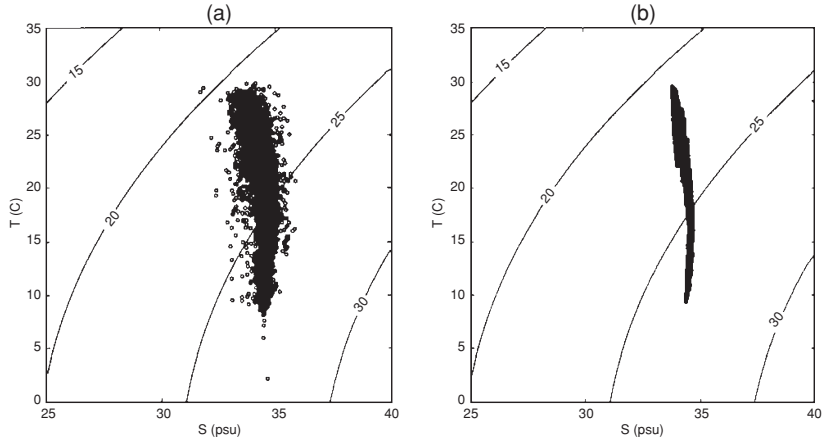

Fig. 11.61. T–S diagrams for (**a**) the MOODS data set in May 1933–1986 and (**b**) the AXBT temperature and May climatological salinity (from Chu et al. 1998d, Journal of Geophysical Research)

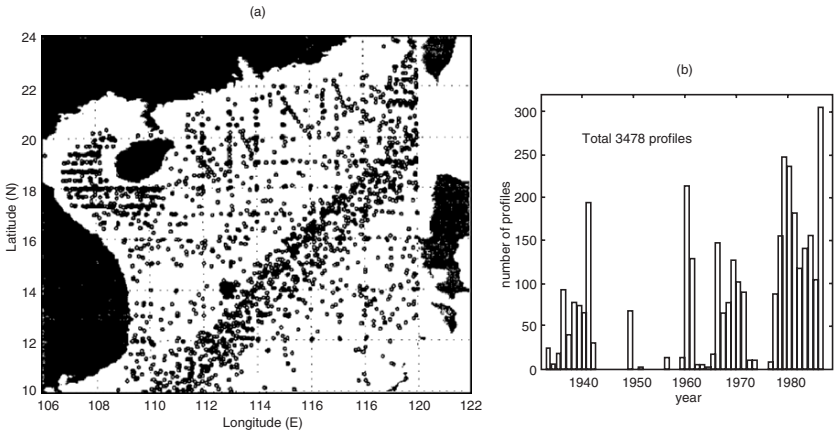

Fig. 11.62. The MOODS data distribution: (**a**) spatial and (**b**) temporal (from Chu et al. 1998d, Journal of Geophysical Research)

gradient depends mostly on the salinity gradient. Under that circumstance, the use of the climatological salinity values may bring large errors in inverting the velocity field.

Horizontal Velocity Fields

The available historical data (Wyrtki 1961a) show two totally different circulation patterns for the months preceding and following the AXBT survey in the central South China Sea: a cyclonic gyre in April (Fig. 11.63a) and an

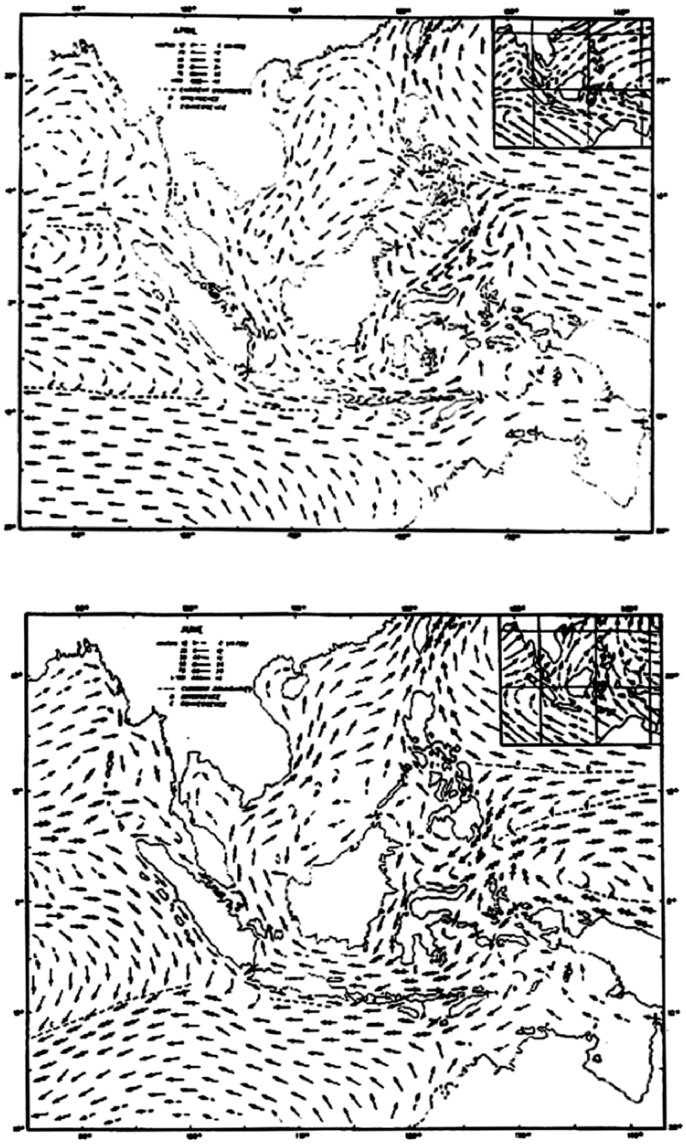

Fig. 11.63. A drastic change of the surface circulation from (**a**) April to (**b**) June (from Wyrtki 1961a)

anticyclonic gyre in June (Fig. 11.63b). We may treat the May circulation as the transition between the two patterns.

The inverted velocity data set (Fig. 11.64) indicates the existence of a central South China Sea anticyclonic gyre surrounded by several cyclonic and anticyclonic eddies. Generally, the anticyclonic (cyclonic) eddies are associated

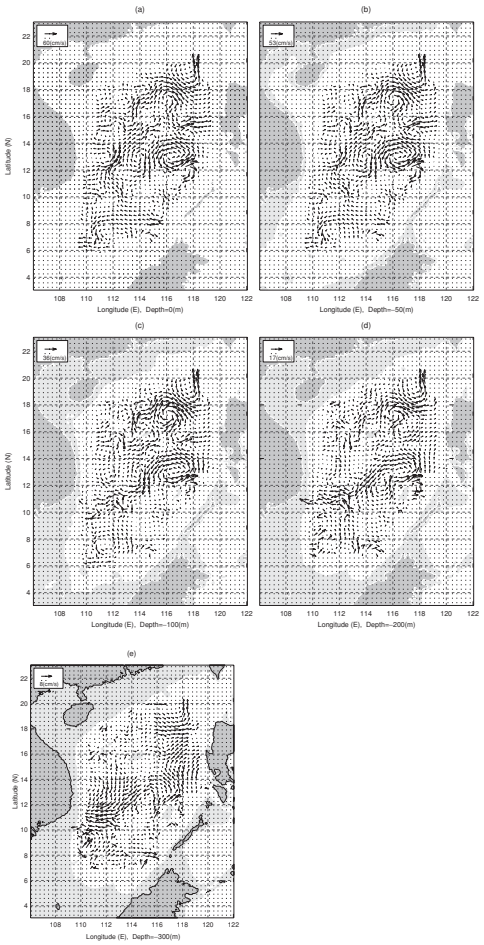

Fig. 11.64. Absolute velocity at different depths: (**a**) 0 m, (**b**) 50 m, (**c**) 100 m, (**d**) 200 m, and (**e**) 300 m. The central South China Sea anticyclonic eddy was surrounded by Dongsha, Hannan, South Vietnamese Bight, and Liyue cyclonic eddies and Xisha anticyclonic eddy (from Chu et al. 1998d, Journal of Geophysical Research)

with the warm (cool) pools. The kinetic features of these eddies are listed in Table 11.2. Furthermore, the magnitude of inverted velocities decreases with depth and is quite small at 300 m. This implies that the geostrophic calculation with the level-of-no-motion at or below about a 300 m depth could have been used to give results close to the P-vector method.

The observed three-dimensional temperature and inverted velocity fields indicate the existence of a central South China Sea warm-core anticyclonic eddy with surrounding Dongsha, Hannan, South Vietnamese Bight, and Liyue cool-core cyclonic eddies and Xisha warm-core anticyclonic eddy (Fig. 11.65).

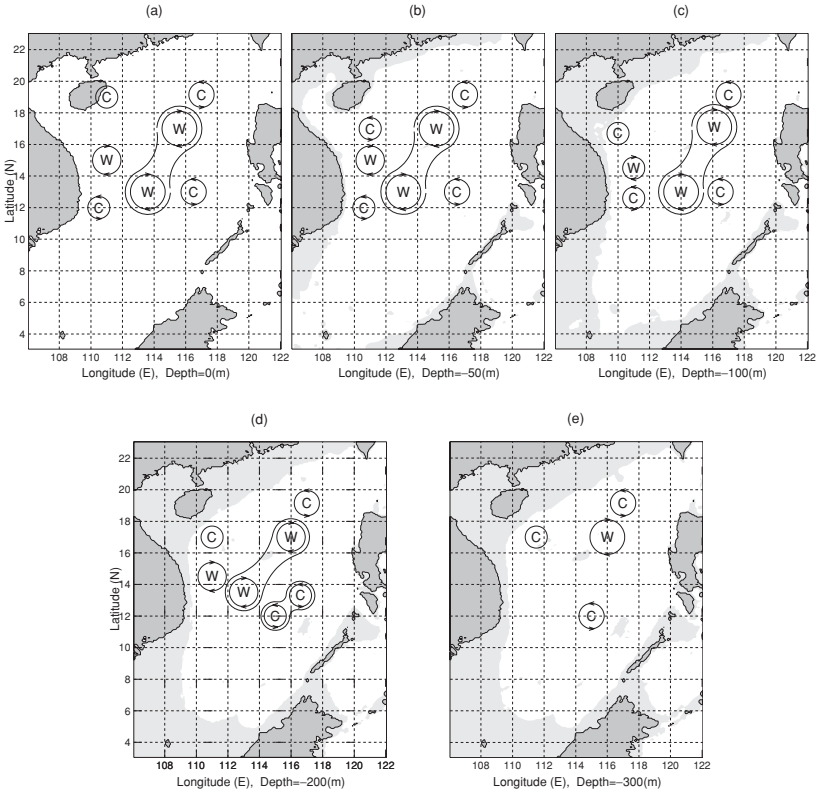

Fig. 11.65. Illustration of South China Sea warm-core and cool-core eddies in May 1995 (from Chu et al. 1998d, Journal of Geophysical Research)

Zonal Cross Sections of v-Component

Four zonal cross sections (19°N, 17°N, 13°N, and 7°N) of v velocity show the vertical eddy structure (Fig. 11.66). The positive values indicate northward velocity, and the negative values refer to the southward velocity. Alternate positive and negative areas indicate the occurrence of cyclonic and anticyclonic eddies. At each zonal cross section, a neighboring eastern negative/western positive pattern refers to an anticyclonic eddy, and, a neighboring western negative/eastern positive pattern refers to a cyclonic eddy.

At 19°N cross section, it shows the existence of the Dongsha cyclonic eddy near 117°E. The diameter of the Dongsha eddy is around 300 km. The depth of the eddy is around 200 m. This eddy reveals an asymmetric feature. The northward velocity with a maximum speed of $0.4\,\mathrm{m\,s^{-1}}$ in the eastern part is stronger than the southward velocity with a maximum speed of $0.1\,\mathrm{m\,s^{-1}}$ in the western part.

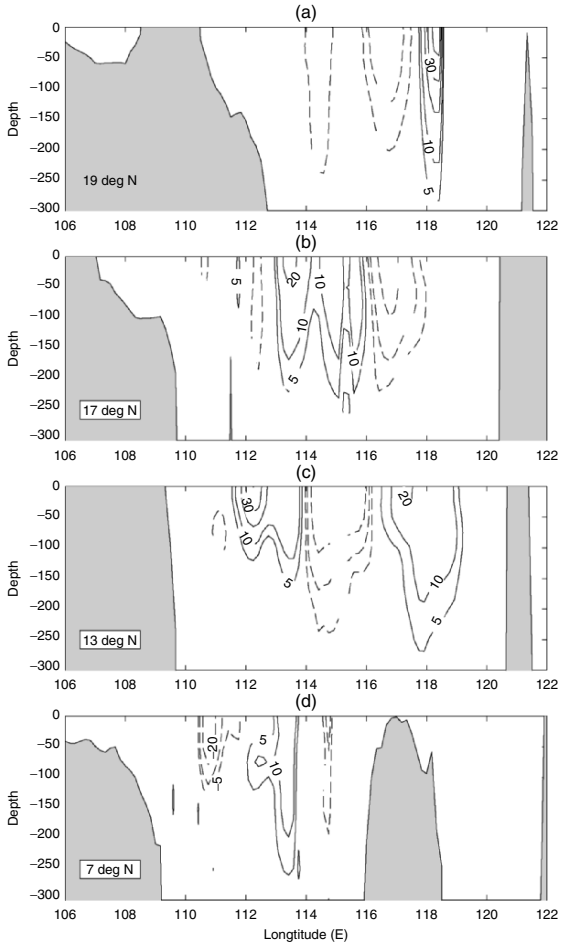

Fig. 11.66. Distribution of velocity v component at several zonal cross sections: (**a**) 19°N, (**b**) 17°N, (**c**) 13°N, and (**d**) 7°N (from Chu et al. 1998d, Journal of Geophysical Research)

At 17°N cross section, it shows the existence of the central South China Sea anticyclonic eddy that is centered at 116°E. The zonal span of the central South China Sea eddy is around 500 km. The depth of the eddy is around 300 m. The maximum tangential velocity is around $0.2\,\mathrm{m\,s^{-1}}$. This eddy is quite symmetric with a maximum southward velocity in the eastern part similar to the northward velocity in the western part.

At 13°N cross section, it shows the existence of a double-eddy structure. Between 112 and 116°E there was a strong anticyclonic eddy (the central South China Sea eddy) with a maximum tangential speed of $0.3\,\mathrm{m\,s^{-1}}$ (appearing in the upper 50 m) and that is centered at 114°E. The zonal span of

this eddy is around 500 km. This anticyclonic eddy is associated with the central South China Sea warm pool. The depth of the eddy is around 250 m. To the east of the anticyclonic eddy, a cyclonic eddy appeared between 114 and 119°E that is centered at 116°20′E. This cyclonic eddy is associated with the Liyue cool pool, and therefore called the Liyue cool-core (cyclonic) eddy. The central South China Sea warm-core eddy and Liyue cool-core eddy shared the same southward branch. Furthermore, the northward flow at the eastern part of the Liyue cool-core eddy (maximum tangential speed around $0.1\,\mathrm{m\,s^{-1}}$) is weaker than the southward flow in the western part.

At 7°N cross section, it shows the occurrence of a cyclonic eddy (110–114°E). This cyclonic eddy is quite asymmetric. The southward flow (maximum tangential speed around $0.2\,\mathrm{m\,s^{-1}}$) in the western part is stronger than the northward flow (maximum tangential speed around $0.1\,\mathrm{m\,s^{-1}}$) in the eastern part. The depth of the eddy is around 150 m. To the east of the anticyclonic eddy, a cyclonic eddy appeared between 114 and 119°E that is centered at 116°20′E.

Latitudinal Cross Sections of u-Component

Three latitudinal cross sections (111°E, 114°E, and 117°E) of u velocity also show the vertical eddy structure (Fig. 11.67). The positive values indicate eastward velocity, and the negative values refer to westward velocity. Alternate positive and negative areas indicate the occurrence of cyclonic and anticyclonic eddies. At each latitudinal cross section, a neighboring southern negative/northern positive pattern refers to an anticyclonic eddy. However, a neighboring northern negative/southern positive pattern refers to a cyclonic eddy.

The area with a southern negative/northern positive u pattern (anticyclonic eddy) coincides with the area of the downward bending isotherms (warm pool). At 111°E cross section, the central South China Sea warm-core eddy is identified by an isotherm trough located at 9°N (Fig. 11.65), and an anticyclonic eddy is identified by the southern negative/northern positive u pattern that is centered at 9°N (Fig. 11.67). At the 114°E cross section, the central South China Sea warm-core eddy is identified by an isotherm trough located at 13°N (Fig. 11.65), and an anticyclonic eddy is identified by the southern negative/northern positive u pattern that is centered at 13°N (Fig. 11.67).

11.9.5 Mechanisms

In searching mechanisms for the formation of this recurring seasonal signal, a central South China Sea warm anomaly, Chu et al. (1997d) found a high correlation between surface wind stress curl and SST anomaly from correlation analysis of the European Center for Medium-range Weather Forecast (ECMWF) analyzed wind stress data and the NCEP SST data. The high correlation leads to a hypothesis for the wind-driven central South China Sea warm pool during the spring-to-summer monsoon transition. The bowl-type

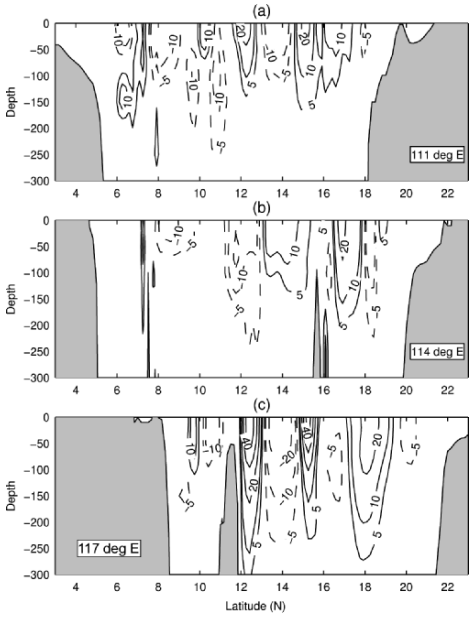

Fig. 11.67. Distribution of velocity u component at several latitudinal cross sections: (**a**) 111°E, (**b**) 114°E, and (**c**) 117°E (from Chu et al. 1998d, Journal of Geophysical Research)

bottom topography (Fig. 11.68) provides a favorable condition for the central South China Sea warm pool formation in the spring-to-summer monsoon transition. In spring, a surface anticyclone usually appears over the central South China Seas (Cheang 1980). Ekman downwelling will occur in the central part of the "bowl," and mass balance will cause upwelling near the boundary of the bowl. The downwelling prevents the deep cold water from upward advection, while the upwelling along the boundary helps the upward advection of deep cold water. This makes the central part of the bowl warm and the side part of the bowl cool and leads to the generation of the central South China Sea warm pool surrounded by several cool pools. Furthermore, other mechanisms such as remote forcing and topographic influence could be significant. This wind-driven mechanism for the formation of a central South China Sea warm-core eddy with surrounding cool-core eddies during the spring-to-summer transition was confirmed by a numerical study (Chu et al. 1998c).

11.10 Low Salinity Cold-Core Cyclonic Eddy Northwest of Luzon

Last section shows the existence of six eddies in the South China Sea from an AXBT survey conducted in May 1995 and historical salinity data using the

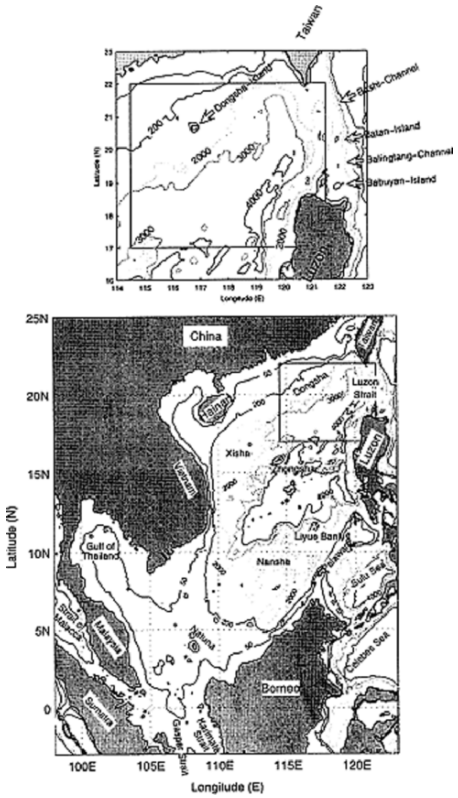

Fig. 11.68. Geography and isobaths showing the bottom topography of the South China Sea. The shaded box shows the survey area containing 307 AXBT and 9 AXCTD stations in July 1998 (from Chu and Fan 2001d, Journal of Oceanography)

P-vector inverse method (see Fig. 11.65): dual warm-core anticyclonic eddies in the central South China Sea and four surrounding cold-core cyclonic eddies located at northwest of the Luzon Island, southeast of the Hainan Island, South Vietnamese bight, and Liyue Bank. In the upper layer the tangential velocity of the dual central South China Sea anticyclonic warm-core eddies is around 0.3–0.4 $\mathrm{m\,s^{-1}}$ and that of the four cool-core cyclonic eddies varies from 0.1 to 0.4 $\mathrm{m\,s^{-1}}$. The tangential velocities of all eddies decrease with depth. At 300 m depth, it became less than 0.05 $\mathrm{m\,s^{-1}}$. Among these eddies, an eddy northwest of Luzon Island is of interest because it may affect the Kuroshio water entering the South China Sea due to its location.

11.10.1 Two Regimes

Two regimes (bifurcation and loop) of the northeast South China Sea (116–120°E, 18–23°N) circulation can be identified based on the character-

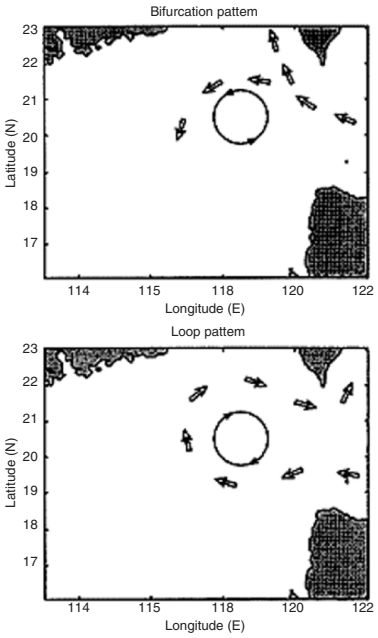

Fig. 11.69. Two regimes of the northeast South China Sea circulation: (**a**) bifurcation pattern, and (**b**) loop pattern (from Chu and Fan 2001, Journal of Oceanography)

istics of the major eddy (i.e., the northwestern Luzon eddy) in the area. If this eddy is cyclonic (Qiu et al. 1985; Chu and Fan 2001), the northeast South China Sea circulation takes the bifurcation pattern: The Kuroshio water is intruded into the South China Sea through the whole Luzon Strait and bifurcated into northward and northwestward branches before impinging the eddy. The northwestward branch was circulating around the cyclonic eddy (Fig. 11.69a). If this eddy is anticyclonic (Li et al. 1998), the northeast South China Sea circulation takes the loop pattern (Metzger and Hurlburt 1996). The Kuroshio water is intruded into the South China Sea through the southern Luzon Strait. It loops around the anticyclone, exits the South China Sea through the northern Luzon Strait, and rejoins the Kuroshio currents (Fig. 11.69b).

The northwestern Luzon eddy was claimed to be either cold-core cyclonic or warm-core anticyclonic from geostrophic shear calculated from hydrographic data. For example, Nitani (1970) used limited data to identify this eddy to be cold-core cyclonic and occurring in the summer. Xu et al. (1982) used historical (1921–1970) hydrographic data to identify this eddy to be cold-core cyclonic and occurring in the winter. Zhou et al. (1995) confirmed the occurrence of the northwestern Luzon cold-core cyclonic eddy in both winter and summer using the climatological monthly mean temperature and salin-

ity data. Recently, Li et al. (1998) analyzed the hydrographic data collected during a major expedition of the Northeastern South China Sea Circulation Cooperative Study in August–September 1994 and identified the northwestern Luzon eddy to be warm-core anticyclonic. All of these observational studies are based on the level-of-no-motion assumption. For example, Xu et al. (1982) and Li et al. (1998) assumed 1,200 and 1,000 db as the level-of-no-motion, respectively.

11.10.2 Observations

To remove the level-of-no-motion assumption, Chu et al. (1998d) (see Sect. 11.9) used the P-vector inverse method to identify the northwestern cold-core cyclonic eddy from an extensive AXBT survey conducted in May 1995 and historical salinity data. A weakness of the study (Chu et al. 1998d) is the use of the synoptic temperature data and the climatological salinity data. The incompatible T, S data may lead to some error in the inversion of absolute velocity.

One objective of SCSMEX is to detect the South China Sea eddy features. During the intensive observational period of the SCSMEX in July 1998, the US Naval Oceanographic Office conducted an intensive airborne expendable hydrographic survey of the northeast South China Sea on July 8–26, 1998. The Chinese Academy of Sciences conducted the ADCP measurements on R/V Shiyan3. The airborne hydrographic survey includes 307 AXBT stations and 9 AXCTD stations, uniformly distributed in the region (114°30′–121°30′E, 17–22°N) that is shown in Fig. 11.68 as the shaded box. Due to Navy regulations, it is unable to present the T, S station distribution. The maximum depth of the observations is 400 m. This data set provides something close to a "snapshot" of the temperature and salinity in the upper ocean in the northeast South China Sea in July 1998. With synoptic T, S data, we may obtain a more accurate estimation of the northwestern Luzon eddy using the P-vector inverse method. The 307 AXBTs and 9 AXCTDs were deployed over a period of July 8–26, 1998. The majority of the AXBTs/AXCTDs were nominally capable of reaching a depth of 400 m. The vertical resolution of the measurements is 1 m. The T–S diagram of the AXCTD data (Fig. 11.70) shows the typical northeast South China Sea water depicted by Li et al. (1998): The salinity maxima are less than 34.7 ppt and the salinity minima are larger than 34.40 ppt.

The in situ density with 1 m vertical resolution is computed from the 9 AXCTD stations. Horizontal average of 316 temperature stations, nine salinity stations, and nine in situ density profiles at each depth leads to the vertical mean profiles of temperature $\bar{T}(z)$, salinity $\bar{S}(z)$, and density $\bar{\rho}(z)$. From the mean density profile, the buoyancy frequency is computed,

$$N = \sqrt{-\frac{g}{\rho_0}\frac{\mathrm{d}\bar{\rho}(z)}{\mathrm{d}z}}. \tag{11.4}$$

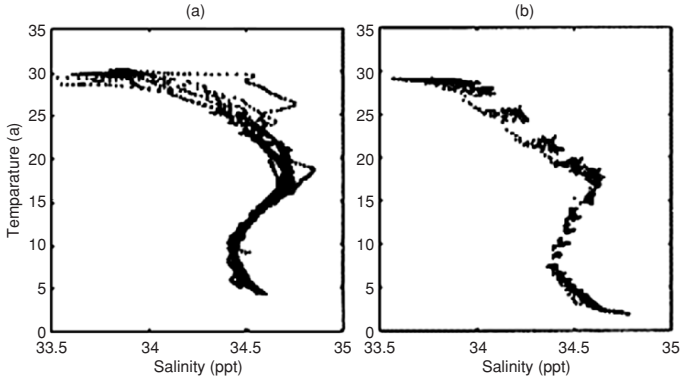

Fig. 11.70. (**a**) T–S diagram constructed from the AXCTD data, and (**b**) $\hat{T} - \hat{S}$ diagram constructed from the interpolated data (from Chu and Fan 2001, Journal of Oceanography)

The mean temperature profile shows a very shallow mixed layer with the depth less than 20 m (Fig. 11.71a). Below the mixed layer, the mean temperature reduces rapidly with depth from 29.5°C at the base of the mixed layer (20 m) to 20°C at the 100 m depth, and then reduces slowly with depth from 20°C at the 100 m depth to 10°C at the 400 m depth.

The mean salinity profile (Fig. 11.71b) shows the existence of salinity maxima (34.63 ppt) located at the 125–175 m depths and of salinity minima (34.43 ppt) located at the 400 m depth. The mean density profile (Fig. 11.71c) shows that the vertical variability of $\bar{\rho}(z)$ follows the vertical variability of $\bar{T}(z)$. The buoyancy frequency (Fig. 11.71d) increases with depth from 0 at the surface to a maximum value ($0.026\,\mathrm{s}^{-1}$) at the 45 m depth and then tends to reduce with depth to a minimum value ($0.007\,\mathrm{s}^{-1}$) at the 400 m depth.

The same as in Sect. 11.9, the AXBT/AXCTD observations were mapped at each depth using a two-scale OI scheme (Gandin 1965; Lozano et al. 1996). The large-scale OI was used to estimate the background mean with a decorrelation scale of 450 km. The mesoscale OI was used to map the observational anomaly from the background mean field into a regular grid with a spatial decorrelation scale of 75 km and a temporal decorrelation scale of 10 days.

The spatial and temporal decorrelation scales associated to the mean field were estimated from the covariance matrix obtained from the MOODS for the South China Sea (Chu et al. 1997c). The large-scale mean was computed using the temperature and salinity profiles. The large-scale pattern for the surface (not shown) resembles the pattern previously estimated by Chu et al. (1997c). The decorrelation length scale for the fluctuations from the mean was estimated from the AXBT data. The results shown below are relatively insensitive to the length scale in the range of 60–90 km. The decorrelation timescale was selected to ensure synopticity. The SST horizontal scales seem rather larger than temperatures in the seasonal thermocline. In this study, we choose

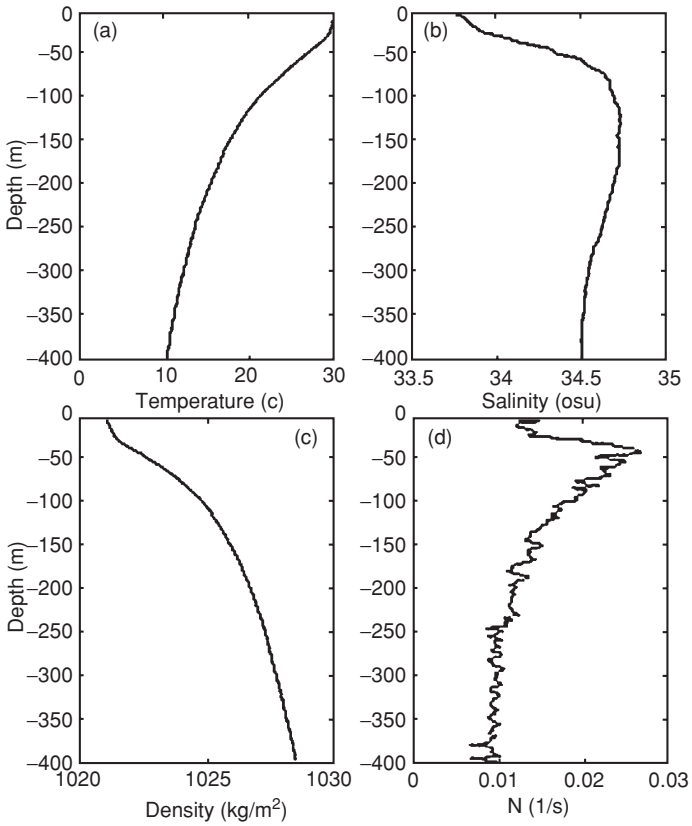

Fig. 11.71. Mean vertical profiles of (**a**) temperature, (**b**) salinity, (**c**) density, and (**d**) buoyancy frequency (from Chu and Fan 2001, Journal of Oceanography)

horizontal scales to be uniform in the vertical for convenience and for lack of sufficient data to discriminate these differences properly.

The current observations were made from R/V Shiyan3 on 16–21 July 1998. That vessel was equipped with an ADCP and a global position system (GPS) receiver. This system measured currents underway from depths of about 10–250 m in 4 m depth bins. Five minute averages were recorded.

11.10.3 Temperature

Horizontal Structure

Figure 11.72 shows the horizontal depictions of temperature at nine different depths from the surface to the 400 m depth, with 50 m interval. A cold-core ring is located northwest of Luzon Island (116–119°E, 19–21.5°N) with surrounding warmer water. The cold-core was evident at all levels, 1–2°C cooler

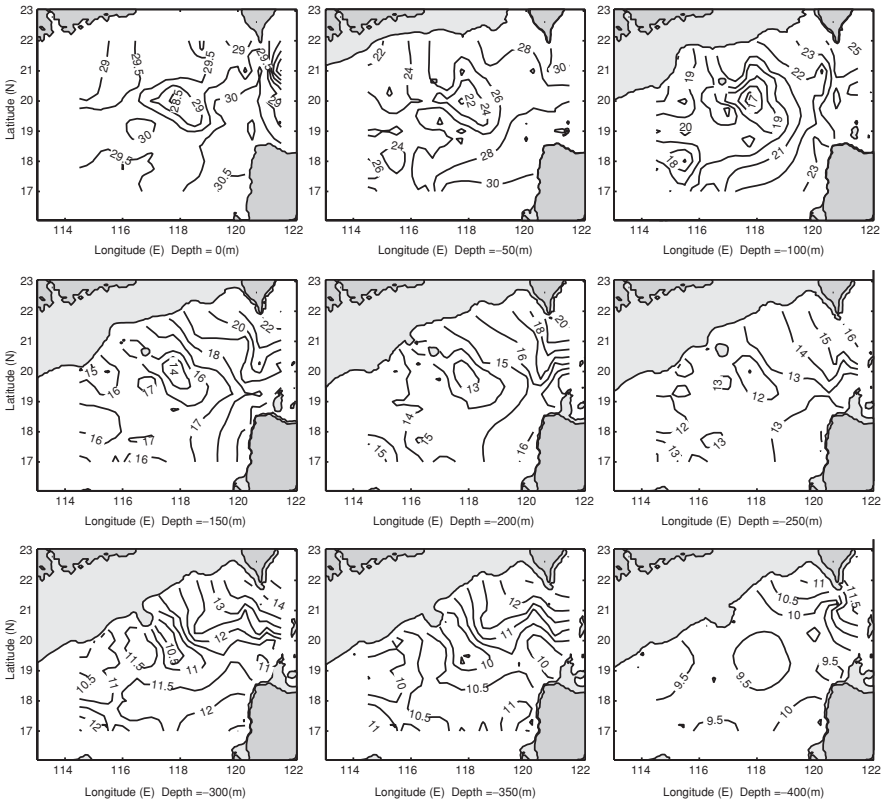

Fig. 11.72. Horizontal temperature fields at nine different depths from the surface to 400 m at 50 m intervals. Cooler water is situated northwest of Luzon Island (116–119°E, 19–21.5°N), surrounded by warmer water (from Chu and Fan 2001, Journal of Oceanography)

inside than outside of the eddy. The location and thermal features of the northwestern Luzon cold-core eddy are listed in Table 11.3.

Vertical Structure

Six zonal cross sections, from 17 to 22°N, of temperature (Fig. 11.73) show the vertical layered structure (mixed layer, thermocline, and layer below the thermocline). A cold-core can be identified by the uplifting (ridge) of isotherms and a warm-core can be identified from the downward bending (trough) of the isotherms.

The mixed layer is not evident at 22°N cross section but becomes evident as latitude decreases. From 21 to 17°N cross sections, the mixed layer shallows toward the west. A shallow layer (< 50 m depth) of warm water with temperature higher than 30°C occurs in Luzon Strait (120–120.7°E) at 20°N

Table 11.3. Location, typical temperature, salinity, and tangential velocity of the northwestern Luzon low salinity cool-core cyclonic eddy (from Chu 2001, Journal of Oceanography)

Depth (m)	location	T (°C)	S (ppt)	Max tangential velocity ($\mathrm{m\,s^{-1}}$)
0	19–21°N; 116.5–119°E	28.5	33.60	0.50
50	18.8–21.5°N; 116.5–119°E	22.0	34.40	0.45
100	18.8–21.5°N; 116.75–119°E	17.0	34.52	0.20
150	19–20.8°N; 116.5–119°E	14.0	34.64	0.12
200	18.5–21°N; 117–119°E	13.0	34.56	0.06
250	19–21°N; 116.5–119°E	12.0	34.50	0.06
300	18.8–20.8°N; 117–119°E	10.5	34.46	0.05

cross section. This warm water westward extends as the latitude decreases. At 17°N cross section, the warm water ($T > 30$°C) reaches 117°E.

The cross sections from 21 to 19°N clearly show the existence of the northwestern Luzon cold-core near 117.5°E from the uplifting (ridge) of isotherms. Taking 20°N cross section as an example, the ridge is located at 117.8°E from the surface to the 400 m depth. The longitudinal span of the northwestern Luzon cold eddy is around 300 km.

Six latitudinal cross sections from 116 to 121°E of temperature (Fig. 11.74) show the same vertical layered structure (mixed layer, thermocline, and layer below the thermocline). The mixed layer shallows toward the north in the western cross sections (115–116.5°E). A shallow layer (< 50 m depth) of warm water ($T > 30$°C) occurs in the southern part of the Luzon Strait (south of 20.3°N) at 120°E cross section. This warm water retreats toward the south as the longitude decreases. At the 117°E cross section, the warm water ($T >$ 30°C) disappears.

The cross sections from 117 to 119°E show the existence of the northwestern Luzon cold-core eddy near 18–21°N from the uplifting (ridge) of isotherms. Taking 118°E cross section as an example, the ridge is located at 20°N from the surface to the 400 m depth. The latitudinal span of the northwestern Luzon cold eddy is around 300 km.

11.10.4 Salinity

Horizontal Structures

Figure 11.75 shows the horizontal depictions of salinity at nine different depths from the surface to the 400 m depth with 50 m interval. In them, we see low salinity centers associated with the northwestern Luzon cold-core eddy at various depths: a low salinity center ($S < 33.60$ ppt) with the northwestern Luzon cold-core ($T < 29$°C) at the surface, a low salinity tongue ($S < 34.64$ ppt) ($T < 14$°C) at 150 m depth, and a low salinity center ($S < 34.45$ ppt) ($T < 9.5$°C) at the 400 m depth.

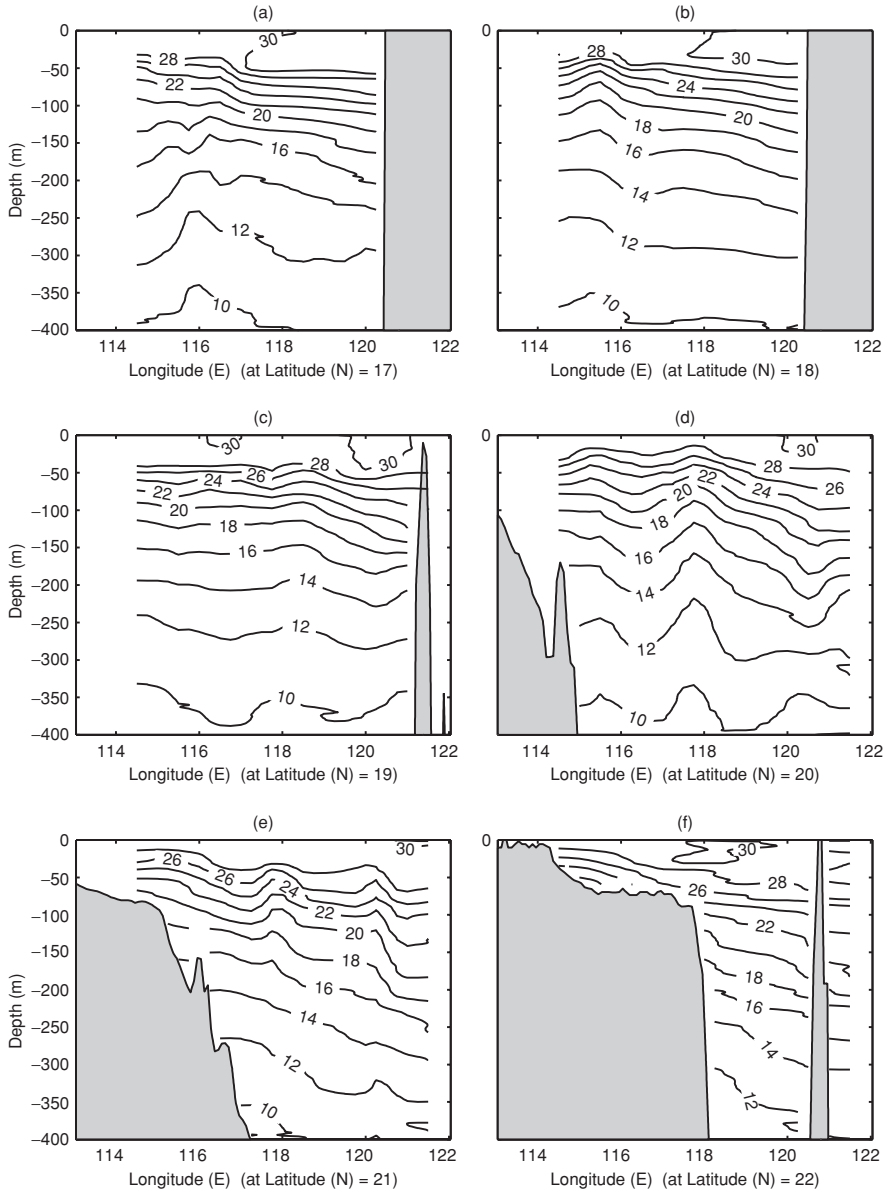

Fig. 11.73. Temperature distribution at several zonal cross sections: (**a**) 17°N, (**b**) 18°N, (**c**) 19°N, (**d**) 20°N, (**e**) 21°N, and (**f**) 22°N (from Chu and Fan 2001, Journal of Oceanography)

Vertical Structures

Six zonal cross sections, from 17 to 22°N, of salinity (Fig. 11.76) show a strong northward uplifting of halocline. The halocline occurs between 30 and 50 m depths north of 20°N and 40–75 m depths south of 20°N.

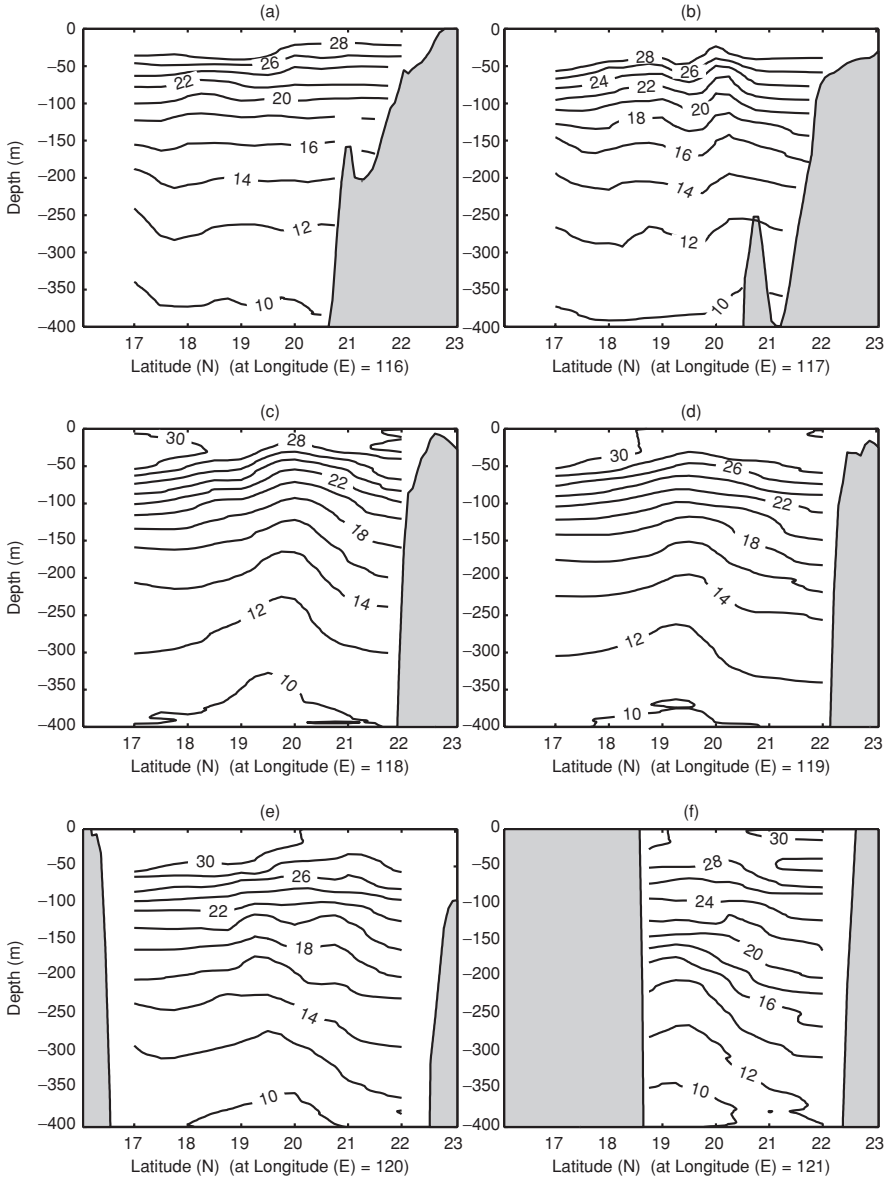

Fig. 11.74. Temperature distribution at several latitudinal cross sections: (**a**) 116°E, (**b**) 117°E, (**c**) 118°E, (**d**) 119°E, (**e**) 120°E, and (**f**) 121°E (from Chu and Fan 2001, Journal of Oceanography)

The strength of the halocline decreases toward south. The cross sections of 17°–18°N show an evident westward uplifting of the halocline. Below the halocline, salinity maxima (> 34.7 ppt) can be identified from all the cross

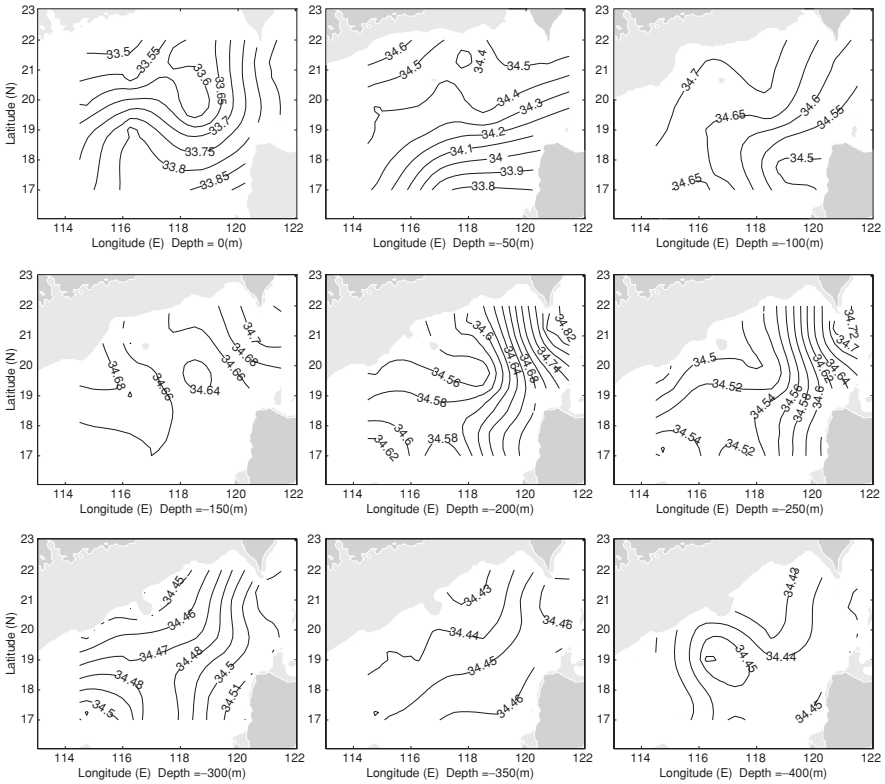

Fig. 11.75. Horizontal salinity fields at nine different depths from the surface to 400 m at 50 m intervals. Fresher water is situated northwest of Luzon Island, surrounded by saltier water (from Chu and Fan 2001, Journal of Oceanography)

sections with shallow depths (100–150 m) west of 119°E and with deep depths (150–250 m) east of 119°E. A low salinity-core can be identified by the uplifting of the isohalines or by sandwiching between the two salinity maxima. Looking at 20°N cross section, the western salinity maxima occurs west of 119°E between 100 and 150 m depths, and the eastern salinity maxima occurs east of 120°E between 150 and 250 m depths. Between the two salinity maxima, there exists a low salinity area, which is colocated with the northwestern Luzon cold-core eddy.

Six latitudinal cross sections, from 115 to 121°E, of salinity (Fig. 11.77) show the same features as Fig. 11.76 with the strong halocline occurring at all the cross sections. The halocline has a clear northward uplifting.

The bottom of the halocline is located at around 75 m depth at 17°N and at near 50 m depth at 22°N. The strength of the halocline on the latitudinal cross sections decreases eastward. Below the halocline, two salinity maxima (north and south) can be identified from several cross sections with a salinity

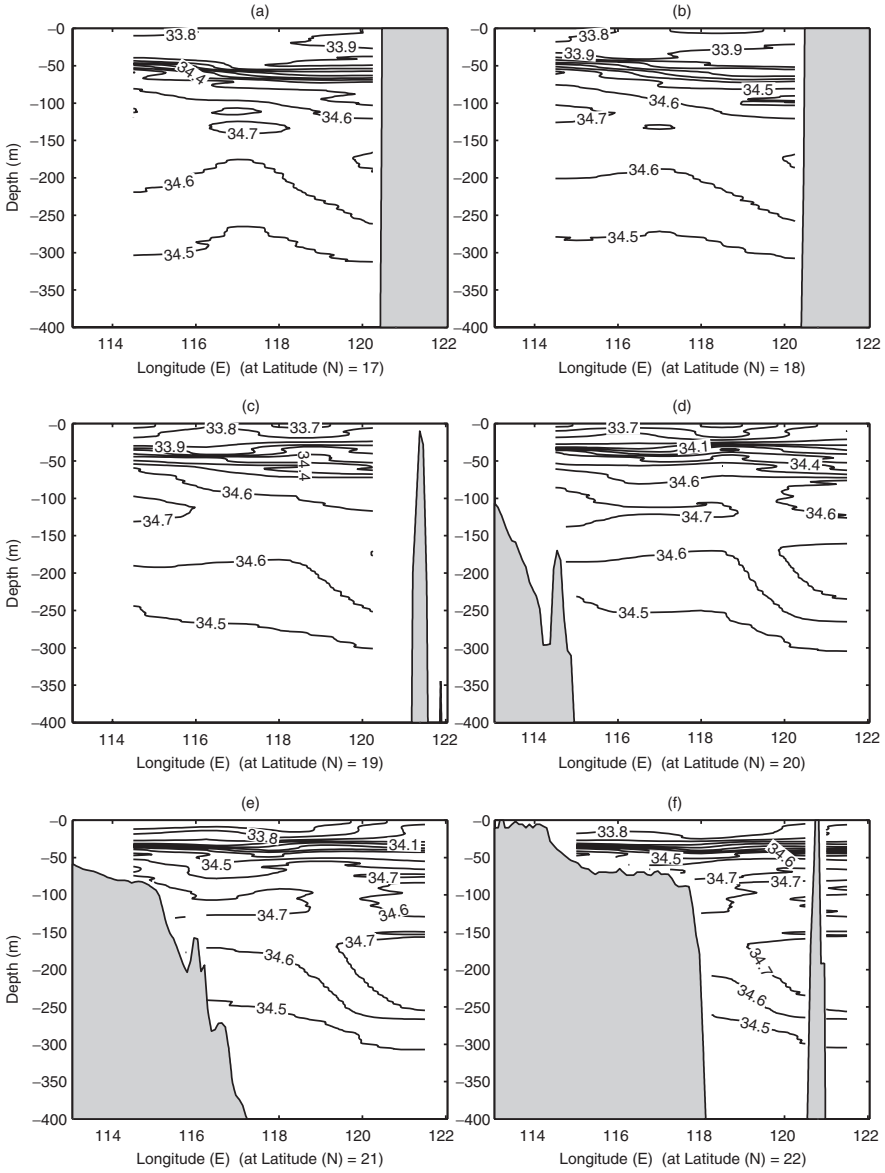

Fig. 11.76. Salinity distribution at several zonal cross sections: (**a**) 17°N, (**b**) 18°N, (**c**) 19°N, (**d**) 20°N, (**e**) 21°N, and (**f**) 22°N (from Chu and Fan 2001, Journal of Oceanography)

minimum in between them. Looking at the 117°E cross section, the southern salinity maximum (> 34.7 ppt) occurs south of 18.2°N between 120 and 150 m depths, and the northern salinity maximum (> 34.7 ppt) occurs north of 19.5°N between 75 and 125 m depths. Between the two salinity maxima,

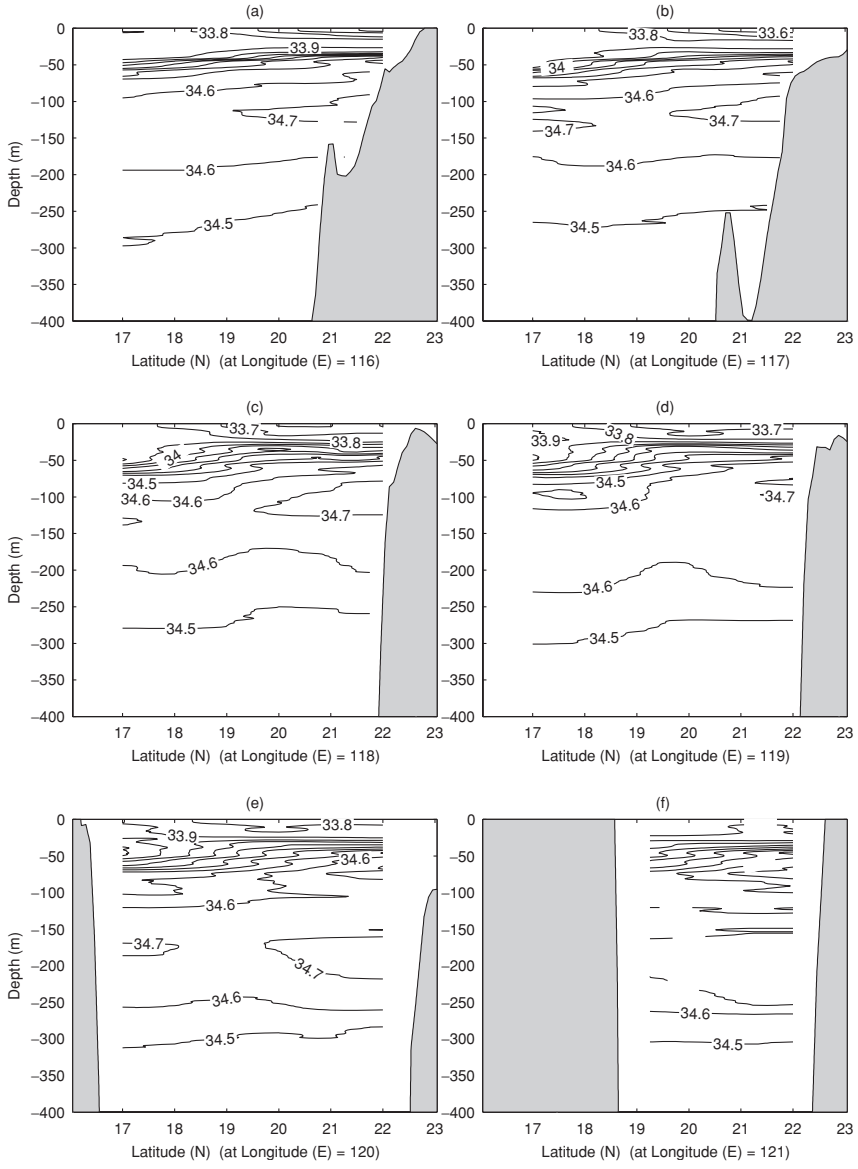

Fig. 11.77. Salinity distribution at several meridional cross sections: (**a**) 116°E, (**b**) 117°E, (**c**) 118°E, (**d**) 119°E, (**e**) 120°E, and (**f**) 121°E (from Chu and Fan 2001, Journal of Oceanography)

there exists a low salinity area, which is colocated with the northwestern Luzon cold-core eddy. Thus, the salinity is usually lower inside than outside of the northwestern Luzon cold-core eddy.

11.10.5 Velocity

Horizontal Structure

The inverted velocity vectors near Luzon Strait (Fig. 11.78) clearly show a pattern of upper layer (above 200 m depth) apparent Kuroshio intrusion and lower layer (below 200 m depth) weak outflow. The upper layer flow pattern is quite similar to the bifurcation pattern depicted in Fig. 11.69a. In this figure the upper layer intruded Kuroshio water bifurcated into northward and northwestward branches west of the Balingtang Channel (120°20′E, 19°30′N). The northwestward branch was circulating around the cold-core area (116–119°E, 19–21.5°N) and formed a cyclonic eddy (i.e., upper part of the northwestern Luzon baroclinic eddy). The maximum tangential velocity of the eddy decreased with the depth from around $0.5\,\mathrm{m\,s^{-1}}$ at the surface to $0.06\,\mathrm{m\,s^{-1}}$ at 200 m depth. The radius of the eddy was around 150 km. There was a smaller and weaker anticyclonic eddy associated with the warm-core ring southwest of the northwestern Luzon eddy.

Comparing Fig. 11.78 with Figs. 11.72 and 11.75, we may find that the northwestern Luzon cyclonic eddy has lower temperature and salinity than the surroundings. The location and kinetic features of the northwestern Luzon eddy at different depths are listed in Table 10.1. Several weak and small eddies are also found west and southwest of the northwestern Luzon eddy.

The current vectors at 50 m as measured by the ADCP aboard R/V Shiyan3 are shown in Fig. 11.79. At this depth, a cyclonic eddy can be identified. It was centered at 118°E, 19.5°N with the zonal span of around 300 km. The maximum velocity is $1\,\mathrm{m\,s^{-1}}$, which is higher than the speed inverted from the hydrographic data.

Zonal Cross Sections of v Component

Six zonal cross sections, from 17 to 22°N, of v-velocity show the vertical structure of the northwestern Luzon eddy (Fig. 11.80). The positive values indicate northward velocity, and the negative values refer to the southward velocity. Between 116 and 119°E (the zonal span of the northwestern Luzon eddy), the northwestern Luzon baroclinic eddy can be identified by alternate positive and negative areas at the zonal cross sections of 19°N, 20°N, and 21°N. At each zonal cross section, we found a cyclonic rotation in the upper layer (surface to 200 m depth) from a neighboring eastern positive/western negative pattern and an anticyclonic rotation in the lower layer (below the 200 m depth) from a neighboring eastern negative/western positive pattern. The upper layer cyclonic rotation was quite strong with the maximum v-velocity higher than $0.3\,\mathrm{m\,s^{-1}}$. The lower layer anticyclonic rotation was weaker with the maximum v-velocity around $0.1\,\mathrm{m\,s^{-1}}$.

The area with a southern cyclonic eddy in the upper layer (surface to the 200 m depth) coincides with the area of the uplifting isotherms (cold-core).

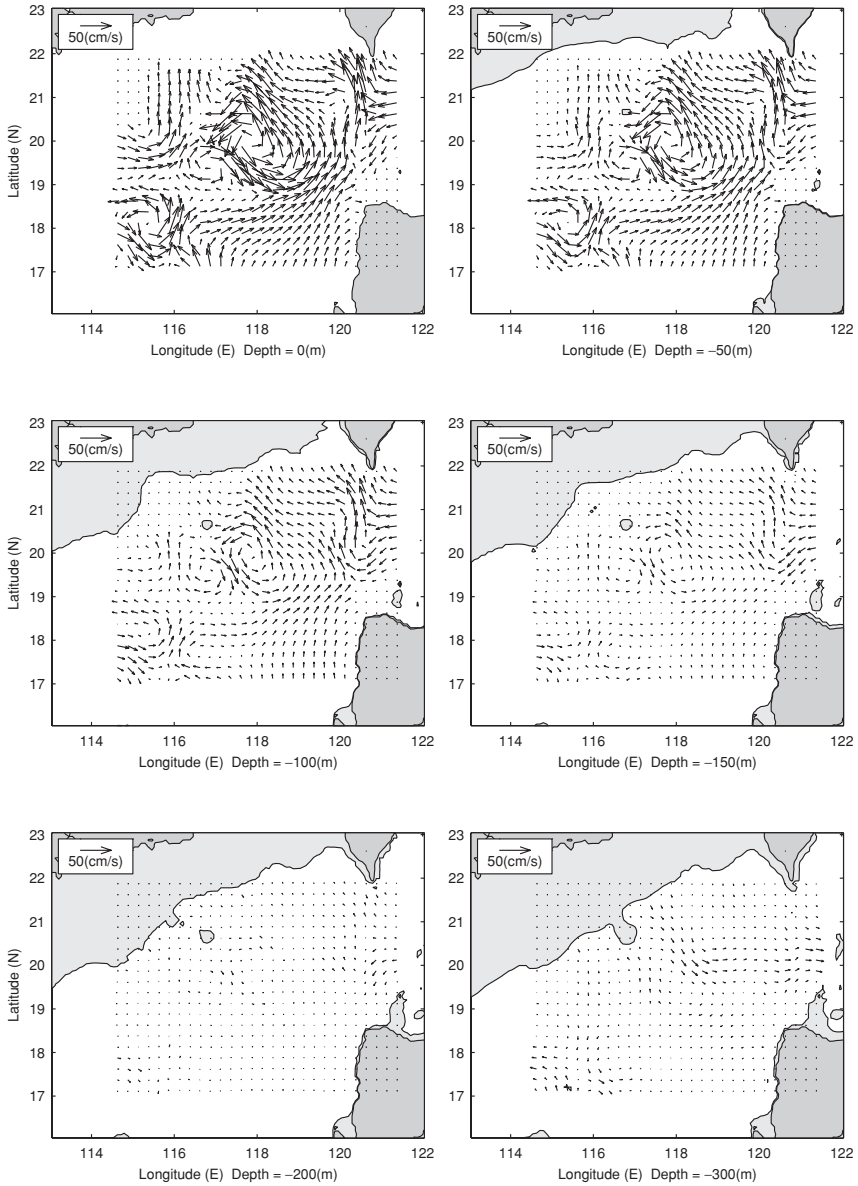

Fig. 11.78. Absolute velocity vectors at different depths: (**a**) 0 m, (**b**) 50 m, (**c**) 100 m, (**d**) 200 m, and (**e**) 300 m. The northwestern Luzon baroclinic eddy is cyclonic in the upper layer from the surface to 200 m depth and anticyclonic in the lower layer below 200 m depth (from Chu and Fan 2001, Journal of Oceanography)

At the 118°E cross section, the northwestern Luzon cold-core eddy is recognized by an isotherm ridge located at 19.5°N (Fig. 11.74). A strong cyclonic

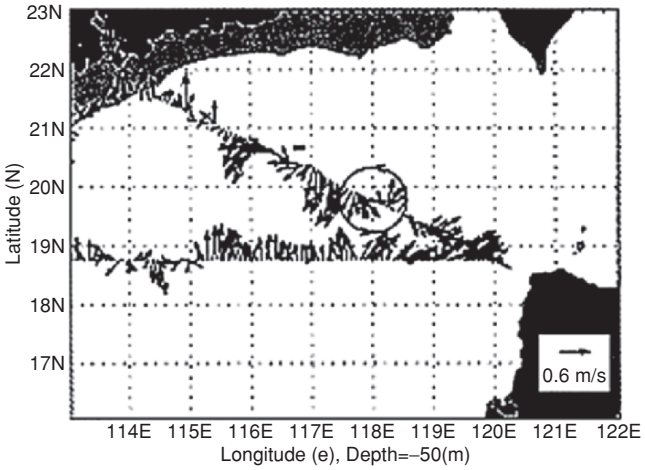

Fig. 11.79. ADCP velocity vectors (15 min averages) at 50 m depth measured during the SCSMEX on 16–21 July 1998 from R/V Shiyan3. Note the cyclonic circulation pattern centered 118°E, 19.5°N with the zonal span of around 300 km. The maximum velocity is $1\,\mathrm{m\,s^{-1}}$ (from Chu and Fan 2001, Journal of Oceanography)

eddy with the maximum speed of $0.5\,\mathrm{m\,s^{-1}}$ is identified by the southern positive/northern negative u pattern that is centered at 19.5°N in the upper layer (above the 250 m depth) and a weak anticyclonic eddy with the maximum speed of $0.1\,\mathrm{m\,s^{-1}}$ is identified by the southern negative/northern positive u pattern that is also centered at 19.5°N (Fig. 11.80) in the lower layer (below the 250 m depth).

11.10.6 Energy Budget of the Northwestern Luzon Eddy

Mean Kinetic Energy

The horizontal mean kinetic energy per unit mass is computed at each depth,

$$\bar{u}(z) = \frac{1}{M}\sum_i\sum_j u(x_i, y_j, z), \quad \bar{v}(z) = \frac{1}{M}\sum_i\sum_j v(x_i, y_j, z), \tag{11.5}$$

where M is the total number of the horizontal grid points. The mean kinetic energy $\bar{K}$ is defined by

$$\bar{K}(z) = \frac{1}{2}[\bar{u}(z)^2 + \bar{v}(z)^2]. \tag{11.6}$$

Figure 11.81a shows the vertical profile of the mean kinetic energy. The mean kinetic energy, $\bar{K}$, has the maximum value of $3.5 \times 10^{-3}\,\mathrm{m^2\,s^{-2}}$ at the surface. It decreases with the depth from the surface maximum value to zero at the 200 m depth. Between 200 and 250 m, the mean kinetic energy is very small (near zero). Below the 250 m depth, the mean kinetic energy slightly increases with the depth.

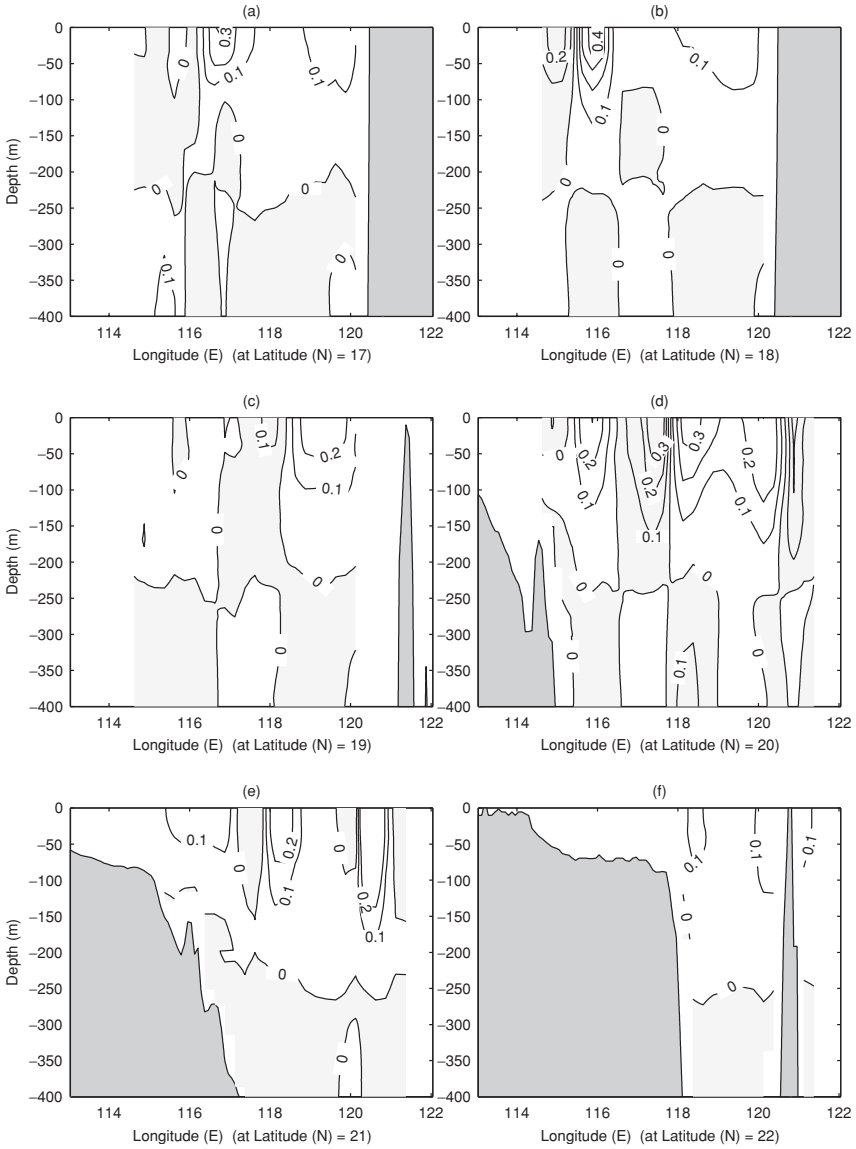

Fig. 11.80. Distribution of inverted velocity v component at several zonal cross sections: (**a**) 17°N, (**b**) 18°N, (**c**) 19°N, (**d**) 20°N, (**e**) 21°N, and (**f**) 22°N (from Chu and Fan 2001, Journal of Oceanography)

Eddy Kinetic Energy

The eddy kinetic energy can be computed by

$$K' = \frac{1}{2}(u'^2 + v'^2), \tag{11.7}$$

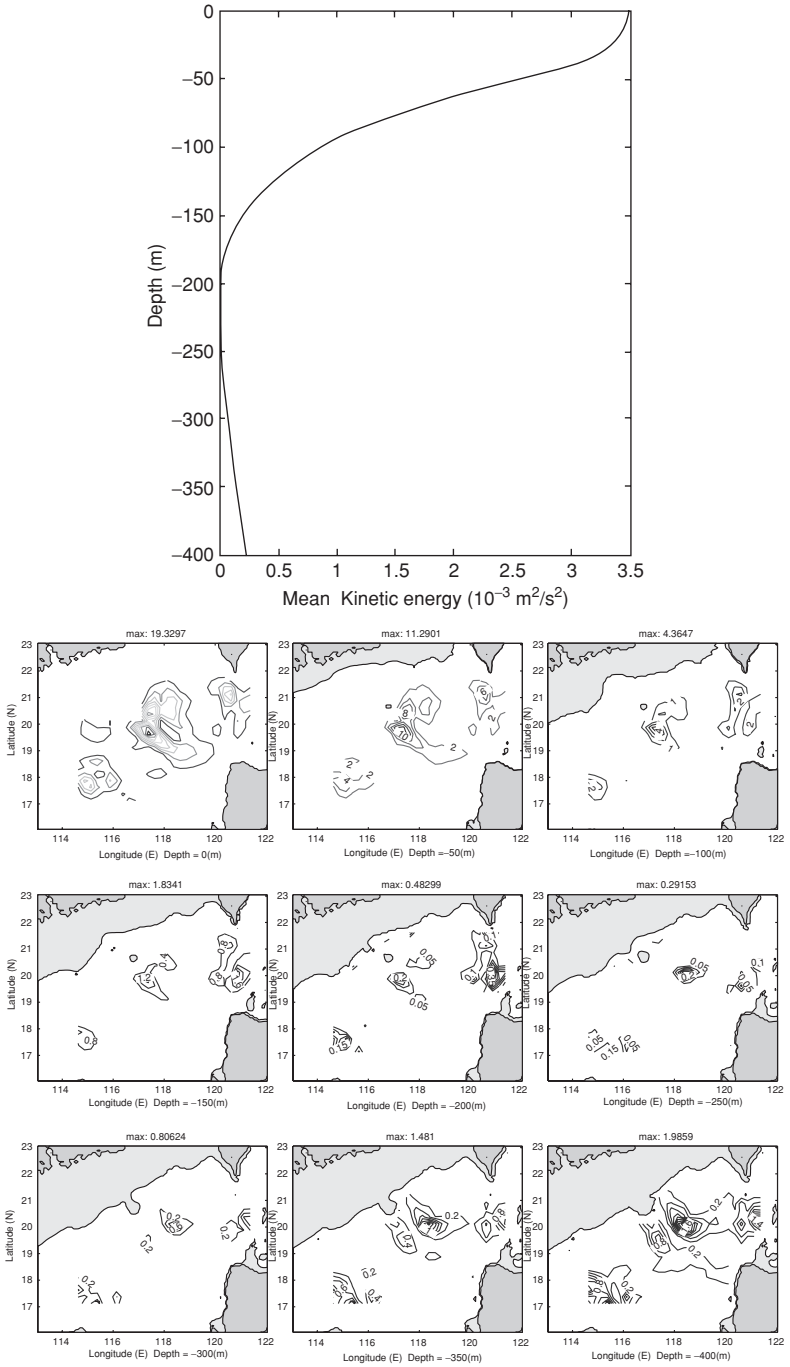

Fig. 11.81. (**a**) Vertical dependence of the mean kinetic energy per unit mass, $\bar{K}$ (in: $10^{-3}\,\mathrm{m}^2\,\mathrm{s}^{-2}$) (from Chu and Fan 2001, Journal of Oceanography). (**b**). Horizontal distribution of eddy kinetic energy per unit mass, K' (in $10^{-2}\,\mathrm{m}^2\mathrm{s}^{-2}$), at nine different depths (from Chu and Fan 2001, Journal of Oceanography)

where

$$u'(x_i, y_j, z) = u(x_i, y_j, z) - \bar{u}(z), \quad v'(x_i, y_j, z) = v(x_i, y_j, z) - \bar{v}(z). \quad (11.8)$$

The horizontal distributions of K' at different depths (Fig. 11.81b) clearly show the isolated eddy structure such as the northwestern Luzon eddy in the middle of the region (18–22°N, 116.5–119°E). The eddy kinetic energy has the maximum value ($0.19\,\mathrm{m^2\,s^{-2}}$) at the surface and decreases with the depth to $0.8 \times 10^{-2}\,\mathrm{m^2\,s^{-2}}$ at the 300 m depth. The maximum eddy kinetic energy is 1–2 orders of magnitude larger than the mean kinetic energy.

11.11 Japan/East Sea MultiEddy Structure Detected from AXBT Data

11.11.1 Background

In Sect. 6.5, the seasonal variability of the Japan/East Sea thermohaline structure and circulation is discussed. The Japan/East Sea has steep bottom topography (Fig. 6.11) that makes it a unique semienclosed ocean basin overlaid by a pronounced monsoon surface wind. It covers an area of $10^6\,\mathrm{km^2}$, has a maximum depth in excess of 3,700 m, and is isolated from open oceans except for small (narrow and shallow) straits which connect the Japan/East Sea to the Pacific Ocean. It contains three major basins called the Japan, Ulleung, and Yamato Basins, and a high central seamount called the Yamato Rise.

The Japan Sea experiences two monsoons, winter and summer, every year. During the winter monsoon season, a cold northwest wind blows over the Japan Sea as a result of the Siberian High Pressure System located over the East Asian continent. Radiative cooling and persistent cold air advection maintain cold air over the Japan Sea. The northwest–southeast oriented atmospheric Jet Stream is positioned at the Japan Sea. Such a typical winter monsoon pattern lasts nearly six months (November to April). During the summer monsoon, a warm and weaker southeast wind blows over the Japan Sea. Such a typical summer monsoon pattern lasts nearly four months (mid-May to mid-September).

May is the transition period between the two monsoons. Sudden change of the atmospheric forcing (transition from winter to summer monsoon) may vary the Japan Sea thermal structure and cause the formation of mesoscale eddies. Thus, detection of the Japan Sea thermal field during the monsoon reversal is important for the Japan Sea mesoscale dynamics. The Naval Oceanographic Office conducted an intensive AXBT survey during 1–8 May 1995, over the majority of the Japan Sea (Fig. 11.82). This temperature data set provides something close to a "snapshot" of the temperature in the upper ocean in the Japan/East Sea during the monsoon transition period. The density field during the survey period is estimated from the AXBT temperature field and

the climatological monthly mean salinity of May. The P-vector inverse method is used to obtain the absolute velocity field. Analysis on the temperature and velocity fields leads to a multieddy structure.

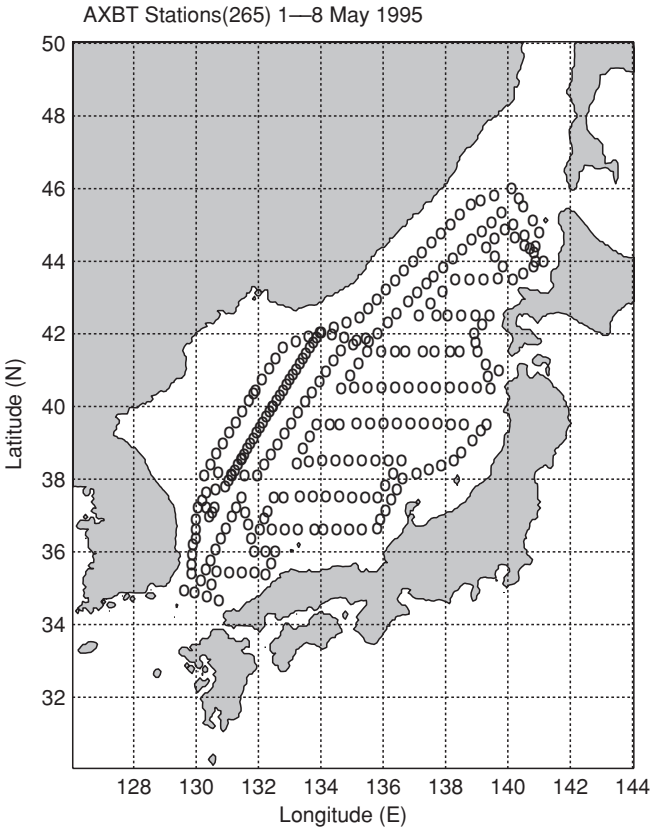

Fig. 11.82. Deployment pattern of AXBT survey during 1–8 May 1995.

11.11.2 AXBT Data

The total number of the AXBT stations is 265. The majority of the AXBTs were nominally capable of reaching a depth of 360–400 m. The vertical resolution of the AXBT data is 1 m. The ensemble of temperature profiles (Fig. 11.83a) and the mean profile with an envelope of a standard deviation (Fig. 11.83b) show the existence of a mixed layer with depths ranging from 20 to 200 m and a thermocline with a vertical temperature gradient varying from 5 to 12°C per 100 m below the mixed layer.

The same as in Sect. 11.9, the AXBT observations were mapped at each depth using a two-scale OI scheme (Gandin 1965; Lozano et al. 1996). The

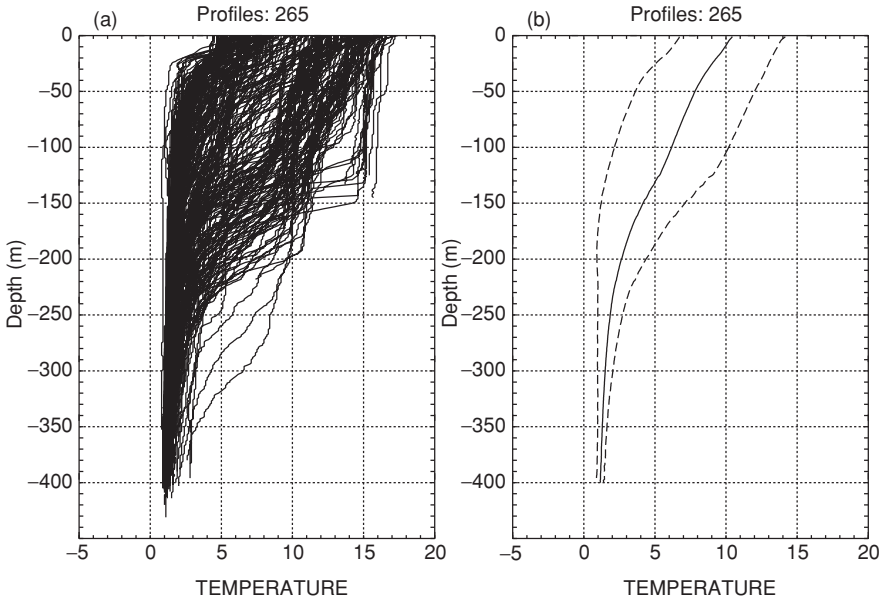

Fig. 11.83. Temperature profiles of AXBT survey during 1–8 May 1995: (**a**) ensemble of profiles, and (**b**) the mean profile with an envelope of a standard deviation

large-scale OI was used to estimate the background mean with a decorrelation scale of 450 km. The mesoscale OI was used to map the observational anomaly from the background mean field into a regular grid with spatial and temporal decorrelation scales of 150 km and 12 day. Since only temperature-measuring AXBTs were used, no salinity measurements were made at the same time. Three-dimensional velocity is inverted from this in situ temperature and climatological salinity fields in lieu of in situ salinity data.

11.11.3 Temperature

Horizontal Structures

Figure 11.84a–e shows horizontal depictions of temperature at 0-, 50-, 100-, 200-, and 300-m depths, respectively. The contour interval is 0.5°C. In them we see the Polar Front occurring near 40°N with meandering and stretching from the east Korean Bay to Tsugaru Kaikyo. Its strength increases from the surface (Fig. 11.84a) to 100 m depth (Fig. 11.84b, c) and then decreases below that depth.

The maximum horizontal temperature gradient of the Polar Front is around 8°C/100 km, appearing near the East Korean Bay at 100 m depth (Fig. 6d). At 200 m (Fig. 11.84e) and 300 m (Fig. 11.84f) depths, the Polar Front is broken into several eddies. The Polar Front separates the cold water

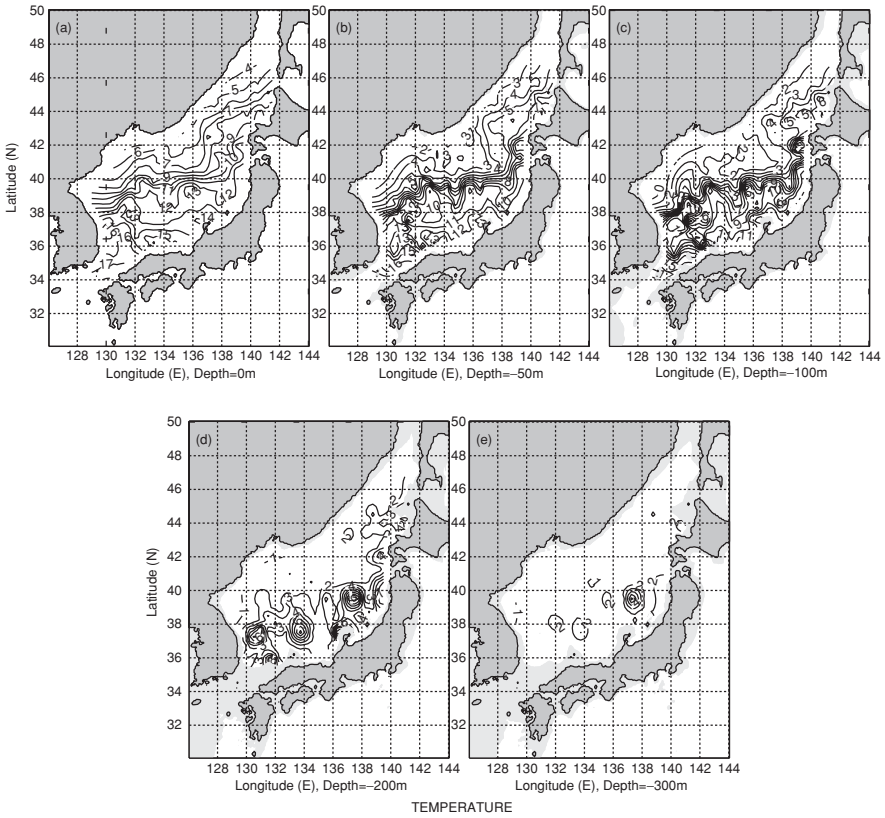

Fig. 11.84. Horizontal temperature fields at different depths: (**a**) 0-m, (**b**) 50-m, (**c**) 100-m, (**d**) 200-m, and (**e**) 300-m. The Polar Front with meandering and eddy shedding is clearly seen from the surface to 100 m depth

entering the Japan Sea from the north (Sea of Okhotsk) and the warm water entering the Japan Sea from the south (Yellow Sea) through the Korea Strait. The temperature has less variability in the north than in the south of the Polar Front. For example, at 50 m depth the temperature varies from 3 to 5°C in the north of the Polar Front and changes from 10 to 16°C in the south of the Polar Front. The meandering strengthens with depth from the surface to 100 m depth. The northward meandering of the Polar Front at 131°E, 134°E, and 138°E forms several warm-cores eddies. The southward meandering of the Polar Front at 132°E forms a cold-core eddy. At 200 m depth, three warm-core eddies with temperature of 6°C are easily identified as the Ulleung eddy at 130°30′E, 37°N, the Oki Gunto eddy at 133°45′E, 37°30′N, and the Yamato eddy at 137°20′E, 39°30′N. Cold-core eddies are generally weaker than the warm-core eddies and are evident only in upper levels (0–100 m). An eddy is

Table 11.4. Locations, typical temperatures, and tangential velocities of major eddies in Japan Sea detected during May 1–8, 1995

Depth (m)	Ulleung (W)	Oki Gunto (W)	Yamato (W)	Tsushima (°C)
0	129–131°E	133–134°E	135–137°E	131–133°E
	35–37°N	36–39°N	38–40°N	36–38°N
	$16°C, 0.1\,m\,s^{-1}$	$13°C, 0.06\,m\,s^{-1}$	$13°C, 0.1\,m\,s^{-1}$	$13°C, 0.06\,m\,s^{-1}$
	anticyclonic	meandering	meandering	cyclonic
50	129–132°E	133–135°E	136–138°E	131–133°E
	36–38°N	36–39°N	38–40°N	36–38°N
	$13°C, 0.08\,m\,s^{-1}$	$12°C, 0.08\,m\,s^{-1}$	$10°C, 0.08\,m\,s^{-1}$	$10°C, 0.06\,m\,s^{-1}$
	anticyclonic	anticyclonic	anticyclonic	cyclonic
100	129–132°E	133–135°E	136–138°E	131–133°E
	36–38°N	36–39°N	38–40°N	36–38°N
	$11°C, 0.05\,m\,s^{-1}$	$9°C, 0.05\,m\,s^{-1}$	$10°C, 0.05\,m\,s^{-1}$	$6°C, 0.05\,m\,s^{-1}$
	anticyclonic	anticyclonic	anticyclonic	cyclonic
200	129–132°E	133–135°E	136–138°E	131–133°E
	36–38°N	36–39°N	38–40°N	36–38°N
	$6°C, 0.03\,m\,s^{-1}$	$7°C, 0.02\,m\,s^{-1}$	$6°C, 0.02\,m\,s^{-1}$	$3°C, 0.02\,m\,s^{-1}$
	cyclonic	cyclonic	cyclonic	cyclonic
300	129–132°E	133 – −135°E	136–138°E	131–133°E
	36–38°N	36–39°N	38–40°N	36–38°N
	$2°C, 0.04\,m\,s^{-1}$	$2°C, 0.04\,m\,s^{-1}$	$4°C, 0.04\,m\,s^{-1}$	$2°C, 0.01\,m\,s^{-1}$
	cyclonic	cyclonic	cyclonic	cyclonic

identified in the Tsushima Basin ($131°-133°E, 36°-38°N$) as the Tsushima cold-core eddy. The thermal features of these eddies are listed in Table 11.4.

Vertical Structures

Three zonal cross sections ($43°N, 39°N$, and $36°N$) of temperature show the vertical structure of the mixed layer and the thermocline in the north of, along, and in the south of the Polar Front, respectively (Fig. 11.85. Below 300 m depth, the temperature is uniformly cold (2°C) at all three cross sections.

The cross section at 39°N clearly shows the existence of three warm-core eddies near $131°E, 133°E$, and $137°30'E$ from the downward bending (trough) of isotherms. The longitudinal span of the three warm eddies (Ulleung, Oki Gunto, and Yamato eddies) is around 200 km. The 36°N cross section clearly shows the downward bending (trough) of isotherms between $130°30'E$ and $132°30'E$, indicating the existence of a warm-core eddy. Both 39°N and 36°N cross sections clearly show the upward bending (ridge) of isotherms between 131 and 133°E, indicating the existence of a cold-core eddy, the Tsushima eddy.

Three latitudinal cross sections ($131°E, 134°E$, and $137°E$) of temperature also show evident warm-core eddy structure (Fig. 11.86). The "trough" and "ridge" of the isotherms may be considered as centers of warm-core and cold-core eddies. The three cross sections indicate three shaded warm-core eddies

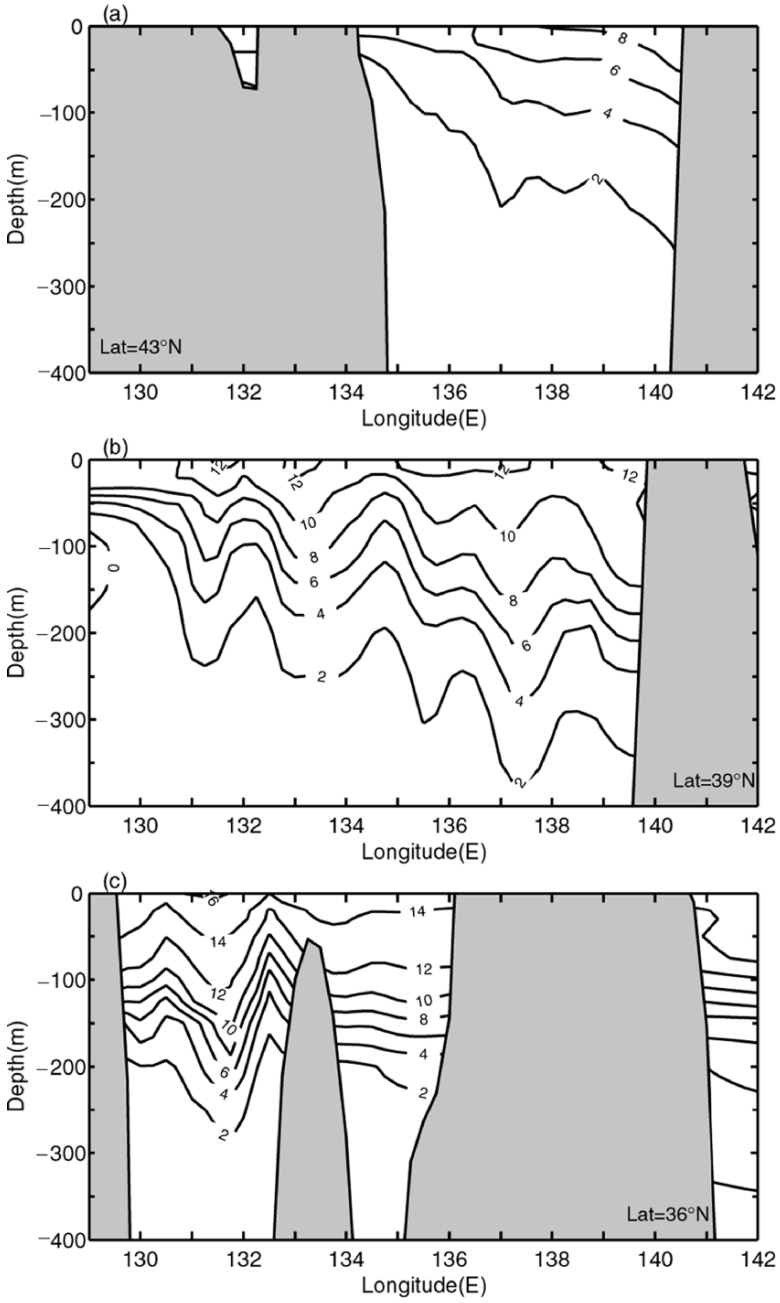

Fig. 11.85. Zonal cross sections of temperature: (**a**) 43°N, (**b**) 39°N, and (**c**) 36°N

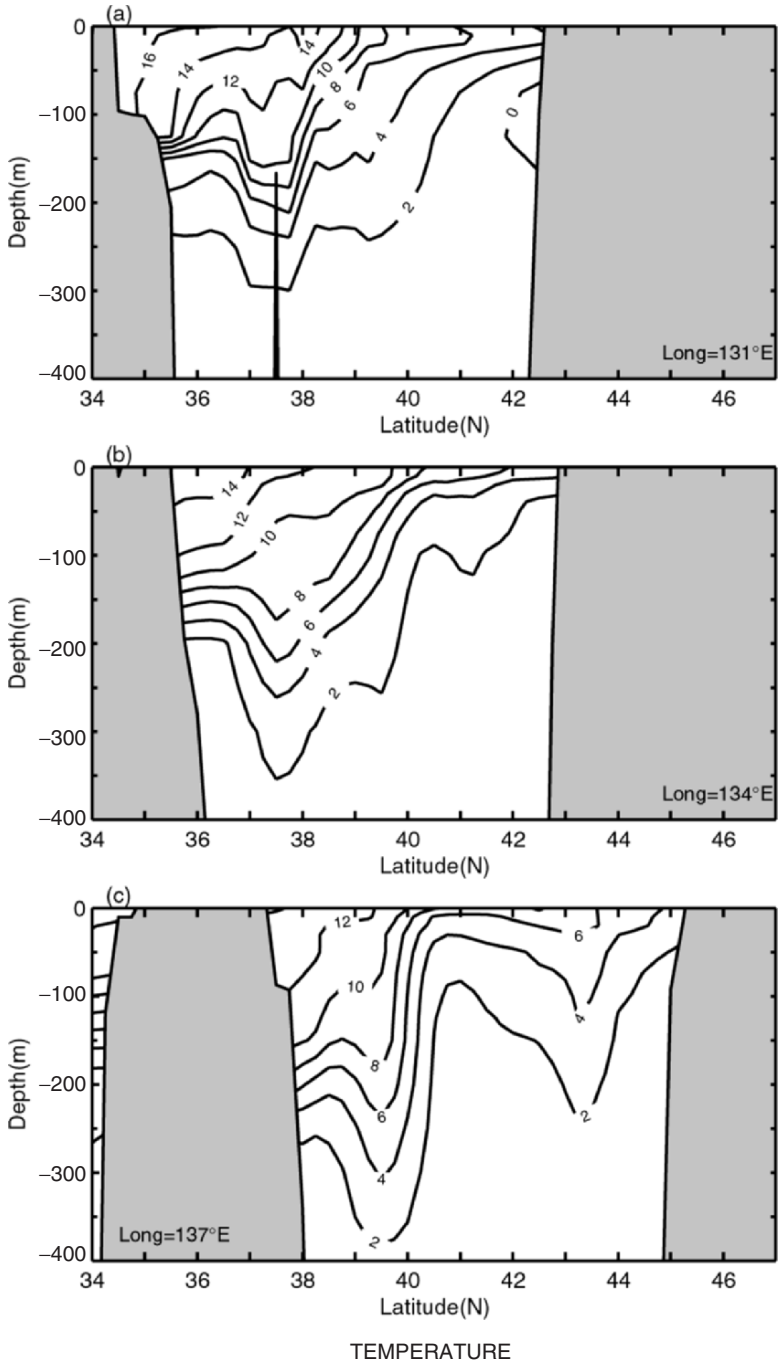

Fig. 11.86. Latitudinal cross sections of temperature: (**a**) 131°E, (**b**) 134°E, and (**c**) 137°E

from the downward bending (trough) of isotherms: 37°30′N at 131°E and 134°E, and 39°30′N at 137°E.

11.11.4 *T*–*S* and *T*–$\bar{\mathbf{S}}$ Relations

Since there were no salinity (S) observations in Japan/East Sea during 1–8 May 1995, May climatological salinity (Levitus et al. 1994) was interpolated to the AXBT stations and those salinity values ($\bar{S}$) were used for the P-vector computation. Figure 11.87a shows T–S diagram of 4,075 profiles from the MOODS in May during 1932–1994, and Fig. 10.86b shows T–$\bar{S}$ diagram from 265 temperature (AXBT) and $\bar{S}$ profiles. The spatial and temporal distributions of the MOODS data are illustrated in Fig. 11.88a, b. Comparison between the two diagrams shows that the T–S characteristics remain stable. However, we should be aware of the shortcomings in using climatological salinity values ($\bar{S}$). If the temperature field is relatively homogeneous in space, the density gradient depends mostly on the salinity gradient. Under that circumstance, the use of climatological salinity values may bring large errors in inverting the velocity field.

11.11.5 Velocity

The inverted horizontal velocity field (Fig. 11.89 indicates the evident Polar Front meandering and eddy shedding. It is easy to identify three warm-core (Fig. 11.84) baroclinic eddies: Ulleung eddy, Oki Gunto eddy, and Yamato

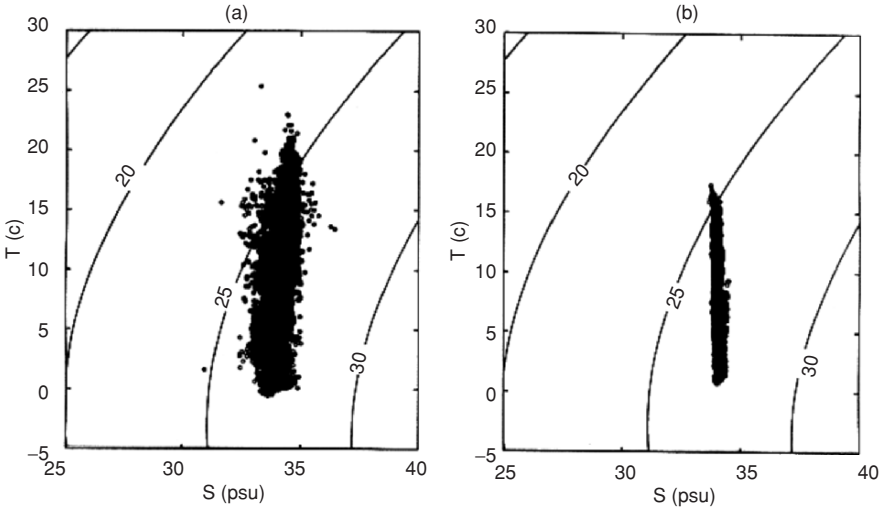

Fig. 11.87. T–S diagrams for: (**a**) the MOODS data set in May during 1933–1986, and (**b**) the AXBT temperature and May climatological salinity

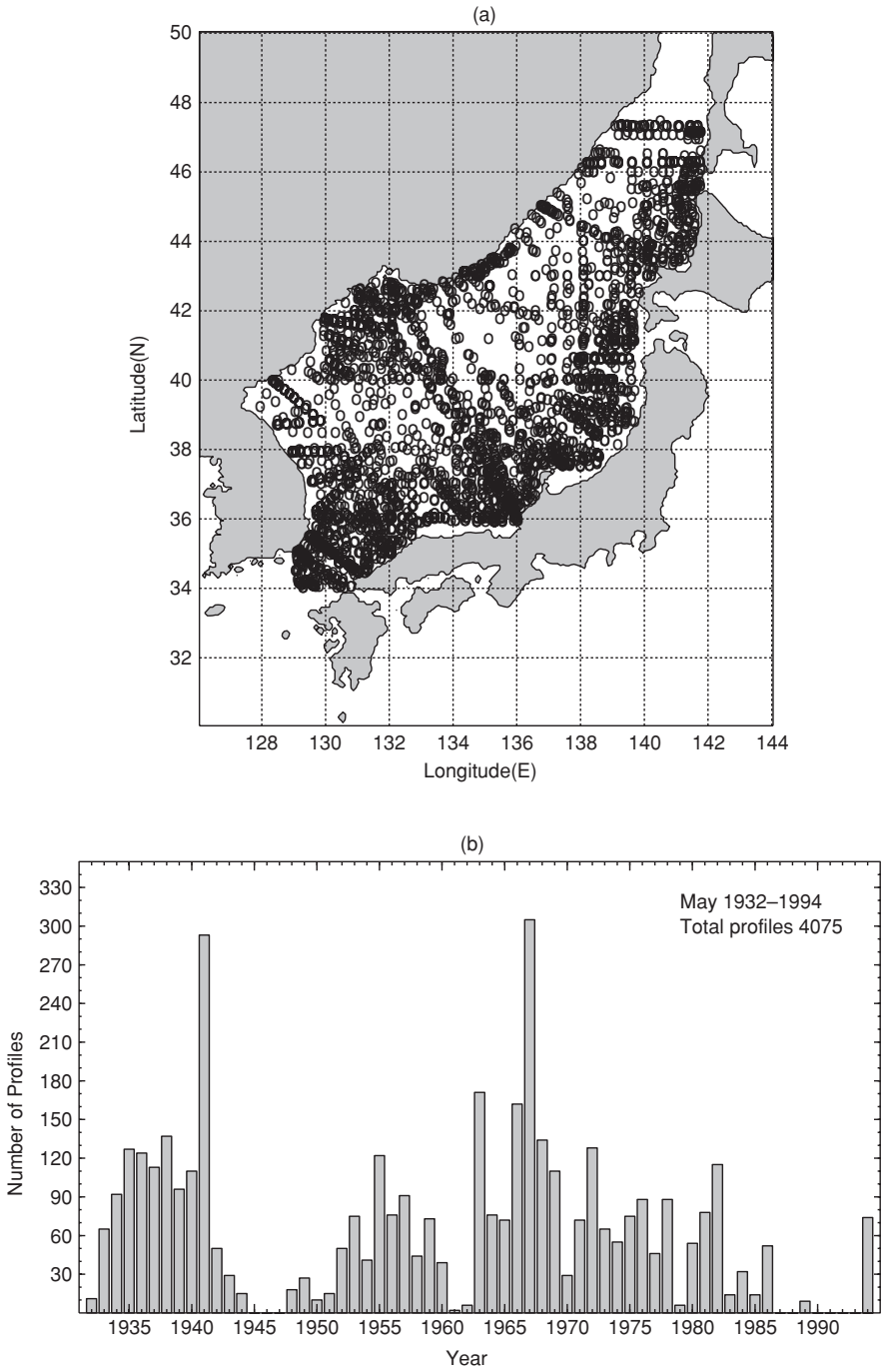

Fig. 11.88. The MOODS data distribution: (**a**) spatial, and (**b**) temporal

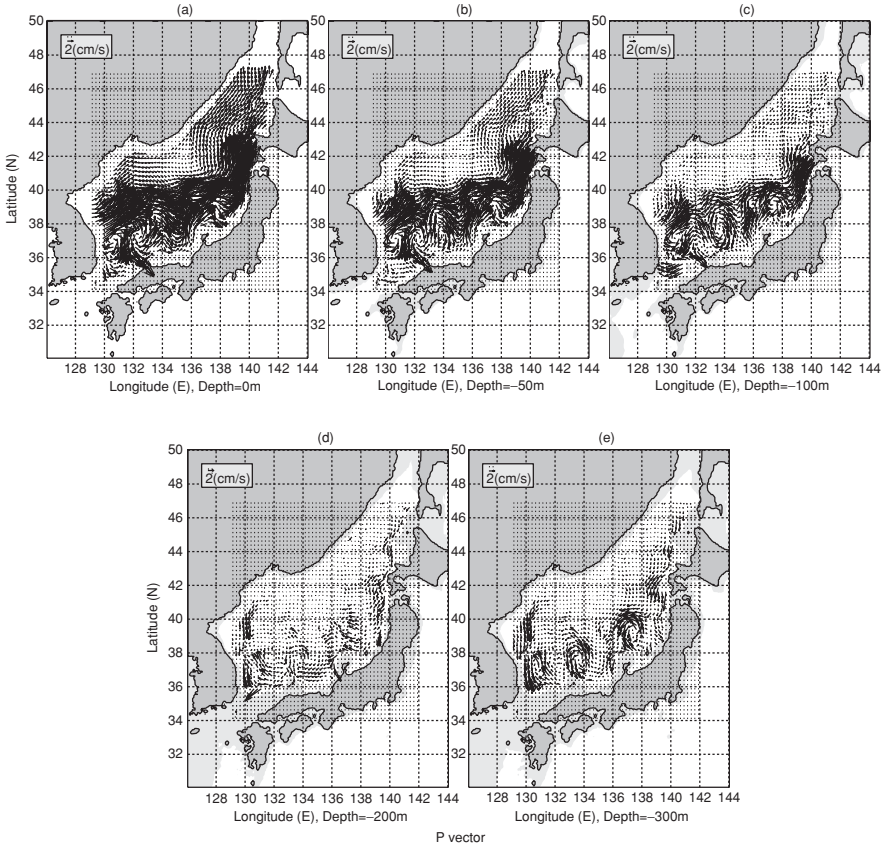

Fig. 11.89. Absolute velocity at different depths: (**a**) 0-m, (**b**) 50-m, (**c**) 100-m, (**d**) 200-m, and (**e**) 300-m

eddy. These eddies are anticyclonic at upper levels (0, 50, and 100 m), and cyclonic at lower level (300 m). It is easy to identify the Tshshima cold-core cyclonic eddy. The kinetic features of these eddies are listed in Table 11.4.

Zonal Cross Sections of v-Component

Three zonal cross sections (43°N, 39°N, and 36°N) of v-velocity show the vertical eddy structure (Fig. 11.90). The positive values indicate northward velocity, and the negative values refer to the southward velocity. Alternate positive and negative areas indicate the occurrence of cyclonic and anticyclonic eddies. At each zonal cross section, neighboring eastern negative and western positive patterns refer to an anticyclonic eddy. Neighboring western negative and eastern positive patterns refer to a cyclonic eddy. There is no evident eddy structure in 43°N cross section.

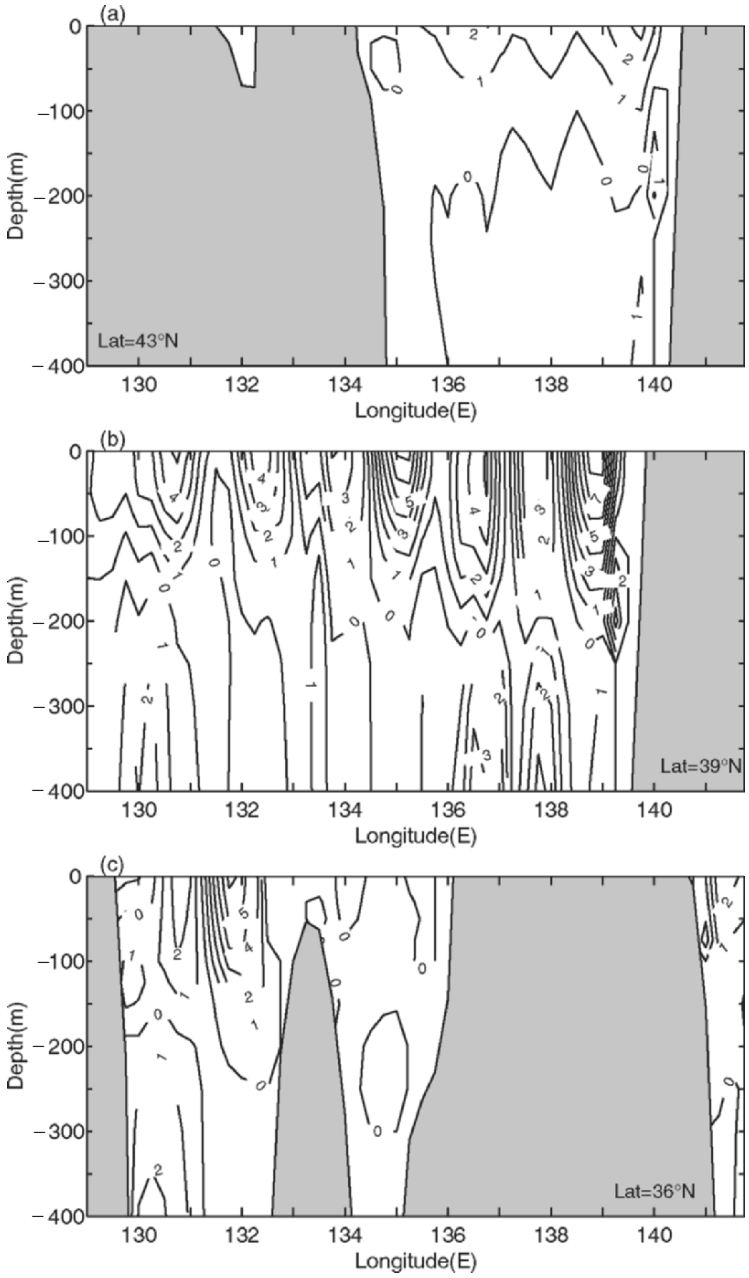

Fig. 11.90. Zonal cross sections of velocity v-component: (**a**) 43°N, (**b**) 39°N, and (**c**) 36°N

The cross section at 39°N clearly shows the existence of the Ulleung, Oki Gunto, and Yamato eddies with high baroclinicity: anticyclonic above 200 m depth and cyclonic below 200 m depth. The three eddies reveal a slightly asymmetric feature. The northward velocity in the western part is a little stronger than the southward velocity in the eastern part. For example, the Yamato warm-core eddy has a maximum northward speed of $0.09\,\mathrm{m\,s^{-1}}$ in the western part and a maximum southward speed of $0.04\,\mathrm{m\,s^{-1}}$ in the eastern part.

The cross section at 36°N clearly shows the coexistence of the Ulleung warm-core eddy and the Tsushima cold-core eddy sharing a wide southward branch between 130 and 132°E. The zonal span of both eddies is around 200 km. The depth of the Ulleung warm-core eddy is around 400 m with anticyclonic tangential velocity above 200 m depth and cyclonic below 200 m depth. The depth of the Tsushima cold-core eddy is quite shallow (above 200 m depth). Both eddies are quite asymmetric with a maximum tangential velocity of $0.05\,\mathrm{m\,s^{-1}}$ at the southward branch.

Latitudinal Cross Sections of u-Component

Three latitudinal cross sections (131°E, 134°E, and 137°E) of u-velocity also show the vertical eddy structure (Fig. 11.91). The positive values indicate eastward velocity, and the negative values refer to westward velocity. Alternate positive and negative areas indicate the occurrence of cyclonic and anticyclonic eddies. At each latitudinal cross section, neighboring southern negative and northern positive patterns refer to an anticyclonic eddy. However, neighboring northern negative and southern positive patterns refer to a cyclonic eddy.

The cross section at 131°E clearly shows the coexistence of the Ulleung warm-core eddy and the Tsusima cold-core eddy sharing an eastward branch near 36°N. Both 134°E and 137°E reveal baroclinic structure of the Oki Gunto and Yamato warm-core eddies, respectively. They have anticyclonic tangential velocities above 200 m depth, and cyclonic tangential velocities below 200 m depth.

11.12 Australian Mediterranean and South Australian Gyres

The inverted Ψ and (U, V) fields (Fig. 11.92) show the following features: the southward flowing East Australia Current is the western boundary current of the southern hemisphere. It is the weakest of all boundary currents, carrying only about 10 Sv. The current first follows the Australian coast, then separates from it somewhere around 34°S (the latitude of the northern end of New Zealand's North Island). This current recirculates (10 Sv) and forms an anticyclonic (anticlockwise) eddy. The path of the current from Australia to New Zealand is known as the Tasman Front, which makes the boundary of

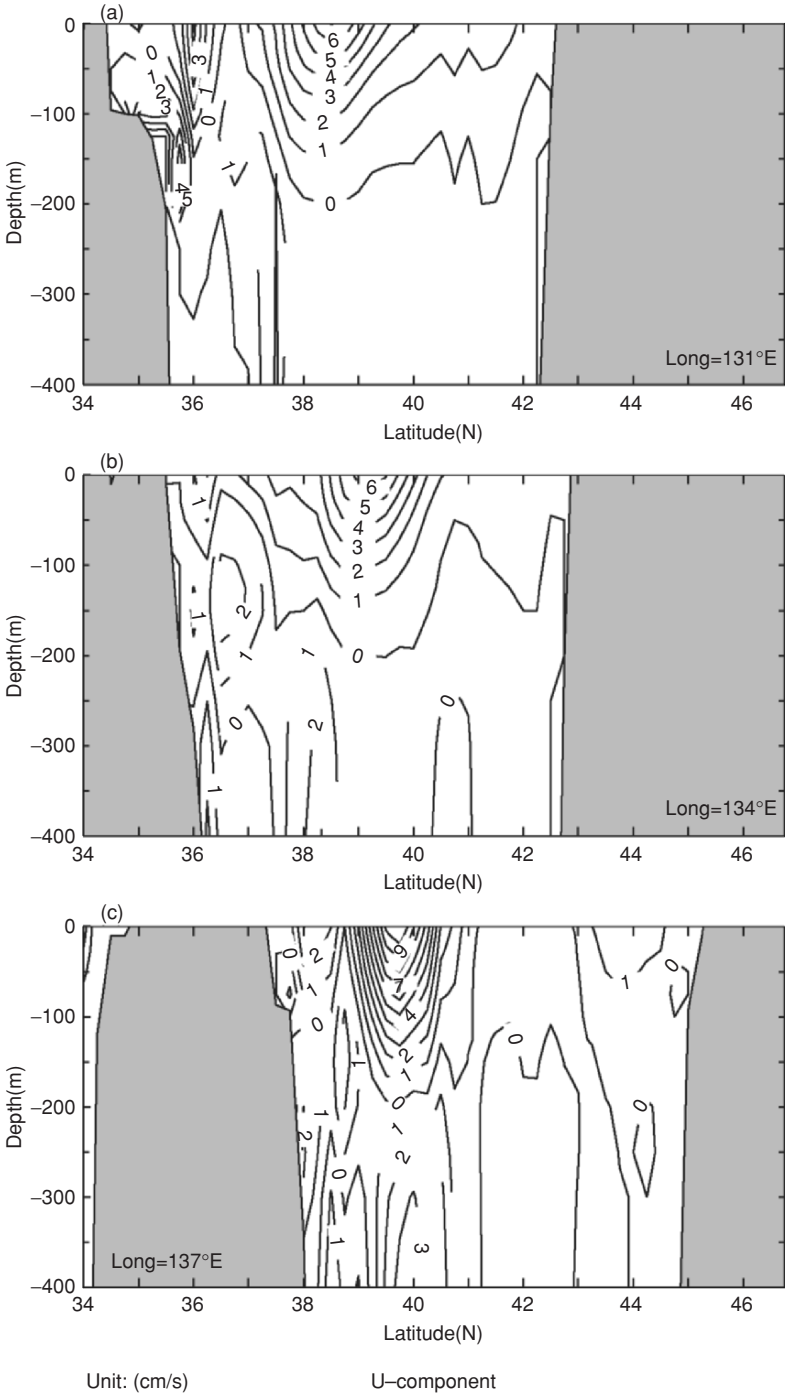

Fig. 11.91. Latitudinal cross sections of velocity u-component: (**a**) 131°E, (**b**) 134°E, and (**c**) 137°E

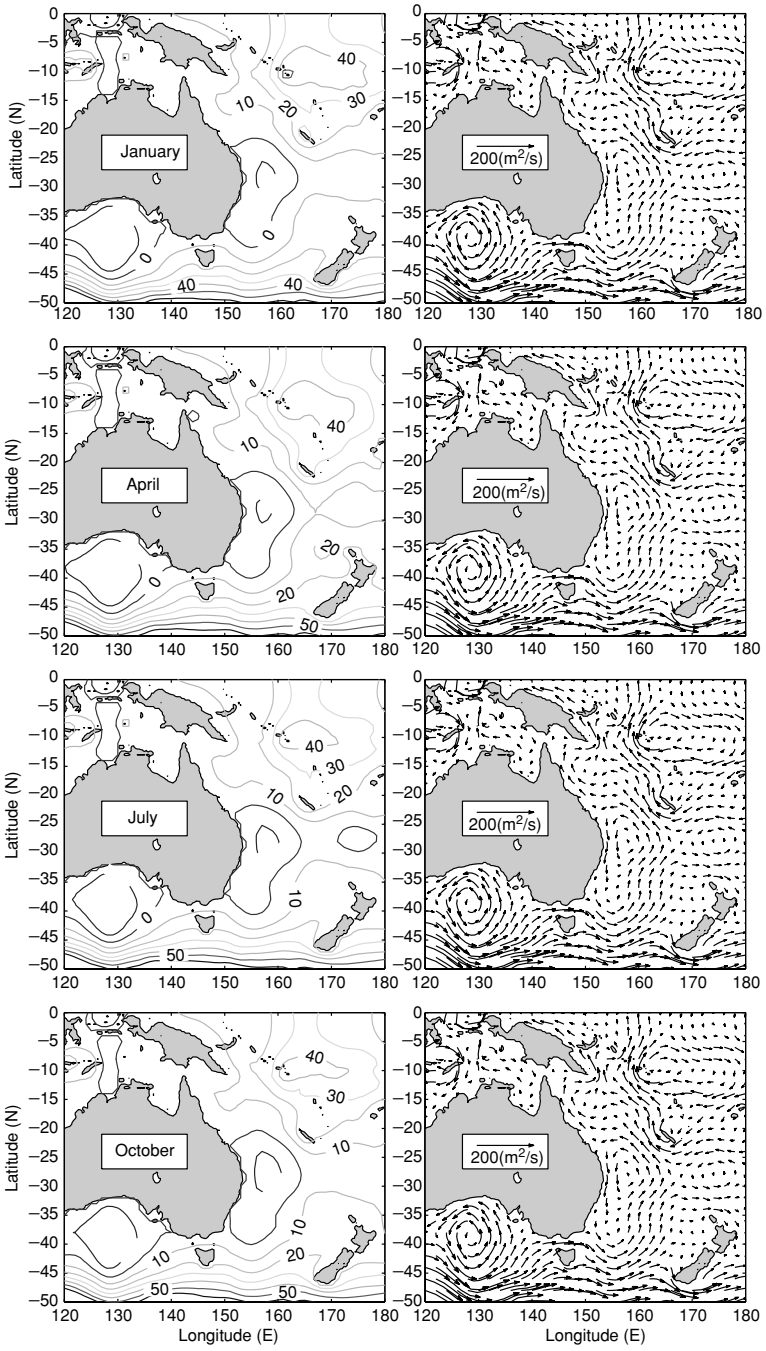

Fig. 11.92. Volume transport stream function (ψ) and vertically integrated velocity (U, V) for Australian Mediterranean and south Australian gyre

the warmer water of the Coral Sea and the colder water of the Tasman Sea. In the South Australian Basin, an anticyclonic eddy is identified and recirculates 10 Sv with a weak seasonal variation.

Questions and Exercises

(1) Discuss the major features of the basin-scale circulations in the Pacific from Fig. 11.1. Compare inverted depth-integrated velocity vectors and stream function with the results obtained from widely used ocean general models.
(2) Download the volume transport stream function from the enclosed DVD-ROM for the equatorial Pacific between 10°N and 10°S. Discuss the barotropic (depth-averaged) exchange between the Northern and Southern Hemispheres.
(3) Use Fig. 11.2a, b or download the volume transport stream function from the enclosed DVD-ROM to discuss the seasonal variability of the volume transport in the Pacific basin.
(4) Discuss the flow patterns in the Water Mass Crossroads. Figure 11.3 does not show evident seasonal variability. Do you think it is realistic? What is the flow pattern presented by other authors?
(5) Identify the seasonal variation of the three major currents (Mindanao Current, New Guinea Coastal Undercurrent, and North Equatorial Counter Current) from Fig. 11.7. Which level and which month is the Mindanao Current strongest? Discuss the physical mechanism causing these Currents.
(6) Search the velocity estimations of the three currents (Mindanao Current, New Guinea Coastal Undercurrent, and North Equatorial Counter Current) from the literature and compare them with the estimations using the P-vector method shown in Figs. 11.8, 11.9, and 11.10. Discuss the validity of using the P-vector method on isopycnal surface for the equatorial regions.
(7) Identify the seasonal variability of Mindanao Eddy and Halmahera Eddy from Fig. 11.7. Discuss the physical mechanism causing the formation of these eddies.
(8) What are the major features of the barotropic flow near Mindanao Island identified from Figs. 11.11 and 11.12? What is the physical mechanism causing the Mindanao Current to be weaker in July than in January?
(9) Discuss the volume transport (Sv) between the Celebes Sea and Pacific Ocean including total volume transport and volume transport between two isopycnal levels.
(10) Discuss the volume transport (Sv) between the Halmerhera Sea and Pacific Ocean including total volume transport and volume transport between two isopycnal levels.
(11) Is the weak seasonal variability of the Indonesia Throughflow shown in Fig. 11.17 realistic? Compare the volume transport of the Indone-

sia Throughflow identified using the P-vector method with the results reported by other authors.

(12) There are several estimations of the Kuroshio transport in the literature. Compare them with the volume transport identified from the volume transport stream function shown in Fig. 11.18. Why is the Kuroshio transport stronger in winter than in summer?

(13) The Kuroshio Water is intruded in the South China Sea as shown in Fig. 11.19. Compare this to the Gulf of Mexico, where the water is also intruded from the southern strait. Why does the Gulf of Mexico often have the Loop-Current while the South China Sea does not?

(14) What are the major features of the Subtropical Counter Current in the North Pacific? What are theories to explain the formation of the Subtropical Counter Current?

(15) Identify strong vertical shear in the Subtropical Counter Current from Fig. 11.21a, b. Discuss the effect of the baroclinic instability on the Subtropical Counter Current.

(16) What are the major characteristics of seasonal variation of the South China Sea (T, S) fields?

(17) What are the major characteristics of seasonal variation of the South China Sea circulation? What are the major currents identified from Figs. 11.34 to 11.37? Are these currents baroclinically stable or unstable?

(18) Figure 11.38 shows the existence of a thermal front in the central South China Sea. Discuss the mechanisms for the formation of this front.

(19) What is the relationship between the cross-basin circulation and the thermohaline front in the South China Sea?

(20) What is the change of T–S relation across the thermohaline front in the central South China Sea?

(21) Discuss the seasonal variability of the thermohaline front and associated cross-basin flow in the central South China Sea.

(22) What are the major features of the multieddy structure in the South China Sea? Discuss the mechanisms for the formation of the multieddies.

(23) Figure 11.69 shows two patterns of the Kuroshio intrusion into the South China Sea (bifurcation and loop) with less occurrence of the loop pattern. Can you explain why?

(24) What are the major characteristics of the cool-core eddy occurring to the west of Luzon detecting by using AXBT/AXCTD during July 8–26, 1998? What is the major mechanism for the generation of this eddy?

(25) Figures 11.80 and 11.81 show that the maximum eddy kinetic energy of the observed cool-core eddy west of Luzon is 1–2 orders of magnitude larger than the mean kinetic energy. Can you explain why?

(26) What are the major features of the multieddy structure in the Japan/East Sea? Discuss the mechanisms for the formation of multieddies.

(27) Discuss the major features of the Australian Mediterranean Gyre and the South Australian Gyre.